C. 1

MATHEMATICAL MODELLING OF THE UNBENDING OF CONTINUOUSLY CAST STEEL SLABS

by

MASATSUGU UEHARA

M.S.University Of Tokyo,1976

A THESIS SUBMITTED IN PARTIAL FULFILMENT OF

THE REQUIREMENTS FOR THE DEGREE OF

MASTER OF SCIENCE

in

THE FACULTY OF GRADUATE STUDIES

Metallurgical Engineering

We accept this thesis as conforming

to the required standard

THE UNIVERSITY OF BRITISH COLUMBIA

August 1983

Department of Metallurgical Engineering

The University of British Columbia
1956 Main Mall
Vancouver, Canada
V6T 1Y3

Date Aug. 10th, 1983

ABSTRACT

A two-dimensional, elasto-plastic, finite-element model has been developed to calculate the bending and bulging deformation of a partially solidified continuously cast steel slab during straightening on a curved-mould casting machine. A preliminary, three-dimensional elastic analysis revealed that a two-dimensional plane-stress model is sufficient for the calculations. The effects of solid-shell motion have been considered in part by shifting the roll points in two steps.

The model was checked by comparing predictions of internal cracks with plant data. From the results of calculations of a one-point bending bow-type caster (10.5m radius) for casting speeds of 1.0, 1.2 and 1.6m/min, it has been verified that internal cracks appear at the solidification front in the upper shell due to straightening of the strand at the higher casting speeds. The critical strain for internal cracks was taken to be 0.25-0.3% at a strain rate of 1×10^{-4} s^{-1} for low-carbon steels.

It has been found that the upper and lower shells deform separately around their individual neutral axes, which are shifted to within 15mm of the respective solidification fronts by the roll-friction force. Therefore the bending strain, ε_u, in the low-ductility region close to the

solidification front can be very small, lower by about 0.3% than the value predicted by one neutral-axis theory. However, as a result of the interaction with the bulging strain, ε_B, the resultant total strain, ε_T, becomes large enough to cause internal cracks(radial streaks) close to the solidification front of the upper shell. The correlation among these variables is as follows; $\varepsilon_T = (2 - 5)\ \varepsilon_B + \varepsilon_u$. Thus, the bulging strain affects the total strain significantly; and to prevent internal cracks it is important to suppress the bulging by having low surface temperatures and small roll pitches during straightening.

By comparing machine radii of 8m, 10.5m and 13m for a one-point bending bow-type caster, it has been verified that the small machine radius of 8.0m is unfavorable because at normal casting speeds the tensile strain at the solidification front exceeds the critical value for crack formation.

TABLE OF CONTENTS

LIST OF TABLES

LIST OF FIGURES

LIST OF SYMBOLS

d	slab thickness (mm)
d_o	grain size (μm)
$[D]$	material matrix
E	Young's modulus (MPa)
F_i	roll friction force (N)
$[K]$	stiffness matrix
l_{Ri}	roll pitch (mm)
Δl	elongation (mm)
n	strain-hardening exponent
N	number of rolls necessary to absorb the bending deformation
$[N]$	matrix of shape function
p_i	ferrostatic pressure (MPa)
Q	self-diffusion energy (J/mol)
R	machine radius (mm)
R_o	gas constant (J/mol°K)
s	shell thickness (mm)
T	temperature (°C)
T_o	surface temperature (°C)
$\overline{u}_x$	average displacement in x direction (mm)
u_Y	displacement in y direction (mm)
V	casting speed (m/min)
w	slab width (mm)
Δy	distance between outer and inner surfaces (mm)
y	distance from the neutral axis (mm)

Z	Zener-Hollomon parameter (s^{-1})
δ_{max}	maximum bulging deflection (mm)
ε	strain
ε_1	strain at inner surface
ε_2	strain at outer surface
$\dot{\varepsilon}$	strain rate (s^{-1})
ε_u	bending strain
ε_B	bulging strain
ε_T	total of bending and bulging strain
$\overline{\varepsilon}_p$	effective plastic strain
ρ	curvature of the strand (1/mm)
σ	stress (MPa)
$\overline{\sigma}$	effective stress (MPa)
σ_p	peak stress (MPa)
σ_Y	Yield stress (MPa)
μ	frictional coefficient
ν	Poisson's ratio

ACKNOWLEDGEMENTS

I wish to express my sincere gratitude to Dr.J.K.Brimacombe and Dr.I.V.Samarasekera for their useful advice and guidance throughout the course of this study.

Thanks are also extended to my fellow graduate students and faculty members in the Department of Metallurgical Engineering. The assistance of the technical staff and in particular that of Mr.N.Walker is greatly appreciated.

I am also grateful to the Natural Sciences and Engineering Research Council of Canada and Nippon Steel Corp. in Japan for providing financial support. Special thanks must also be given to Mr.H.Misumi for his assistance in providing the plant data.

Finally, I would like to take this opportunity to thank my wife Teruko for her assistance in this work.

Chapter 1

INTRODUCTION

During the last two decades several types of continuous-casting machines have been developed for the production of steel slabs. The machine types include the vertical, vertical with bending, circular arc and oval bow which are shown schematically in Fig.1. With increasing demands on production rate and product quality the trend has been away from the vertical type to the low-head, bow-type caster. In the case of the latter, however, the strand is straightened while containing a liquid core. The resultant bending gives rise to elongation, which can cause internal cracks, close to the solidification front where the ductility of the steel is very low. In addition other types of stresses are applied to the solidifying shell,viz. bulging stresses due to ferrostatic pressure and thermal stresses.[1,2,16] Even though the ferrostaic pressure is relatively small in a low head bow-type caster, bulging strain may combine with bending strain to create excessive strains at the solidification front. This effect will

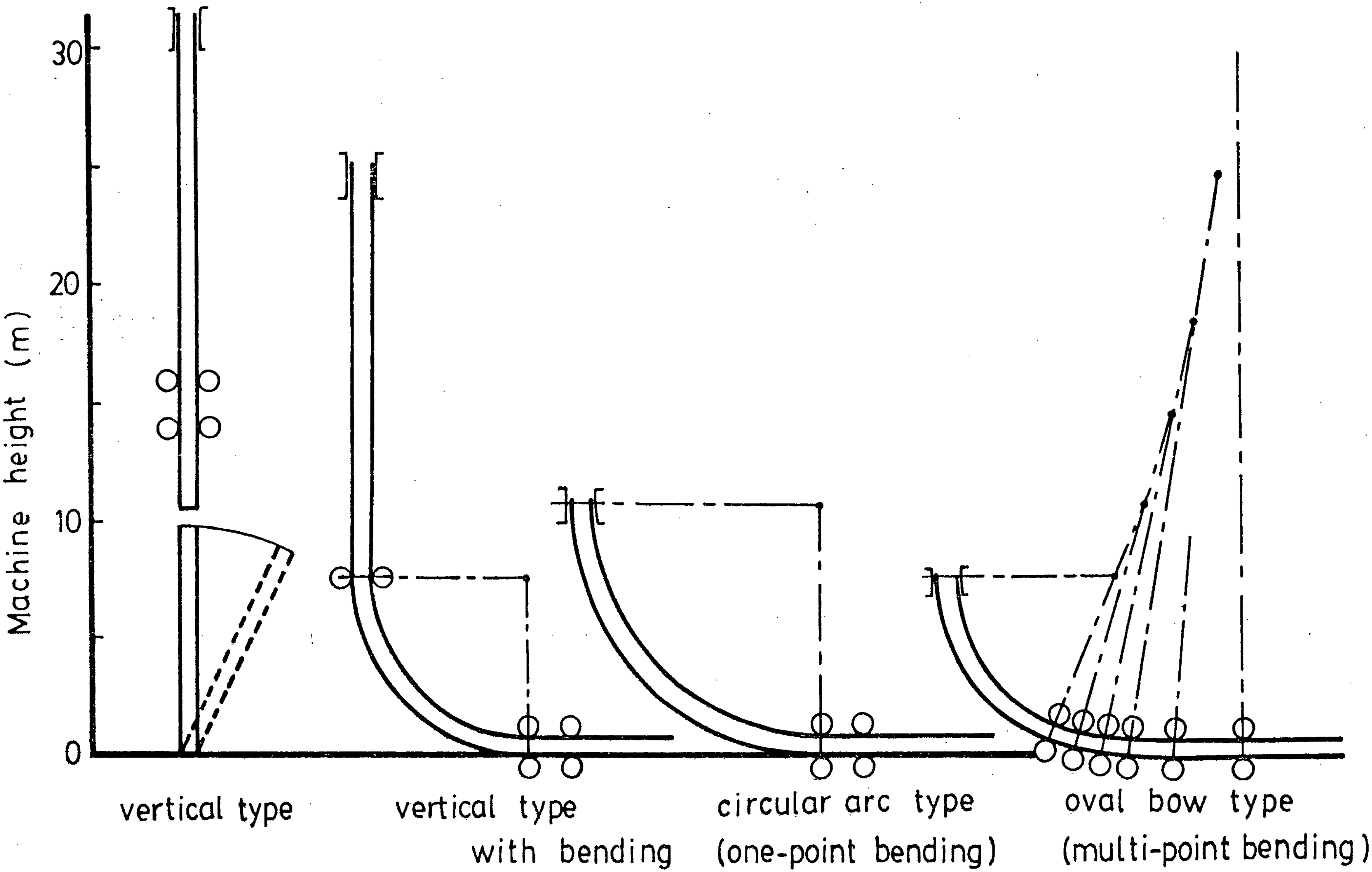

Fig.1 Schematic drawing of Different Types of Casting Machines[40].

be shown in this thesis.

As increasing emphasis has been placed on product quality, stress analysis has been one of the tools employed to study the formation of internal cracks in continuously cast steels since the latter half of the 1970's. However, only a few studies have been reported on the analysis of stresses in bending ; and hence the task is by no means complete. Further investigations are urgently required on this subject from a design point of view, because optimum and limiting machine designs are required in order to meet the strict demands for the modern low head casters. In the present work, the stress analysis of one-point bending will be considered as a first step toward a better understanding of bending behavior.

Chapter 2

PREVIOUS WORK AND OBJECTIVES OF PRESENT WORK

2.1 Internal cracks in continuously cast slabs

It has long been recognized that even small tensile strains applied to the solidifying steel shell can lead to the generation of internal cracks (solidification cracks) close to the solidification front.[41,42] The internal cracks due to bulging or bending of slabs can be seen normal to the broad face in a longitudinal section. In most cases, bending cracks are formed in the upper shell in the straightening zone and bulging cracks are generated in upper and lower shells beneath the roll support points. These cracks are visible on sulphur prints since they are generally filled with solute rich residual liquid (see Figs.5.8 - 5.10 Section 5.1.1).

The critical strains for internal cracks have been reported to be dependent on steel grades and strain rates with low-carbon steels and low strain rates giving high critical strains. Table I presents reported values of critical strain for these conditions. Some scatter in the data (0.2 - 3.0%) can

Table I Studies of critical strain for internal cracks

Study	Method used to obtain critical strain	Critical strain ε_{crit}	Ref
Palmaers	Based on elasto-plastic thermal stress calculation of a continuously cast bloom. C=.18% $\dot{\varepsilon}$?	0.2%	12
Puhringer	Based on elasto-plastic-creep bulging calculation of a continuously cast slab. C=.05% $\dot{\varepsilon}=6\times10^{-4}\ s^{-1}$	0.39%	15
Daniel	Based on elasto-plastic bulging calculation of a continuously cast bloom. C=.15% $\dot{\varepsilon}$?	0.6%	36
Narita	Roll misalignment test on a continuously cast bloom. Strain is calculated based on elasto-plastic simulation model. C=.15% $\dot{\varepsilon}=4\times10^{-4}\ s^{-1}$	0.3%	37
Suzuki	Reduction test . Low carbon steel. $\dot{\varepsilon}=1\times10^{-4}\ s^{-1}$	0.25-0.6%	38
Matsumiya	Laboratory 3-point bending test. Specimen is partly melted by electrical input. C=.15% $\dot{\varepsilon}=5\times10^{-4}\ s^{-1}$	2.0-3.0%	39

be seen owing to the different methods used to estimate the critical strain at the solidification front. Since it is difficult to measure the strain at this location, the critical value has been calculated in these studies with some experimental input. From Table I , four of the six authors report a value in the range of 0.2-0.5% ;and this has been adopted in the present study.

To overcome the problem of internal cracks due to straightening, the following two steps have been adopted in practice: "compression casting" and "multi-point bending". The principle of the compression casting method is to cancel harmful tensile stresses at the solidification front by applying a compressive force in the bending zone. To this end, several driven rolls are required before the bending point to push the strand with a large force against several rolls following the bending point whose movement is electrically controlled so as to apply a braking force to the strand and , at the same time, prevent slab slippage.[34] In the case of multi-point bending the straightening is divided into several bending steps and hence tensile stresses at the solidification front are greatly reduced.[43] Multi-point bending casters are under development at present as a new type of low-head, oval-bow machine.

2.2 Previous work on stress analysis of bending and bulging

As mentioned previously, owing to the interaction of bending strain and bulging strain internal cracks can occur very easily in the straightening zone in a bow-type caster. Bulging and bending must be analysed simultaneously to study the formation of internal cracks due to unbending.

Numerous studies have been devoted to bulging analysis [12,15,20-27]; the results will be discussed in detail in Section 3.3.2. However only a few mathematical models have been reported on bending[15,31,44,45] and no model has yet been reported in the literature on the bulging and bending analysis of continuously cast slabs which is the subject of the present thesis.

The single beam theory, which assumes a neutral axis at the center of the slab thickness, has long been used to explain the bending behavior of continuously cast slabs. According to this beam theory, the bending strains, ε_u , for one-point and multi-point bending, shown schematically in Fig.2, are given respectively by the following equations .

one-point bend ; $$\varepsilon_u = (\frac{d}{2} - s) / R_o \qquad (1)$$

multi-point bend ; $$\varepsilon_u = (\frac{d}{2} - s_n)(1/R_{n-1} - 1/R_n) \qquad (2)$$

As is apparent from Eq.(1), the bending strain becomes larger with decreasing shell thickness and machine radius. However, the assumption of one neutral axis is questionable at the center of

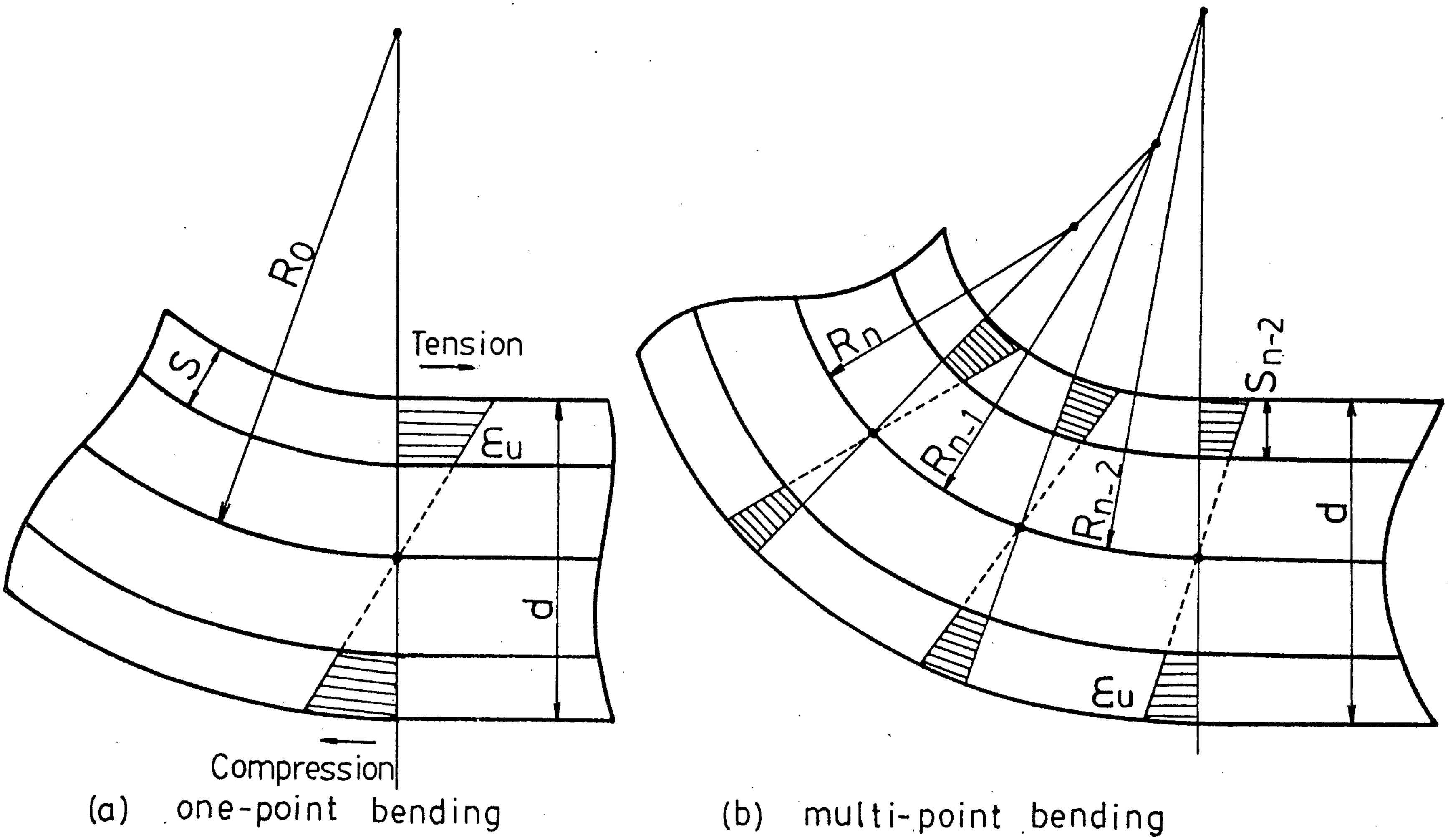

Fig. 2 Elongation at the Solidification Front during Bending.

a wide face of a slab. Based on three-dimensional elastic analysis Vaterlaus[44] has proposed a two neutral-axes theory in which the upper and lower shells deform independently. However his model predictions are contradictory to the observations of internal cracks ,i.e. the harmful tensile strains due to unbending occur at the solidification front in the lower shell and hence internal cracks must appear in the lower shell. A dynamic simulation model has been reported by Onishi[31] based on the one-dimensional, elasto-plastic, finite-element method. Unfortunately this model is only suitable for calculation of roll reaction forces, and cannot be used to evaluate strain distributions through the shell thickness because it is based on an assumption of one neutral-axis theory.

2.3 Objectives of present work

The present study has been undertaken to elucidate machine design parameters and casting conditions that have a strong influence on the state of strain and on crack formation during the unbending of partially solidified steel slabs. A two-dimensional, elasto-plastic,finite-element model has been formulated for this purpose . The primary concerns of the analysis are as follows:

(1) To determine the unbending behavior,i.e. to ascertain whether the conventional single neutral-axis theory is correct or not.

(2) To calculate the critical strain for internal cracks in unbending and to compare it with the values reported in the literature.

(3) To find a correlation between resultant total strain, ε_T, and each of the components of bulging strain, ε_B, and bending strain, ε_u.

The present one-point bending model will provide the basis for the design of a new low-head, bow-type caster.

Chapter 3

BENDING/UNBENDING STRESS ANALYSIS OF CONTINUOUSLY CAST SLABS

3.1 Introduction

Stress analysis has been performed of the bending/unbending of partially solidified wide steel slabs. This is a very complicated problem because while passing through the straightening zone the strand is subjected alternately to tension and compression due to the interaction of ferrostatic pressure pushing the solidified shell outward and the rolls pushing against the shell in the opposite direction. Thus each element of the strand exhibits a complex hysteresis. At the center plane of the wide face of the slab, deformation of the strand is enhanced as a result of interaction between bending and bulging. On the other hand at the corner, deformation is primarily due to bending. Thus, in formulating a model to calculate bending of the moving strand with a liquid core, bending and bulging deformations have to be considered simultaneously as a three-dimensional, visco-elastic-plastic problem. This introduces considerable complexity to the problem and can result in prohibitively high computing costs.

In order to render the problem into a more tractable form the following steps were taken.

Firstly, three-dimensional elastic analysis was applied to the bending of the wide slab, where the strand was considered to be a hollow box with temperature gradients through the shell thickness. Results of the calculation have shown that the deformation at the center plane of the wide face is independent of the side edge. Comparison of this result with that of a two-dimensional plane-stress model of the center plane of a slab has indicated that a two-dimensional model can be applied to the bending analysis of wide slabs as in the case of bulging analysis.[21] Thus, a two-dimensional model has been formulated for the longitudinal section at the center plane of the wide face of slab.

In the formulation of the model elasto-plastic behavior has been incorporated but the effects of creep were not considered. During straightening, the principal component of the total strain is related to elasto-plastic deformation while for bulging if the roll spacing is sufficiently small creep can be negligible.[22] Since displacement boundary conditions are imposed, it is anticipated that creep will not enhance the total strain but will cause a stress relaxation instead in the bending analysis.

For the boundary conditions, which are usually the most important aspect of a mathematical model, the following two factors specifically have been considered. The calculation has been performed in two stages and for each stage the roll supports have been appropriately chosen to simulate as simply as possible a moving strand. This semi-dynamic simulation proved useful particularly for the lower shell and resulted in a smoother strain distribution at the solid-liquid interface. Secondly, roll friction force has been considered. This approach is different from the usually adopted concept of withdrawal resistance in that this force is derived from the bending deformation of the slab. This roll friction force has been used as the force boundary condition on the upstream edge of the shell in the finite-element analysis. These topics are discussed in greater detail in the subsequent sections.

3.2 Mechanical properties of low carbon steels at elevated temperature

A factor of paramount importance in a modelling study of this kind is the accuracy of the mechanical property data. The mechanical properties of steel at elevated temperatures are dependent on temperature , strain rate , thermal history, structure and chemical composition. In order to calculate the stresses in the solidifying shell of continuously cast slabs the property data utilized should be obtained from tests conducted under conditions similar to those in a caster.

In the past few years several studies have been conducted to determine the plastic behavior of steels at elevated temperatures for a variety of strain rates.[3-16] Since at these temperatures it is difficult to separate out the effects of creep from the data it is important to choose data obtained for strain rates comparable to those encountered in continuous casting. It is thus possible to partially account for the effects of creep in modelling the strain distribution in the strand, with an elasto-plastic model.

For this study, mechanical properties of steel in the temperature range 900°C to the solidus temperature and for strain rates in the range from 10^{-5} to 10^{-2} s^{-1} must be known. Properties particularly important are

1) Young's modulus, E
2) Yield stress, σ_Y
3) Poisson's ratio, ν
4) Strain-hardening exponent, n

The temperatures and strain rates given above are typical of values encountered in continuous casting.[3]

3.2.1 Types of stress-strain curves

Before proceeding to the mechanical property data, it is important to understand the general features of the flow curves at high temperatures and low strain rates. Three types of stress-strain curves have been reported for austenitic iron at elevated temperatures and low strain rates,[11,14] as shown in Fig.3.1[14].

Type-1; The flow stress increases to a peak value

C, %	T°C (×100)	13	12	11	10	9	8.25	8	7.75
0.10	$\dot{\varepsilon}=6.7\times10^{-4}/s$	●	●	●	△	□			
	" $\times10^{-3}/s$	●	●	△	△	□			
	" $\times10^{-2}/s$	●	●	△	□	□			
0.25	$\dot{\varepsilon}=6.7\times10^{-4}/s$	●	●	●	●	△	□		
	" $\times10^{-3}/s$	●	●	●	△	□	□		
	" $\times10^{-2}/s$	●	△	△	□	□	□		
0.39	$\dot{\varepsilon}=6.7\times10^{-4}/s$	●	●	●	●	△	△□	□	
	" $\times10^{-3}/s$	●	●	△	△	□	—	□	
	" $\times10^{-2}/s$	△	△	△	□	□	—	□	
0.71	$\dot{\varepsilon}=6.7\times10^{-4}/s$	●	●	●	●	△	△□	□	□
	" $\times10^{-3}/s$	△	△	△	△	□	—	□	—
	" $\times10^{-2}/s$	△	△	△	△	□	—	□	—

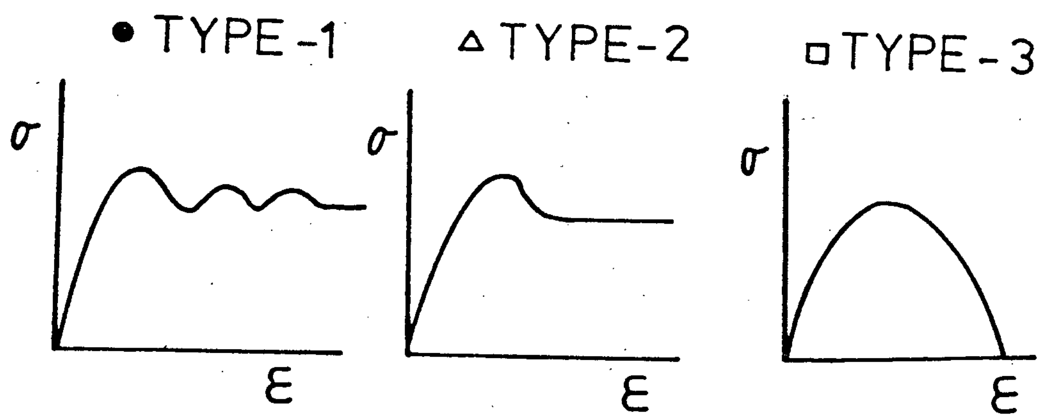

Fig. 3.1 Stress-Strain Curves for Austenitic Iron at Elevated Temperatures and Low Strain Rates.[14]

and then falls to a level which oscillates about a mean. (at high temperatures and low strain rates)

Type-2; The flow stress increases to a peak value and then falls to a steady-state level. (between values of Type-1 and 3)

Type-3; The flow stress increases to a maximum value and then decreases rapidly without reaching a steady-state. (at low temperatures and high strain rates)

The stress-strain data required for the present study is for the initial strain hardening region, that is up to about 1% of the true strain.

3.2.2 Mechanical property data

The following data have been used in this work.

1) Young's modulus, E

The data obtained by Mizukami[7] for a 0.08%C steel, from tensile tests and a resonance method, were adopted as shown in Fig.3.2. The results of the tensile tests show that the Young's modulus is independent of strain rates in the region from 1×10^{-4} to $3\times10^{-3}\ s^{-1}$. The dependence of E on temperature is as follows.

$1000 \le T \le 1400°C$

$$E=1.96 \times 10^{4}-18.375(T-1000) \quad \text{MPa} \quad (3)$$

$1400 \le T \le 1475$

$$E=1.225 \times 10^{4}(1475-T)/75 \quad \text{MPa} \quad (4)$$

$T>1475$

$$E=0 \quad \text{MPa} \quad (5)$$

2) Yield stress, σ_Y

The data obtained by Niedermayr[16] at low strain rates were employed as shown in Fig.3.2. For the higher strain rates above 10^{-2} s^{-1}, a higher yield stress has been observed by Jonas[9]. The formulation of yield stress by Niedermayr ia as follows.

$1000 \le T \le 1200°C$

$$\sigma_Y=66.15-4.655 \times 10^{-2}T \quad \text{MPa} \quad (6)$$

$1200 \le T \le 1480$

$$\sigma_Y=54.39-3.675 \times 10^{-2}T \quad \text{MPa} \quad (7)$$

$T>1480$

$$\sigma_Y=0 \quad \text{MPa} \quad (8)$$

3) Poisson's ratio, ν

Poisson's ratio was assumed to be temperature dependent[17,18], as shown in Fig.3.2.

$$\nu=8.23 \times 10^{-5}T+0.278 \quad (9)$$

4) Strain-hardening exponent, n

The following stress-strain relationship was used to simulate the plasticity.

$$\sigma = K \cdot \varepsilon^{n} \tag{10}$$

where K is a constant, ε is the true strain, and n is the strain-hardening exponent. The exponent n depends in a complex way on such parameters as temperature, strain rate, total strain, grain size, etc. , and therefore cannot be expressed by a simple equation. However, a correlation has been observed recently by Sakai[6] between the strain-hardening exponent and the first peak stress, σ_p ,or hence Zener-Hollomon parameter,Z, under conditions of controlled grain size (d_0=38 μm and 42.3 μm) as shown in Fig.3.3. The Zener-Hollomon parameter is given as follows.

$$Z = \dot{\varepsilon} \exp\left(\frac{Q}{R_0 T}\right) = A \cdot \sigma_p^{m} \qquad s^{-1} \tag{11}$$

where, Q=(self-diffusion energy) J/mol

R_0=8.319 (gas constant) J/mol°K

and A,m are constants. The value of n in the γ-phase increases monotonically with increasing peak stress , σ_p , or Z. The data calculated from Palmaers[12],

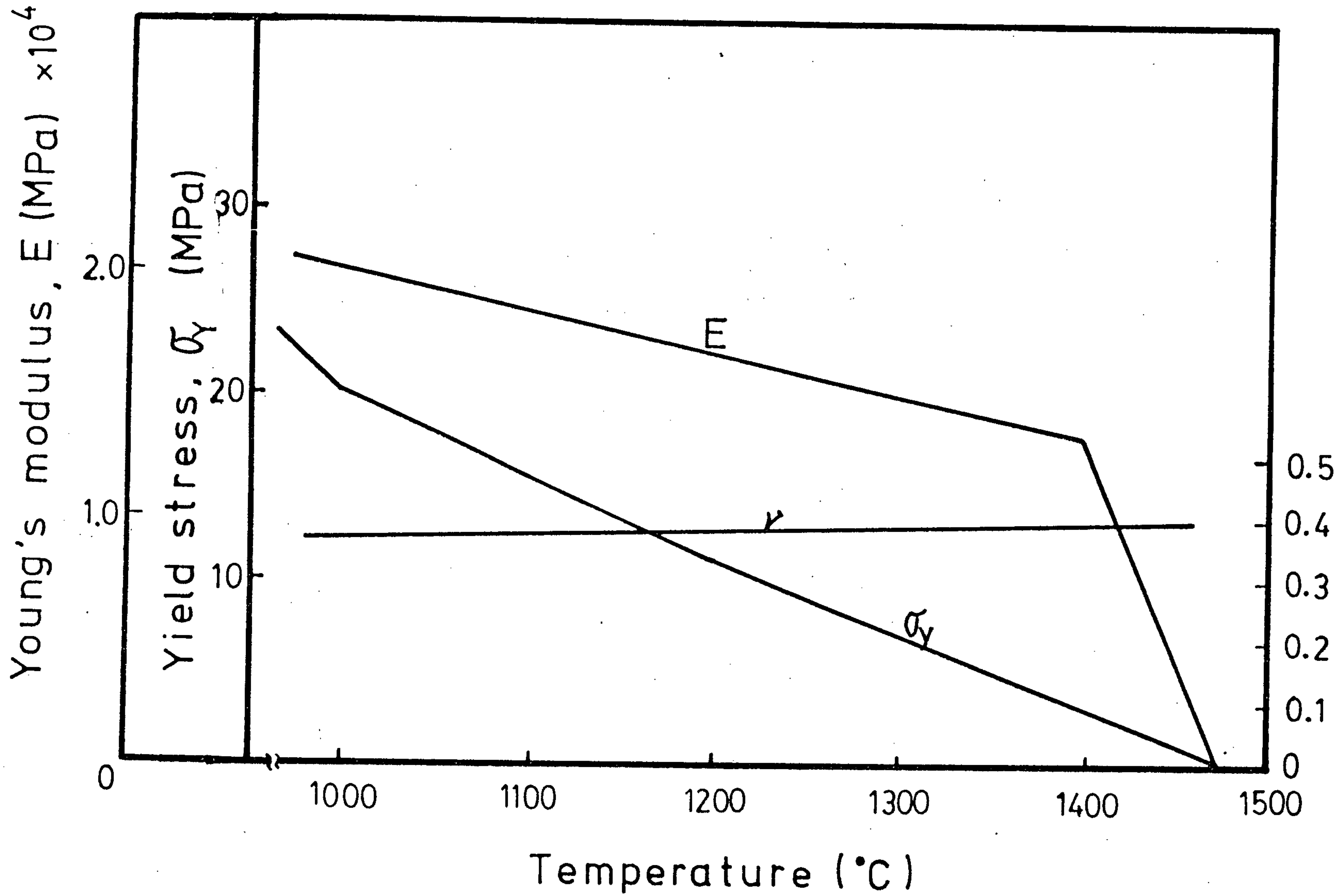

Fig. 3.2 Assumed Mechanical Properties of Slab at Elevated Temperature.

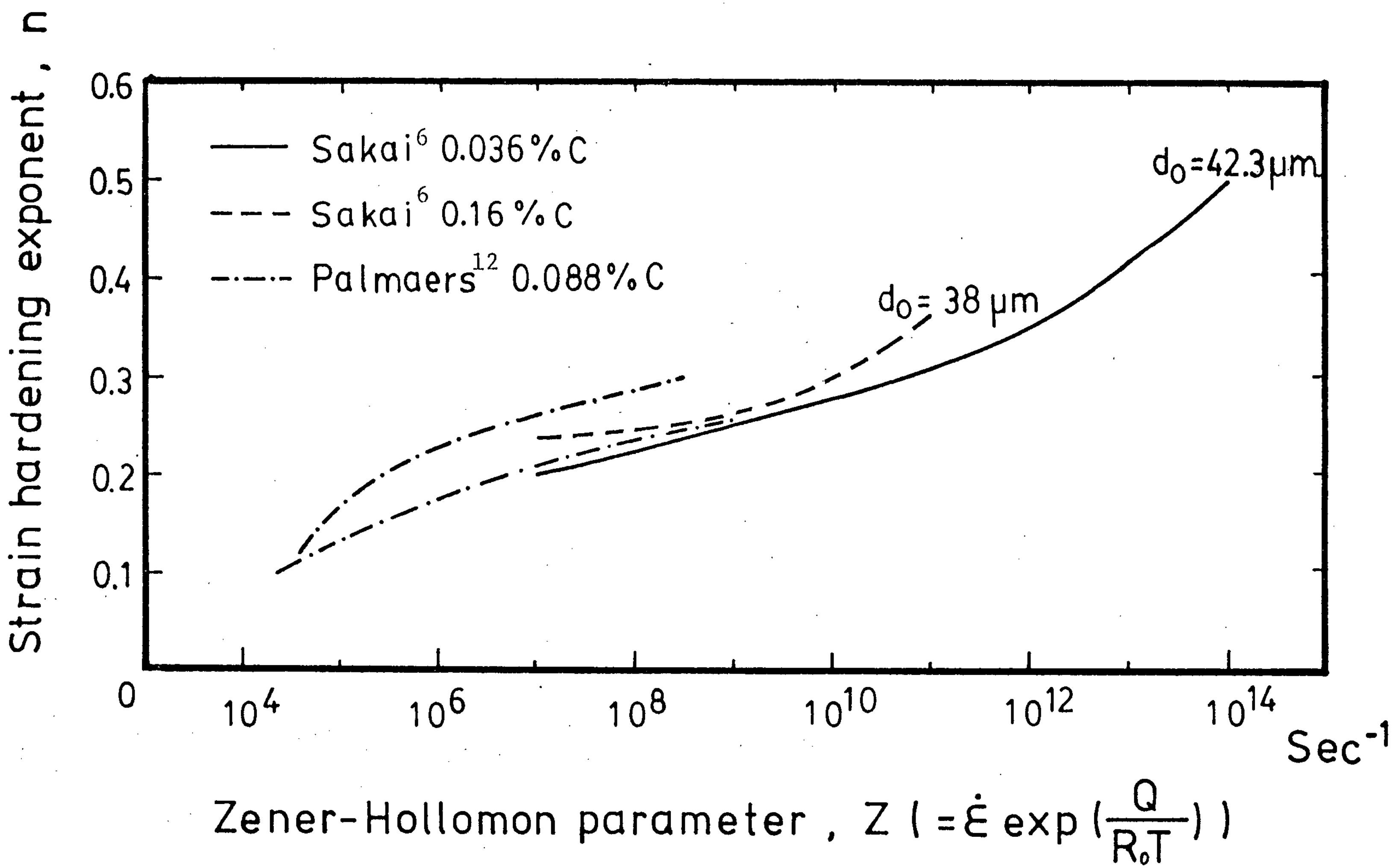

Fig. 3.3 Strain-Hardening Exponent as a Function of Zener-Hollomon Parameter,

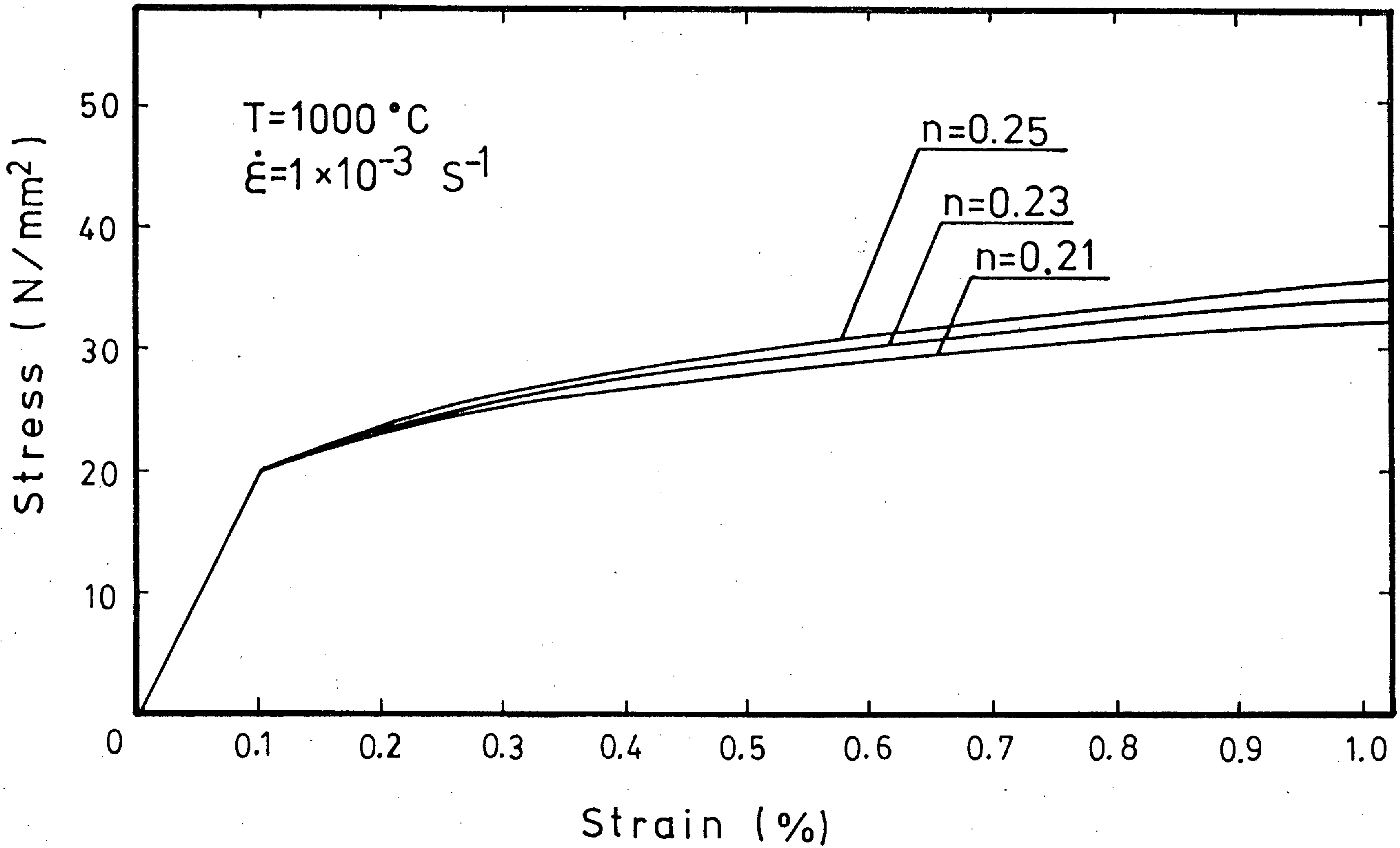

Fig. 3.4 Influence of Strain-Hardening Exponent on the Stress-Strain Curve.

although the grain size is unknown, also shows a monotonic increase of n and is in good agreement with that of Sakai, as shown in Fig.3.3.

Thus for the present study, the strain hardening exponent n was taken from Fig.3.3 by calculating the corresponding Zener-Hollomon parameter Z. The plotted data of n shows some scatter, of about 0.05 in Fig.3.3 but this is unimportant when viewed in terms of the resultant stress-strain curves, as shown in Fig.3.4.

3.3 Model development

Owing to the complexity of the bending/unbending problem certain simplifying assumptions are necessary. The major assumptions adopted here are as follows.

1) The dimension normal to the narrow face is neglected.
2) Creep is neglected.

Thus in the formulation of the model, the two-dimensional finite-element program, EPIC-IV[19], which was developed by Yamada for plane stress/plane strain and axisymmetric problems, has been used with some modification to take into account the moving condition of the slab. The finite-element method is eminently well suited for solving non-linear and complex loading problems.

The validity of these assumptions are examined in detail in the subsequent sections.

3.3.1 Comparison of the three-dimensional and two-dimensional models

To check the adequacy of the two-dimensional model, a three-dimensional elastic analysis was performed and compared with results from the two-dimensional model. A computer program, ELAS65, developed by the Computer Structural Analysis Group of Duke University, was used for the three-dimensional bending analysis of the wide slab.

Assuming symmetry, a half section of a slab was analysed. The slab was considered to be a hollow box with a linear temperature gradient in the through-thickness direction of the shell. The bulging due to ferrostatic pressure of molten steel was excluded in this analysis. A schematic view of the three-dimensional finite-element mesh is shown in Fig.3.5. Calculations were performed for the following conditions.

1) Slab size : $250^{d} \times 1800^{w}$ mm²
2) Shell thickness: 90 mm
3) Roll pitch : 350 mm
4) Bending radius : 10.5 m
5) Mechanical properties:

(outer) ..... T=1045°C, E=18767 MPa, ν =0.36

(middle) .... T=1235°C, E=15278 MPa, ν =0.37

(inner) ..... T=1425°C, E=8163 MPa, ν =0.39

Owing to symmetry, the y-component of displacement was constrained on the longitudinal center plane of the wide face of the slab. In the z-direction, the nodes corresponding to the roll supporting points were constrained. The upstream edge plane perpendicular to the casting direction was loaded with bending moments but kept planar after deformation, while the downstream edge plane was left free.

Fig.3.6 shows the resultant deformation due to bending, and Fig.3.7 shows the strain distribution in the cross section of the slab. Thus it is clear that the wide face shells of the slab bend about their individual neutral axes and therefore can be regarded as independent of the narrow face. This trend may be attributed to the temperature distribution in the shell and the strand aspect ratio(w/d) for the case analysed.

Fig.3.8 shows a comparison of the results of this analysis obtained with the two-dimensional elastic model(plane stress) of the center plane of the wide face. It is evident that there is good agreement. If plastic behavior were to be included, the mid-face would act even more independently of the edges. Therefore it can be concluded that the two-dimensional model, assuming plane stress, is sufficient for the

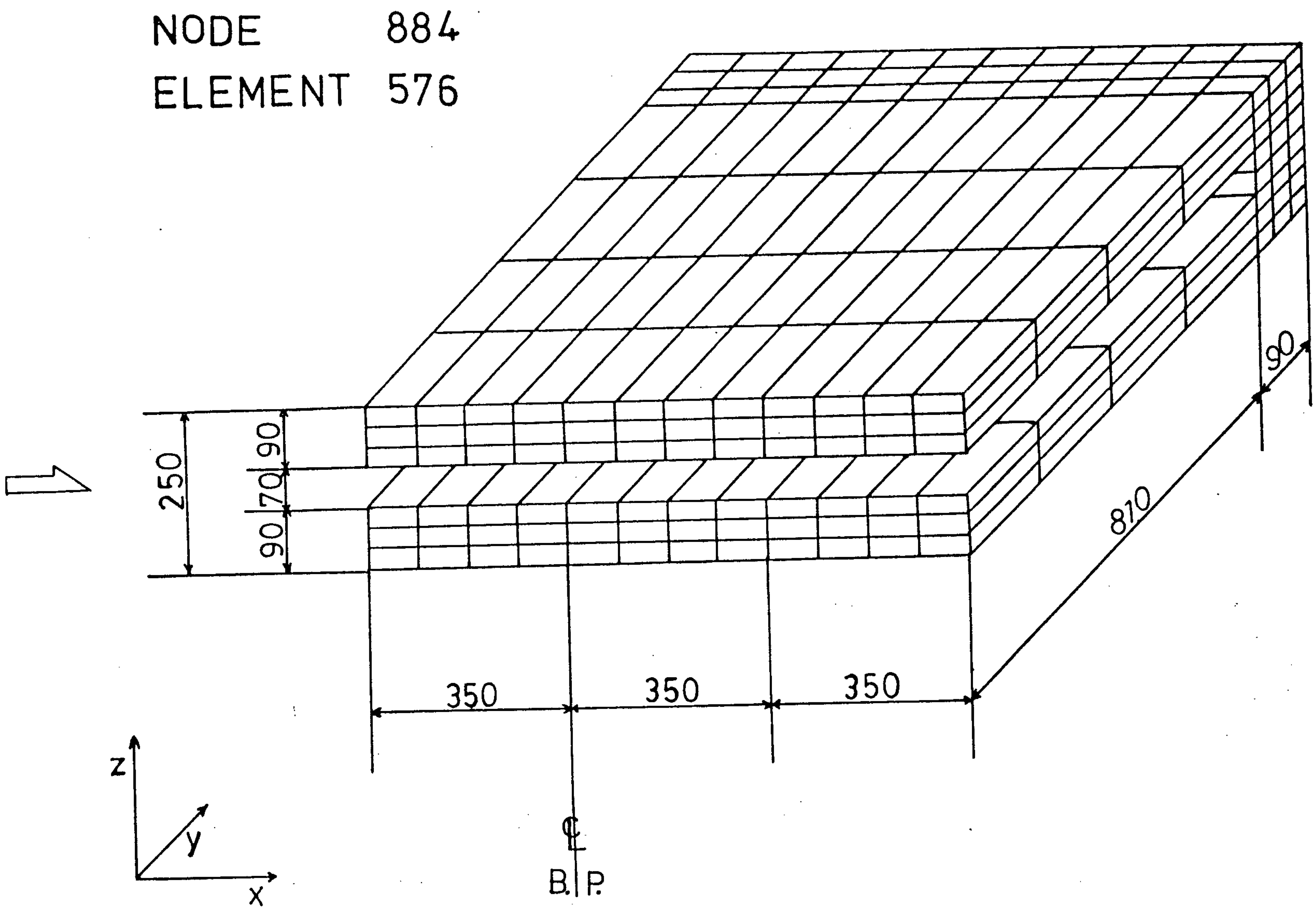

Fig. 3.5 Schematic Diagram of the Three-Dimensional Finite-Element Mesh for the Bending Analysis.

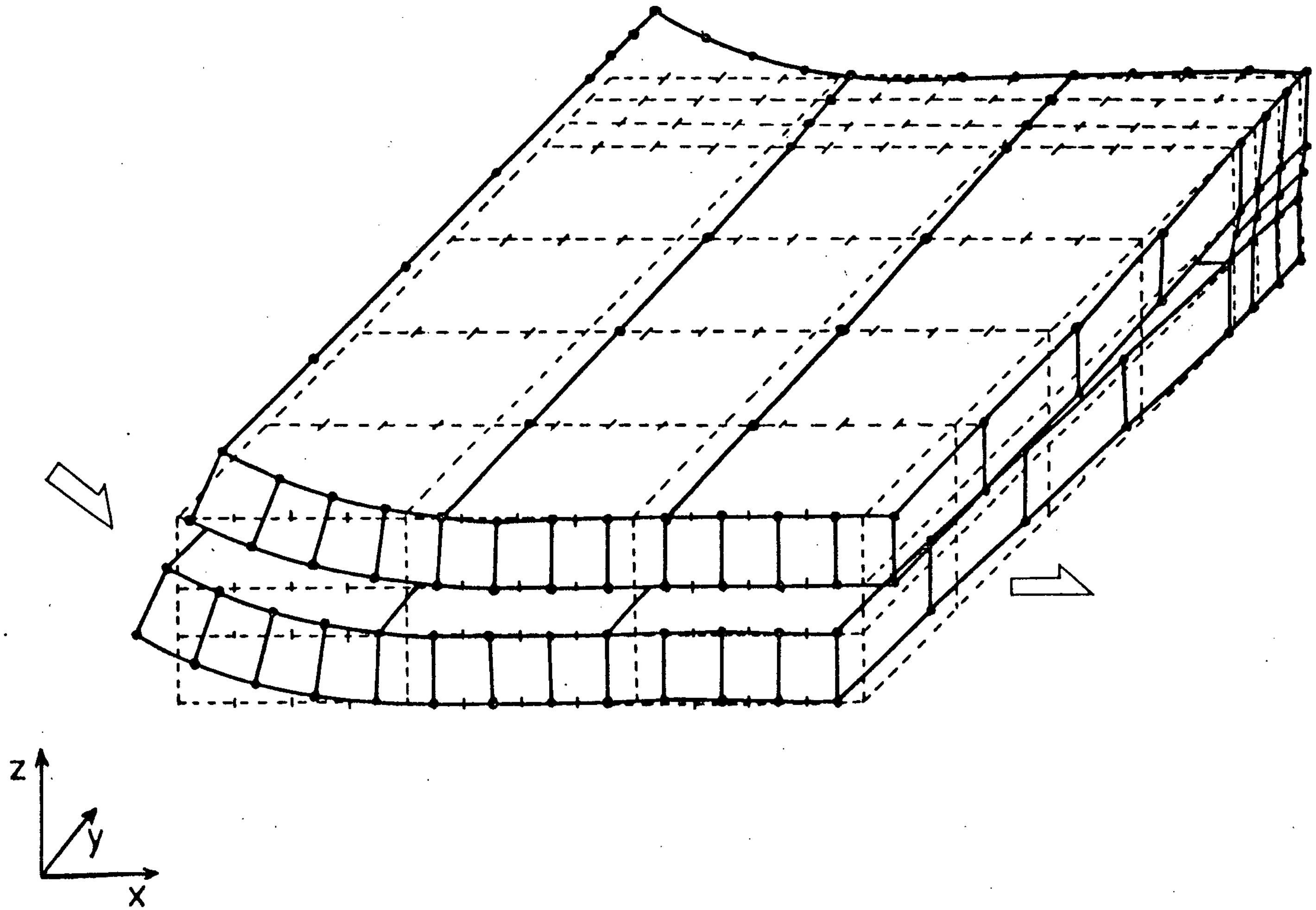

Fig. 3.6 Predicted Distortions of the Slab by the Three-Dimensional Finite-Element Bending Analysis.

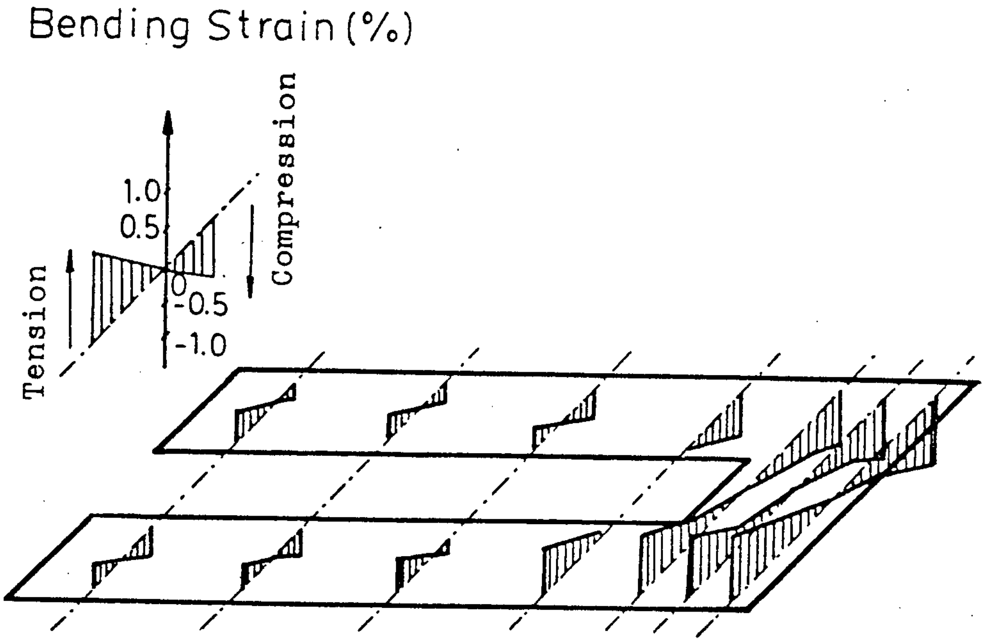

Fig. 3.7. Predicted XX-STRAIN Distribution in the Cross Section of the Slab by the Three-Dimensional Finite-Element Bending Analysis.

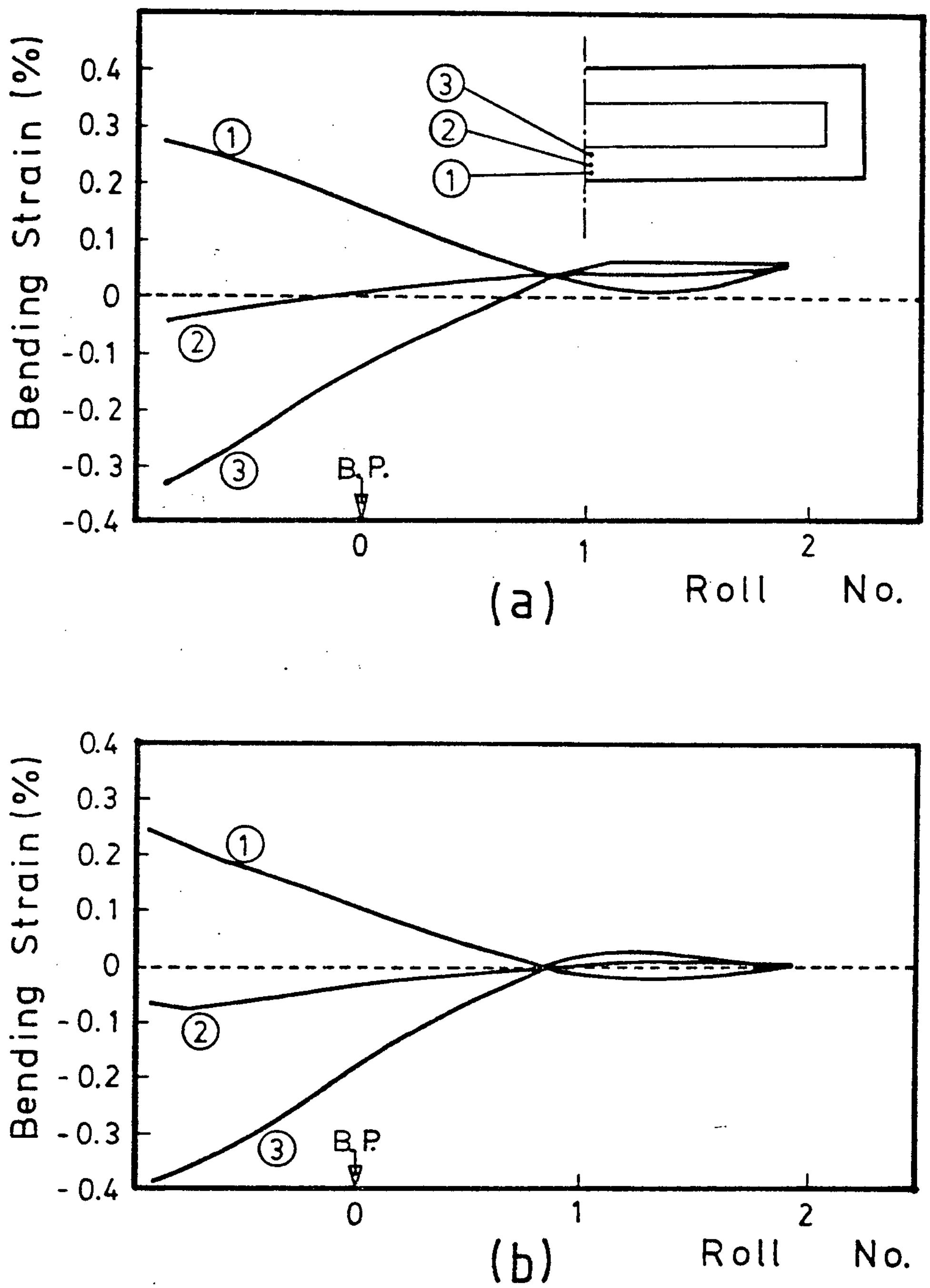

Fig. 3.8 Comparison of Bending Strains Between (a) Three-Dimensional and (b) Two-Dimensional Model.

bending/unbending analysis on the center plane of the wide face of the slab.

3.3.2 Effects of creep in calculations of bulging

In the following section the effect of neglecting creep in the bulging analysis on the accuracy of the calculations has been evaluated. This is accomplished by examining the results of several studies on bulging in continuously cast slabs which have included creep.[12,15,20-27]

Grill and Schwerdtfeger[22] calculated bulging accounting for primary creep using a finite-element model and compared their results with the results obtained with an elasto-plastic model reported by Emi and Sorimachi[20] (see Fig.3.9). It is evident from this comparison, that the elasto-plastic model predicts lower values of bulging at large roll spacings than the model which includes creep but at small roll spacings(less than 40 cm) and for small values of bulging(δ_{max} <1 mm), the difference between the results of the two methods is negligible.

To check the validity of the elasto-plastic model for the bulging analysis, a comparison of model predictions to the data of Wunnenberg[27] and Morita [26] was considered. However because Wunnenberg made measurements with large roll spacings, only the data of Morita , shown in Table II was used. For

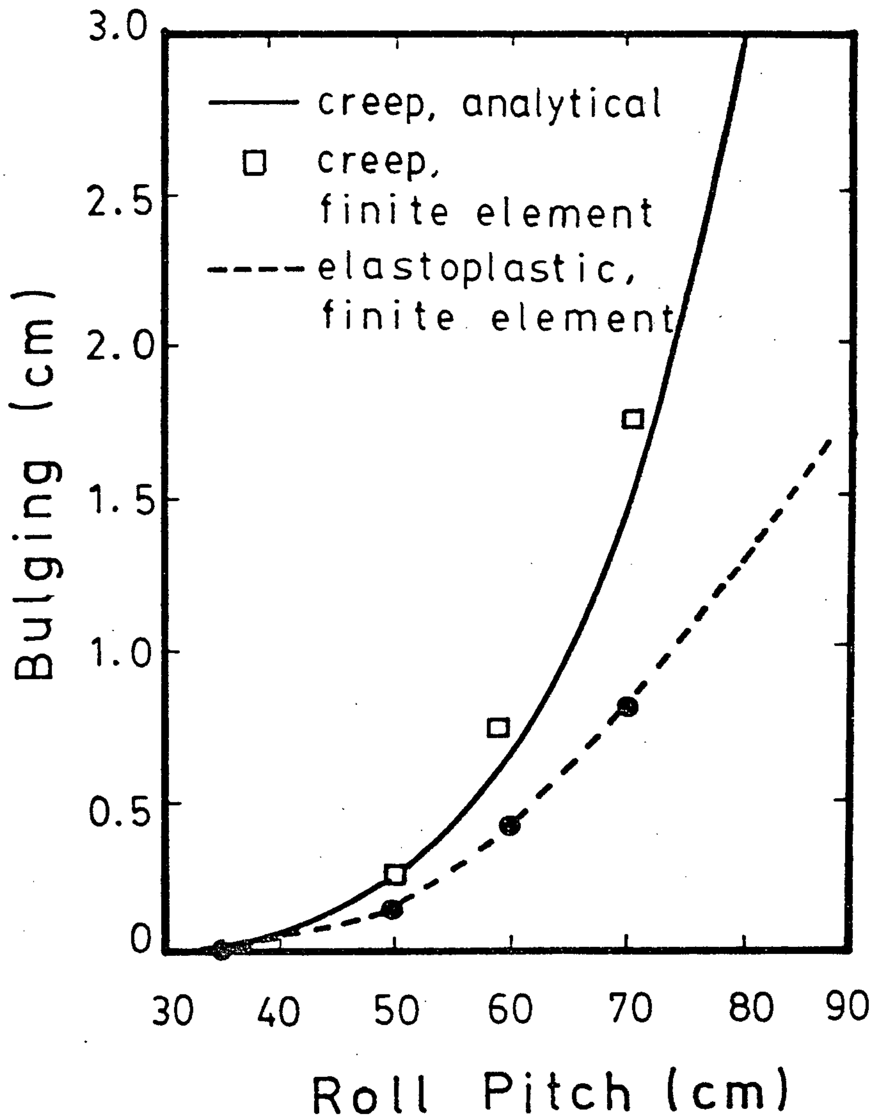

Fig. 3.9 Comparison of Maximum Bulging Predicted by the Creep Model and Elasto-Plastic Model.[22]

comparison purposes the finite-element mesh shown in Fig.3.10 was selected for the elasto-plastic analysis.

Table II Measured data of bulging by Morita[26]

Kind of steel	Si-killed(40kg/mm^2) steel grade
Size	230x1230 mm^2
Casting speed	1.1 m/min
Shell thickness	55 mm
Surface temperature	1000-1050 °C
Roll pitch	399 mm
Ferrostatic head	7.933 m(0.54MPa)
Bulging	0.2-0.4 mm

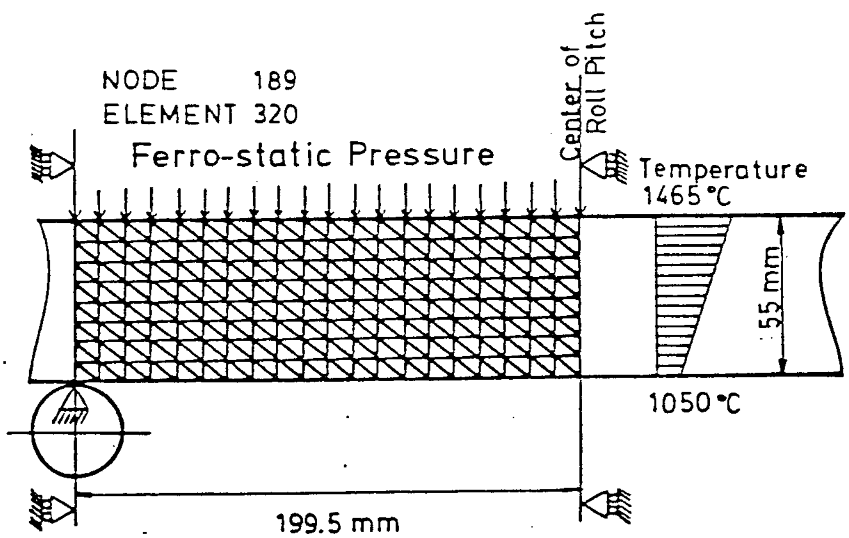

Fig. 3.10 Schematic Diagram of the Two-Dimensional Finite-Element Mesh for the Bulging Analysis.

Mechanical properties were obtained from the data shown in Figs.3.2, and 3.3(see Section 3.2) assuming a uniform strain rate of 1×10^{-3} s^{-1} (Appendix I). The results of the plane stress and plane strain calculations are shown in Fig.3.11. The bulging assuming plane stress is usually larger than that based on plane strain and the differences become more pronounced with increased bulging. The agreement between the elasto-plastic analysis and the measured bulging is reasonably good. The plane stress condition which has been commonly used in bulging analysis by many authors was adopted in the present study. Strictly speaking,the validity of this condition will depend on the degree of restraint the edge exerts on the deformation at the center of the wide face of the slab.

Thus the elasto-plastic model has been shown to be reasonably accurate for calculating bulging under conditions of small roll spacings; in a modern slab caster roll spacings are approximately 30-40 cm. Under transient conditions such as during interruption of casting the creep model will be necessary however.

Another important effect of creep on bulging is that the location of the maximum bulging shifts from the midpoint between rolls to the downstream as a result of interaction between strand movement and creep deformation.[22,23,25,27] This causes an asymmetric bulging deformation but the influence on the maximum deflection is small. Therefore this effect was also neglected in the present study.

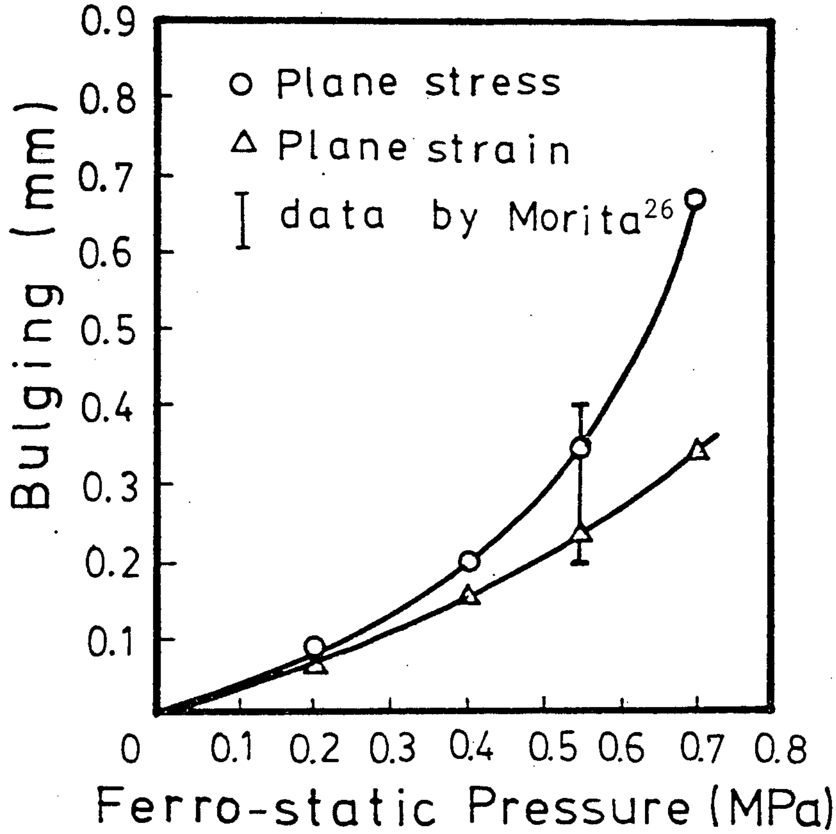

Fig. 3.11 Comparison of Bulging Strains Predicted by the Plane Stress and Plane Strain Finite-Element Analysis.

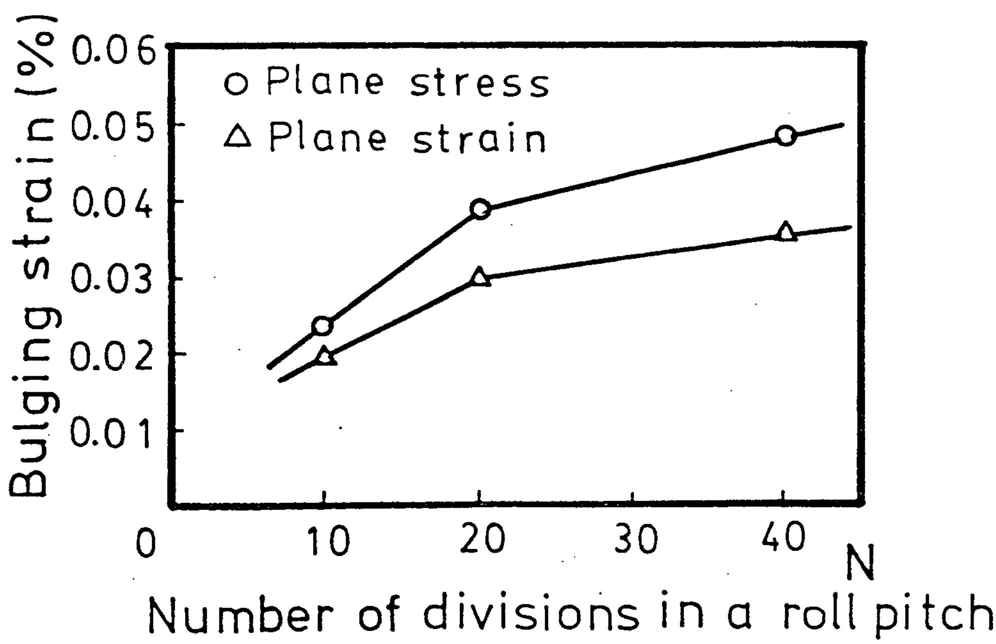

Fig. 3.12 Influence of the Mesh Size on Bulging Strain in the Elasto-Plastic Finite-Element Analysis.

In a finite-element analysis, mesh size has a significant influence on the results. The effect of mesh size in the casting direction has been evaluated and the results are shown in Fig.3.12. The conditions employed in the earlier calculations have been utilized for this evaluation. Thus twenty divisions in a roll pitch can be regarded as a sufficiently fine mesh for the purpose of this study since there is little change in the calculated results beyond this point. Moreover the use of more divisions will result in a prohibitively high computing cost.

Based on these assumptions the bending/unbending analysis combined with bulging was carried out using a two-dimensional(plane stress),elasto-plastic,finite-element model. Details of the model are presented in subsequent sections.

3.3.3 Two-dimensional elasto-plastic Finite Element

In the finite-element method a continuum is approximated by an assemblage of elements which are interconnected at a finite number of joints or nodal points. By satisfying equilibrium of forces, compatibility of displacements and the stress-strain law for the material, it is possible to generate a set of linearly independent equations that can be solved simultaneously for the displacements at nodal points. These can then be used to obtain the stress strain distribution in the assemblage of elements. The mathematical basis of the elasto-plastic finite-element is described in Appendix II and III.

The computer program "EPIC-IV"[19] has been used in the present study. The main characteristics of this program are:

1) Three-noded linear triangular elements are used.
2) The iterative method (Conjugate Gradient method) is adopted to solve the matrix inversion.
3) Isotropic hardening of the material is assumed in plasticity.
4) The incremental method (tangent modulus method) is adopted to simulate material non-linearity.
5) Unloading is checked at every stage of the calculation(Appendix III).

The iterative matrix inversion procedure greatly reduces the computing time for a non-linear problem. The disadvantage of this technique is that when the matrix to be inverted approaches singularity(i.e. plastic instability) the convergence deteriorates.

In order to use this program the following modifications were made. To facilitate the semi-dynamic simulation, the main routine which controls the subroutines was changed. By this modification a shift in the boundary condition (roll supporting points) was made possible. Secondly, sub programs for plotting the results were formulated as a post data processor. The following plots are available: finite-element mesh, deformations, principal strain vectors and contour maps of stresses and strains.

To check the accuracy of the program,the stress/strain distribution in a thick-walled cylinder under internal pressure was computed and compared with the analytical solution by Hill(Appendix IV).

3.3.4 Boundary conditions

The longitudinal center plane of the wide face of a slab has been modelled. Fig.3.13 shows a schematic view of the plane of interest. Three and one half roll pitches in the straightening zone were modelled and the upper and lower shells of this domain were analysed separately using the following boundary conditions.

1) The x- and y-components of the displacements of the nodes on the downstream edge were set equal to the values of geometrical displacements based on simple beam bending theory.
2) The y-component of displacement of roll supporting points were constrained. The y-component of nodes along AB and CD were also constrained(Fig.3.13), since straightening is assumed to be completed within the first roll pitch downstream from the bending

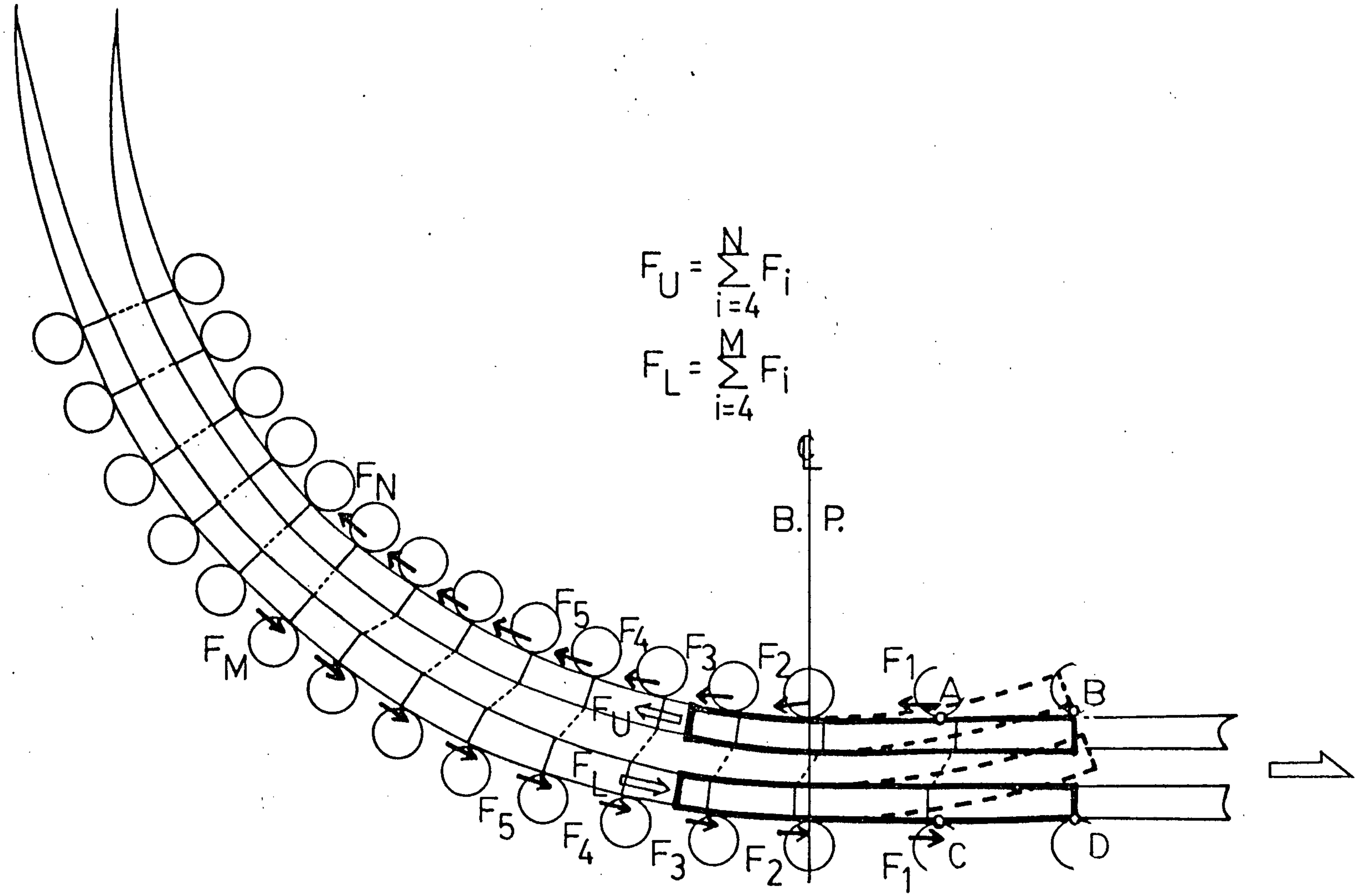

Fig. 3.13 Schematic Diagram of the Boundary Conditions Adopted in the Two-Dimensional Finite-Element Bending Analysis.

point.[31]

3) The roll friction forces caused by bending deformation were uniformly distributed between adjacent rolls.(Coefficient of roll friction was assumed to be 0.45)

4) The upstream edge of the shell was constrained through the force boundary condition; this is equivalent to the constraint force from the remaining domain.

5) The roll points were shifted once in the bending analysis and the above boundary conditions were reapplied.

3.3.4.1 <u>Roll friction force</u>

The cross section perpendicular to the casting direction does not remain planar after the bending deformation(see Fig.3.6 of Section 3.3.1). If the section under consideration were free at the ends, the center plane of the wide face of the upper shell would move downstream relative to the narrow face during unbending, while the center plane of the lower shell would move upstream. This tendency of the center plane to move relative to the narrow face is opposed by frictional forces between the rolls and the strand surface, see Fig.3.13.

The roll friction force has been estimated according to the following steps:

1) Calculate the average movement of the downstream edge $,\overline{u}_x$.

2) Assume the number of rolls,N, necessary to absorb the above displacement,$\overline{u}_x$.

3) Calculate the cumulative roll friction forces, $\sum_{i=1}^{N} F_i$.

$$F_i = \mu \cdot p_i \cdot l_{Ri} \tag{12}$$

where p_i : ferrostatic pressure

l_{Ri} : roll pitch

μ : frictional coefficient (=0.45)

4) Convert ΣF_i to stress σ_i at each roll point.

$$\sigma_i = (\sum F_i/\mathrm{Shell}) \times 4 \tag{13}$$

(stress σ_i is the total of four layers of different materials.)

5) Decide strain ε_i corresponding to the stress σ_i from the stress-strain curve.

6) Calculate elongation Δl from strain ε_i.

$$\Delta l_i = l_{Ri} \cdot \varepsilon_i \cdot 10^{-2} \tag{14}$$

7) Repeat procedures from 2) until final convergence is achieved.

$$\sum_{i=1}^{N} l_i = \overline{u}_x \tag{15}$$

Appendix V presents an example of this calculation of Case 1(see Table III of Section 4), where the value of $\overline{u}_x$ is 8.86 mm and N is 11.

The value of the coefficient of roll friction strongly affects the resultant bending strain as shown in Fig.3.14. the calculation conditions for which are the same as in Case 2(see Table III of Section 4). Unfortunately there is no measured data available for the coefficient of roll friction for the continuous casting of slabs. The value of 0.33 has been adopted empirically for the design of driving rolls; however this value appears to be an underestimate to provide a margin of safety in the design. In the present analysis, therefore, the data summarized by Schey[32] for hot rolling was used, see Fig.3.15. The friction is seen to decrease with increasing temperature; and therefore the iron oxide film thickness is reported to be one of the main variables which affects friction. The value of 0.45(see Fig.3.15, Pavlov in air) corresponding to the surface temperature of 950°C was adopted for the present analysis, since in the one-point bending bow-type casters the surface temperature of the strand ranges from about 900°C to 1000°C at the bending point.[12]

3.3.4.2 Shift of the boundary condition

To take into account the effects of a moving

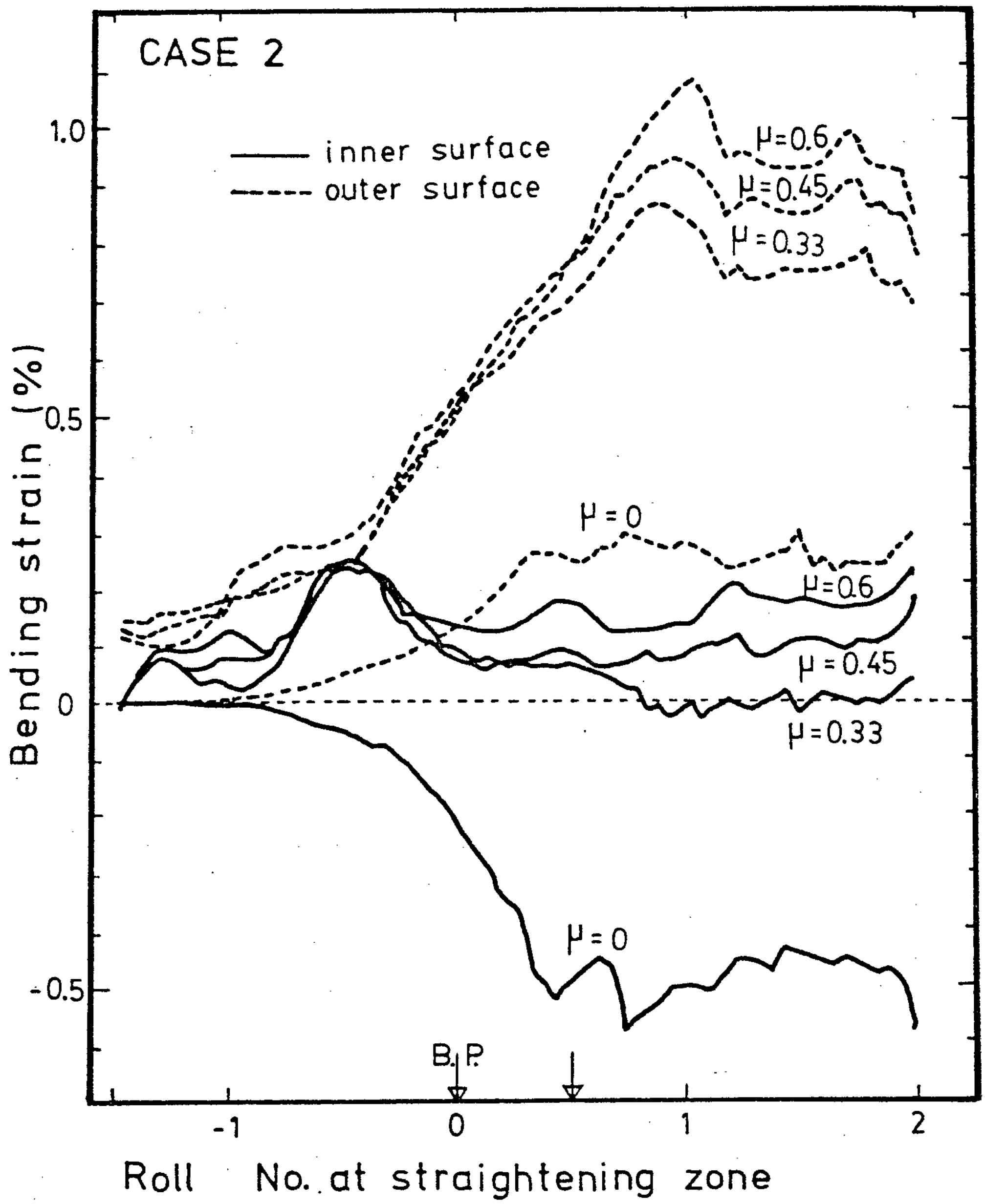

Fig. 3.14 Influence of Coefficient of Roll Friction on the Resultant Bending Strain.

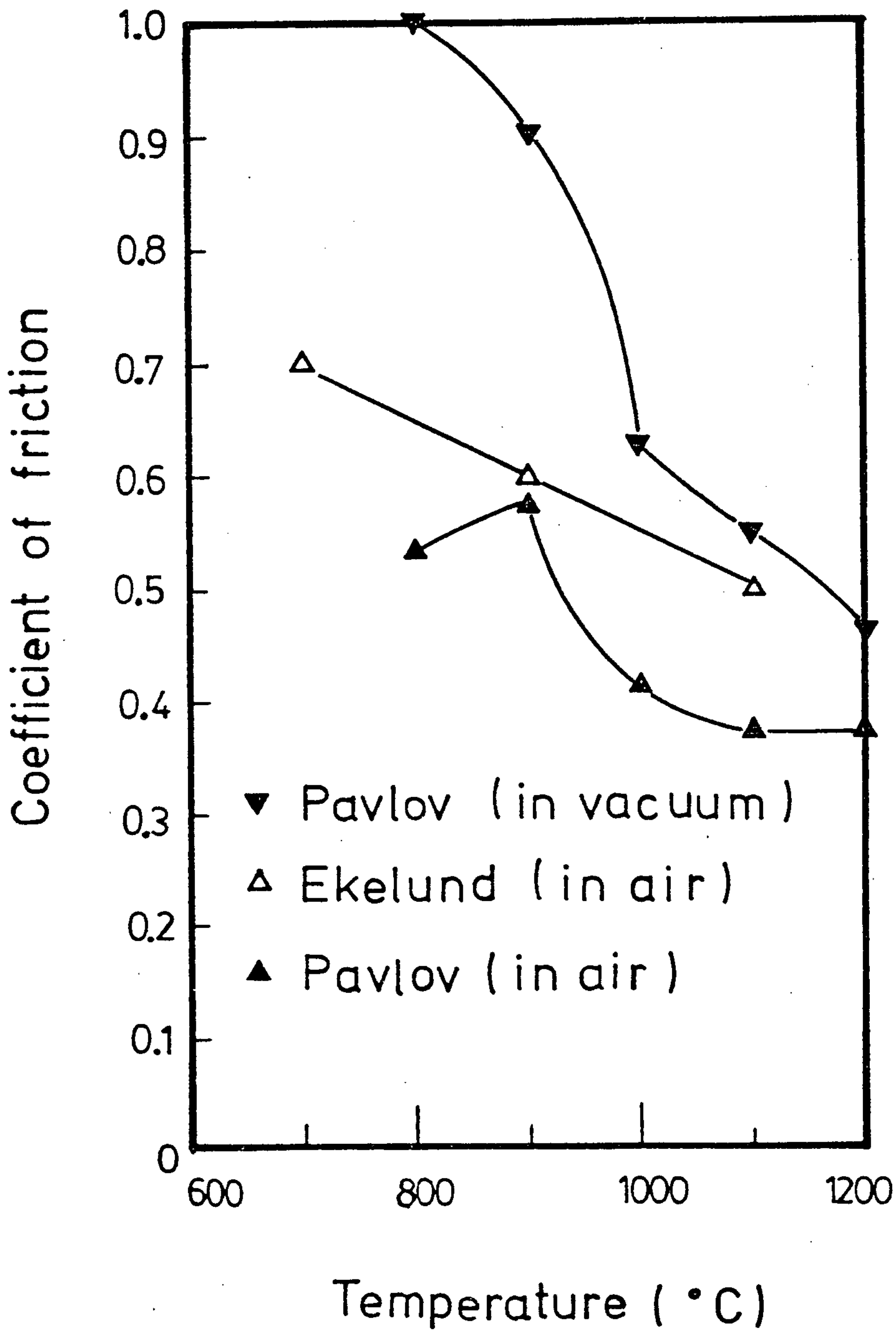

Fig. 3.15 Coefficient of Roll Friction of Hot Rolling as a Function of Temperature.[32]

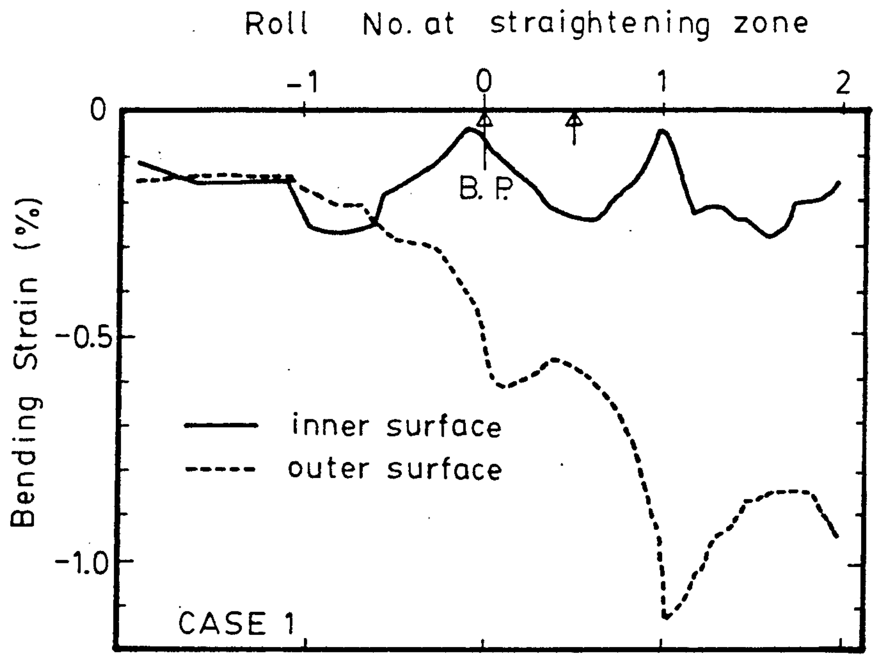

Fig. 3.16 Predicted Bending Strain with the One-Step Bending Model.

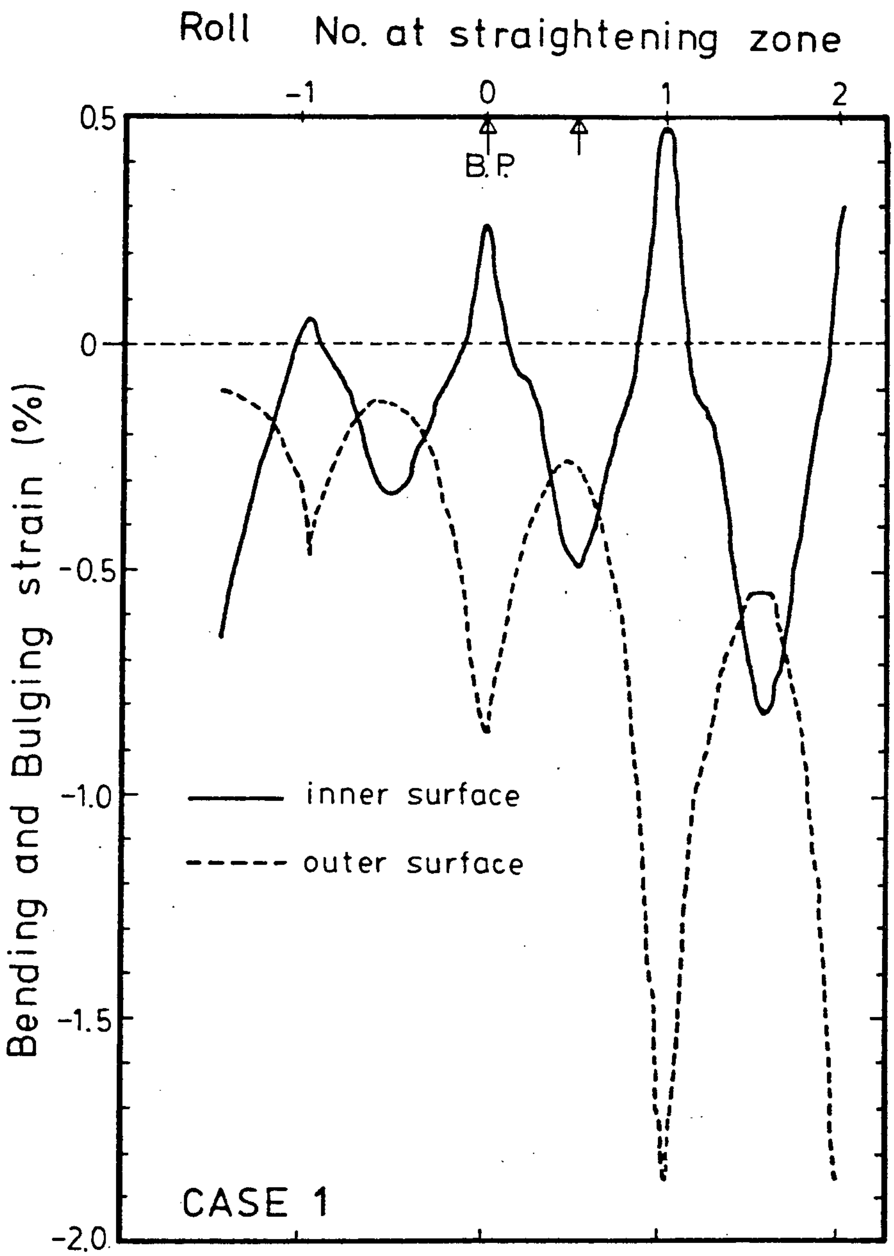

Fig. 3.17 Predicted Bending and Bulging Strain with the One-Step Bending Model.

strand, the roll points were shifted during bending. For a complete dynamic modelling it is necessary to shift roll points by small steps; however this results in a prohibitively high computing cost. In the present analysis, the roll points have been shifted only once during bending and hence the strand was bent in two-steps around the two bending points(see Fig.4.9 of Section 4). A significant difference was observed in the results of two-step bending compared to those of single-step bending, especially in the case of the lower shell. Compare Figs.3.16,3.17 with Figs.5.12,5.20 (Chapter 5) and note that the bending strain distribution in the inner and outer surface are smoother for the case where a two-step bending calculation procedure was employed. In the case of the one-step bending calculation, peak strains appear in the inner surface which were magnified as a result of interaction between bending and bulging ,see Figs.3.16,3.17. It is believed these peak strains cause a significant error in the results of one-step bending.

3.3.5 Calculation flow

Figs.3.18 and 3.19 shows the flow chart for the calculation. "Bending" and "bending plus bulging" were calculated separately. Each calculation consists of two steps,i.e. first-step bending and second-step bending, see Fig.3.18. After the first-step bending,roll points were shifted by a half pitch to set new boundary and loading conditions for the second-step bending analysis. The nodes of the former roll points were unloaded to allow for a spring back. The nodes of the new roll points were loaded with the displacements, u_Y, to push the strand back to simulate roll constraint at the new roll points.

In the calculation of "bending plus bulging", ferrostatic pressure was loaded in the second-step bending stage.

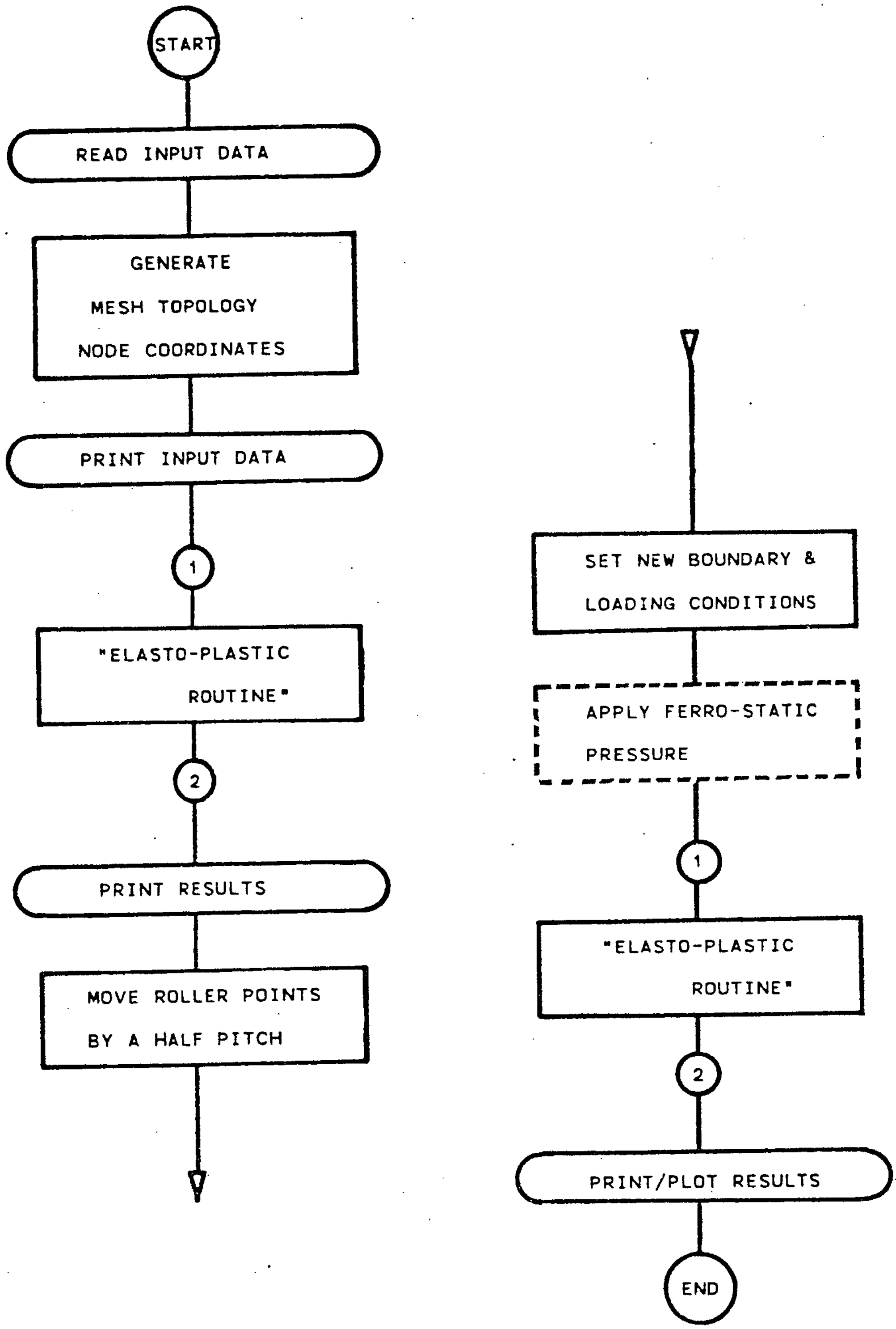

Fig. 3.18 Flow Chart for the Calculation of the Bending and Bulging Strain.

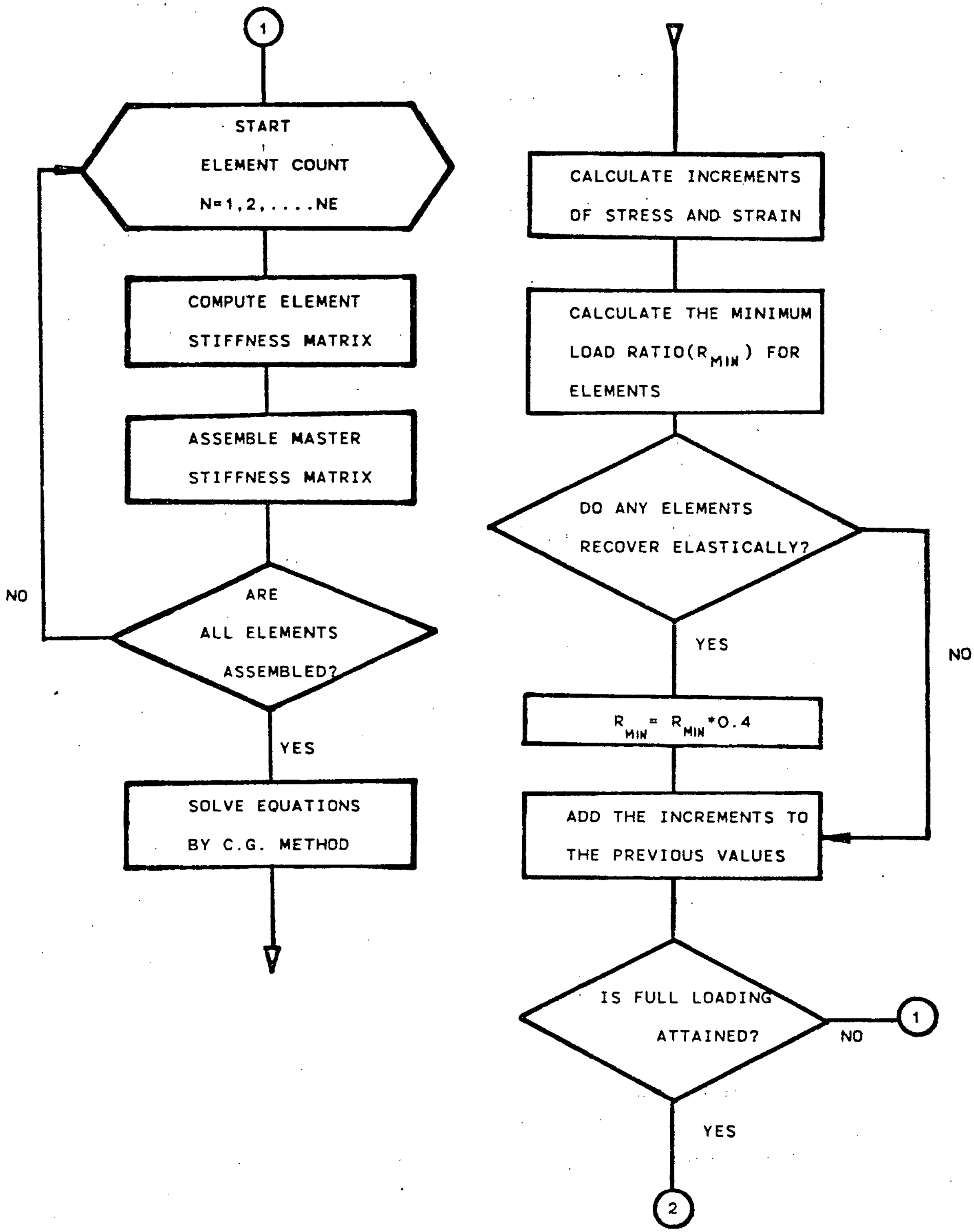

Fig. 3.19 Flow Chart for the Calculation of the Bending and Bulging Strain. ("Elasto-Plastic Routine")

Chapter 4

CALCULATION CONDITIONS

Calculations have been performed only for one-point bending bow-type casters in an attempt to obtain a fundamental understanding of bending/unbending of continuously cast slabs. Multi bending bow-type casters have not been considered since analysis of such machines should allow for stress relaxation due to creep thus making creep analysis mandatory. The main parameters that were investigated with the computer model are as follows;

1) Machine Radius, R
2) Roll Pitch, l_R
3) Casting Speed, V
4) Shell Thickness, s
5) Surface Temperature, T_0
6) Ferrostatic Pressure, p

However the three parameters - ferrostatic pressure, shell thickness and surface temperature are not independent variables; the latter two are dependent upon machine radius and casting speed whilst ferrostatic pressure is only dependent upon machine radius. The shell thickness and surface temperature have been obtained from the plant data at Oita works(NSC)[46], where the surface temperature has been smoothened for simplification. A plot of shell thickness and mid-face temperature against time (= axial distance/casting speed) is shown in Fig.4.1.

The design and operating conditions of the slab caster at Oita works of Nippon Steel Corporation, NSC[35], were chosen as a base case for the calculation to enable a comparison to be made between model predictions and plant data on internal cracks resulting from the unbending. The machine specifications of Oita No.4 caster are as follows(see also Fig.4.2);

I) machine radius : 10.5 m

II) roll pitch : 471 mm

III) slab size : $250^{d} \times 1300 - 1900^{w}$ mm

IV) chemical composition of slab

(Al-Si-killed(40kg/mm²) steel grade):

0.15/0.19%C,0.10/0.30%Si,

0.70/0.90%Mn,0.025%≥P,0.015%≥S,0.01/0.04%T,Al

V) threshold casting speed for bending internal cracks:

1.1 - 1.2 m/min.

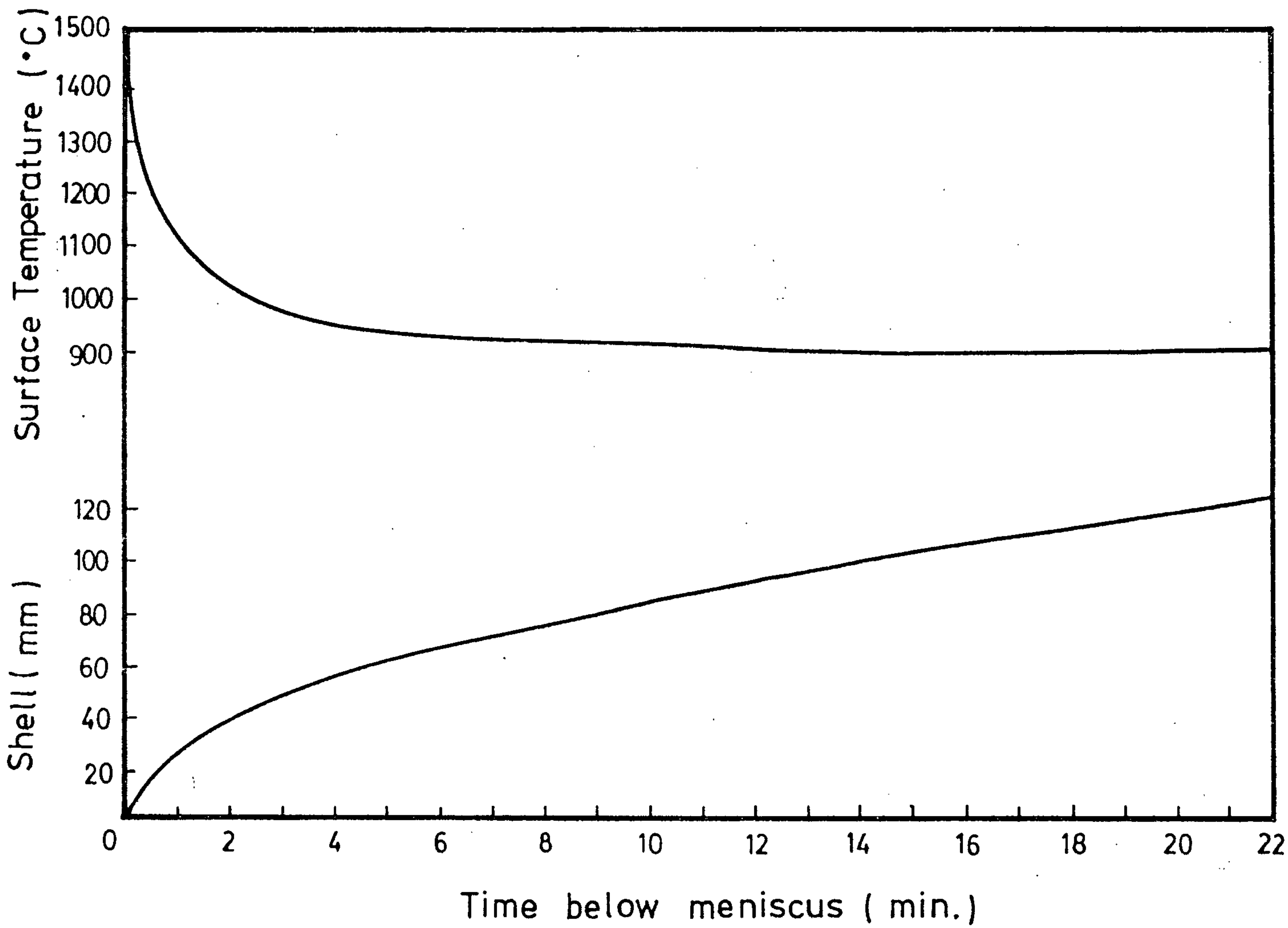

Fig. 4.1 Surface Temperature and Shell Thickness in the Continuous Casting of Slab.

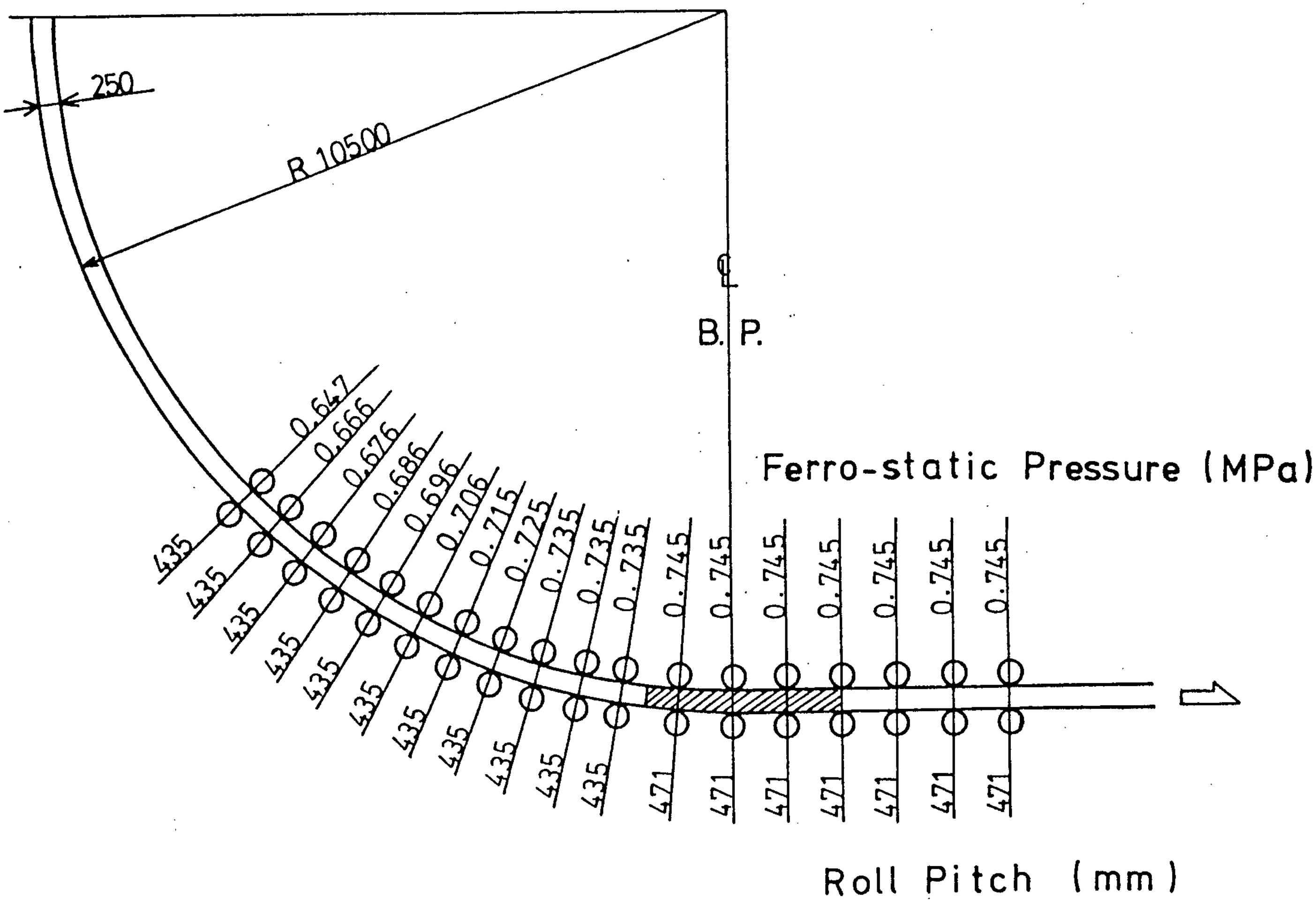

Fig. 4.2 Roll Profile of the 10.5 m Radius Caster,

Table III Calculation conditions for unbending of continuously cast slabs.

	Machine Radius R m	Roll Pitch ℓR mm	Casting Speed V m/min	Shell Thickness S mm	Surface Temp. To °C	Ferrostatic Pressure p MPa
CASE 1. U,L	10.5	471	1.6	83	930	0.74
2. U	10.5	471	1.2 *	97	900	0.74
3. U,L	10.5	471	1.0	106	900	0.74
4. U	10.5	471	1.2	97	990	0.74
5. U	10.5	471	1.2	97	850	0.74
6. U	10.5	400	1.2	97	900	0.74
7. U	10.5	540	1.2	97	900	0.74
8. U	8.0	471	0.9	97	900	0.56
9. U	8.0	471	1.2	83	900	0.56
10. U	13.0	471	1.47	97	900	0.91

U : upper shell , L : lower shell

* : threshold casting speed for internal cracks

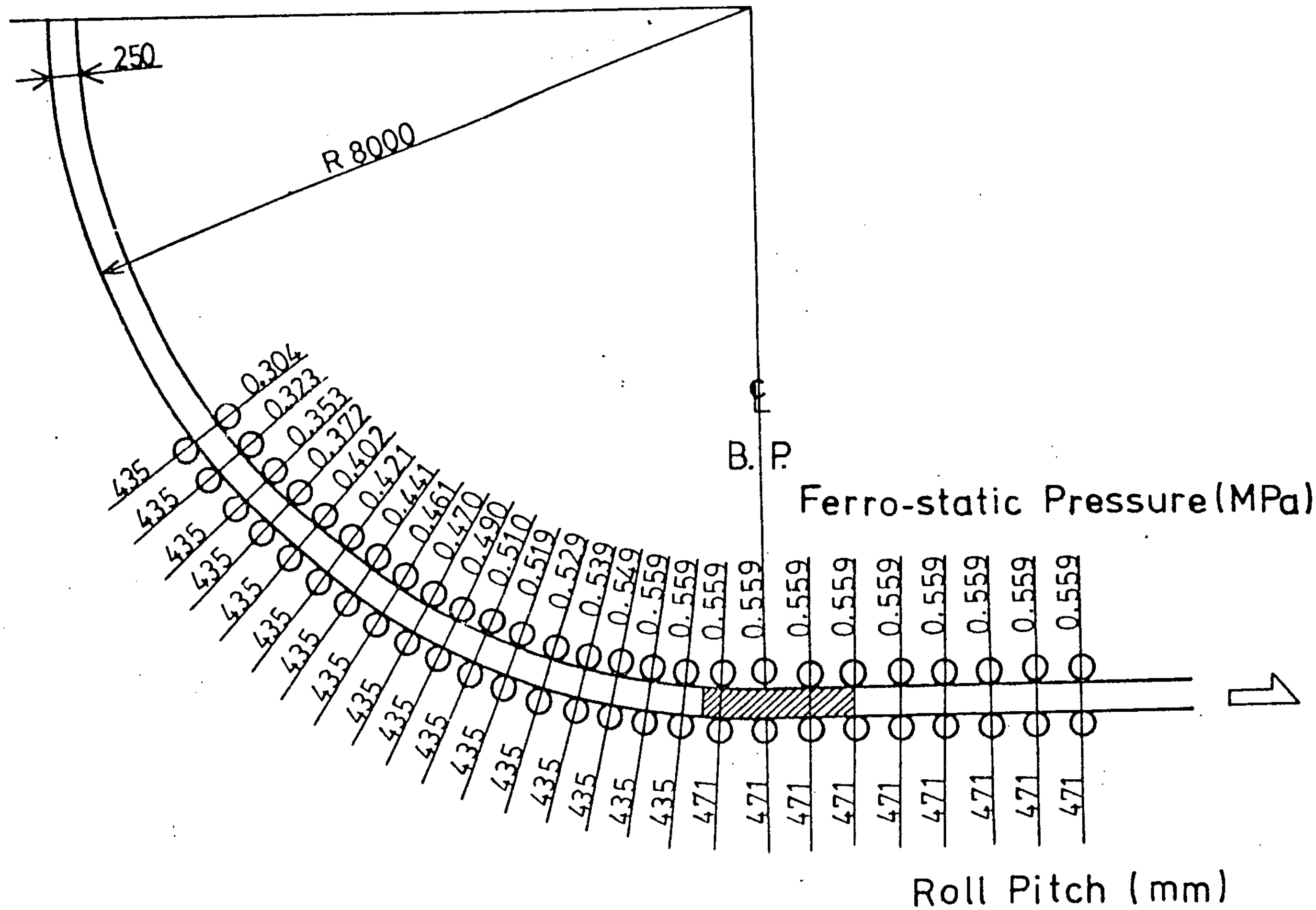

Fig. 4.3 Roll Profile of the 8.0 m Radius Caster.

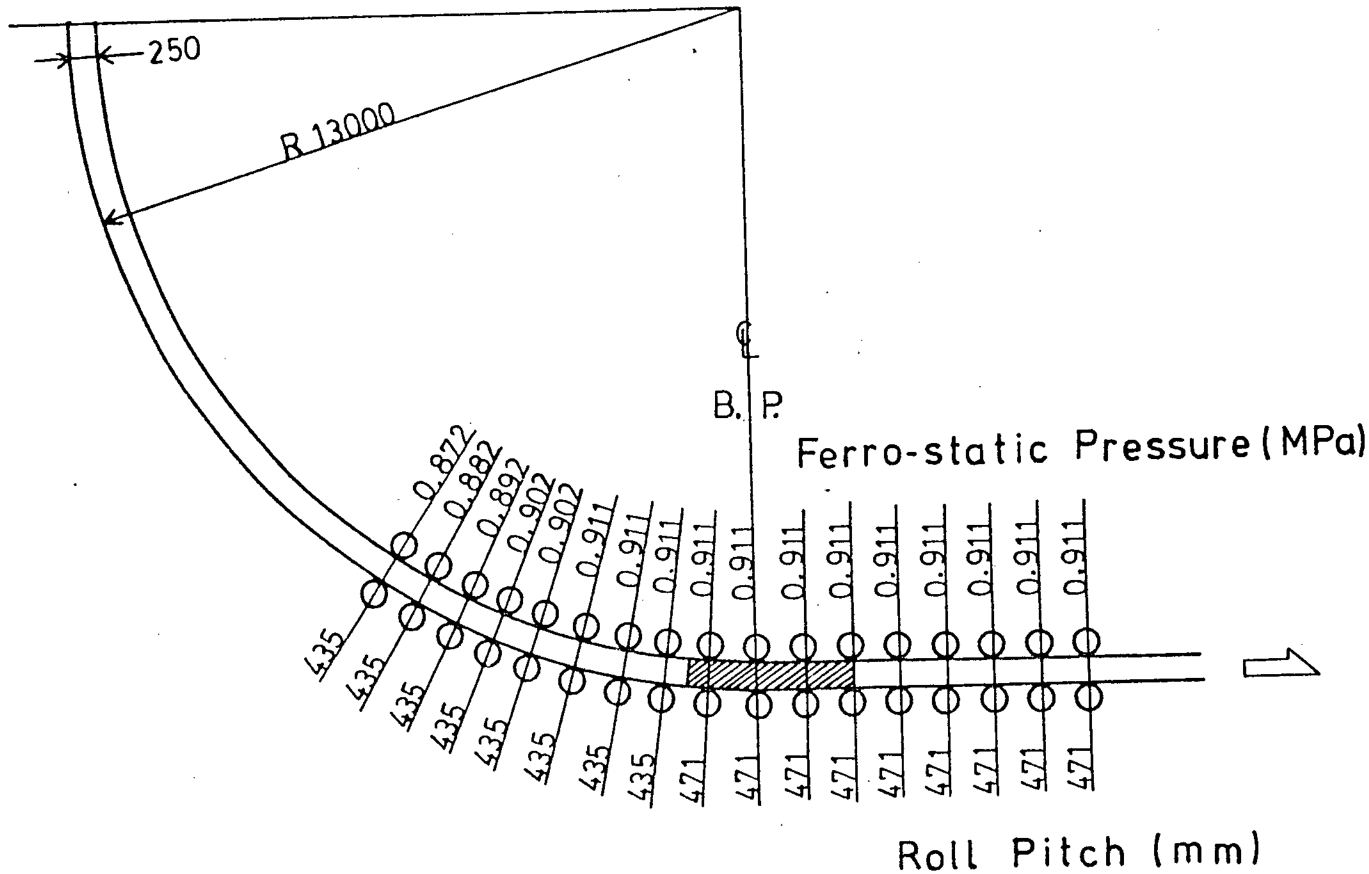

Fig. 4.4 Roll Profile of the 13.0 m Radius Caster.

The conditions which were investigated in the present study are given in Table III. The slab thickness was kept constant at 250 mm for all cases. In Cases 1,2 and 3, the casting speed was varied to evaluate the critical strain necessary for generation of internal cracks. In Cases 4 and 5, the surface temperature was artificially changed using the same conditions as in Case 2; and in Cases 6 and 7, the roll pitch was changed. In Cases 8,9 and 10, machine radii of 8 m and 13 m were studied; the roll configuration for these hypothetical machines is shown in Figs.4.3 and 4.4.

The temperature distribution through the shell thickness has been assumed to be linear with the inner shell surface at the solidus temperature of Al-Si-killed ($40kg/mm^2$)steel grade - 1487°C[33]. Based on temperature distributions calculated separately with a heat-flow model , this assumption is very reasonable. The temperature and shell thickness were assumed to be uniform in the casting direction over the three-and-one-half roll pitches being considered by the model. This again is a very reasonable approximation.

The mechanical properties for the above temperature distribution have been calculated from the mechanical property data shown in Figs.3.2 and 3.3(see Section 3.2.2) and different properties were assigned to each of the four layers into which the shell was divided. To determine the strain hardening exponent,n,the strain rate in each of the layers was calculated by considering the neutral plane of bending to be halfway through the slab thickness. Strictly speaking the real strain rates must be used to determine n, however this approximation is sufficient since the data of n itself has some scatter as shown in Fig.3.3. Figs.4.5 to 4.8 show the stress-strain curves calculated by this procedure.

The finite-element mesh for this calculation is shown in Fig.4.9. The total number of nodes amounted to 536 and the number of elements equalled 924.

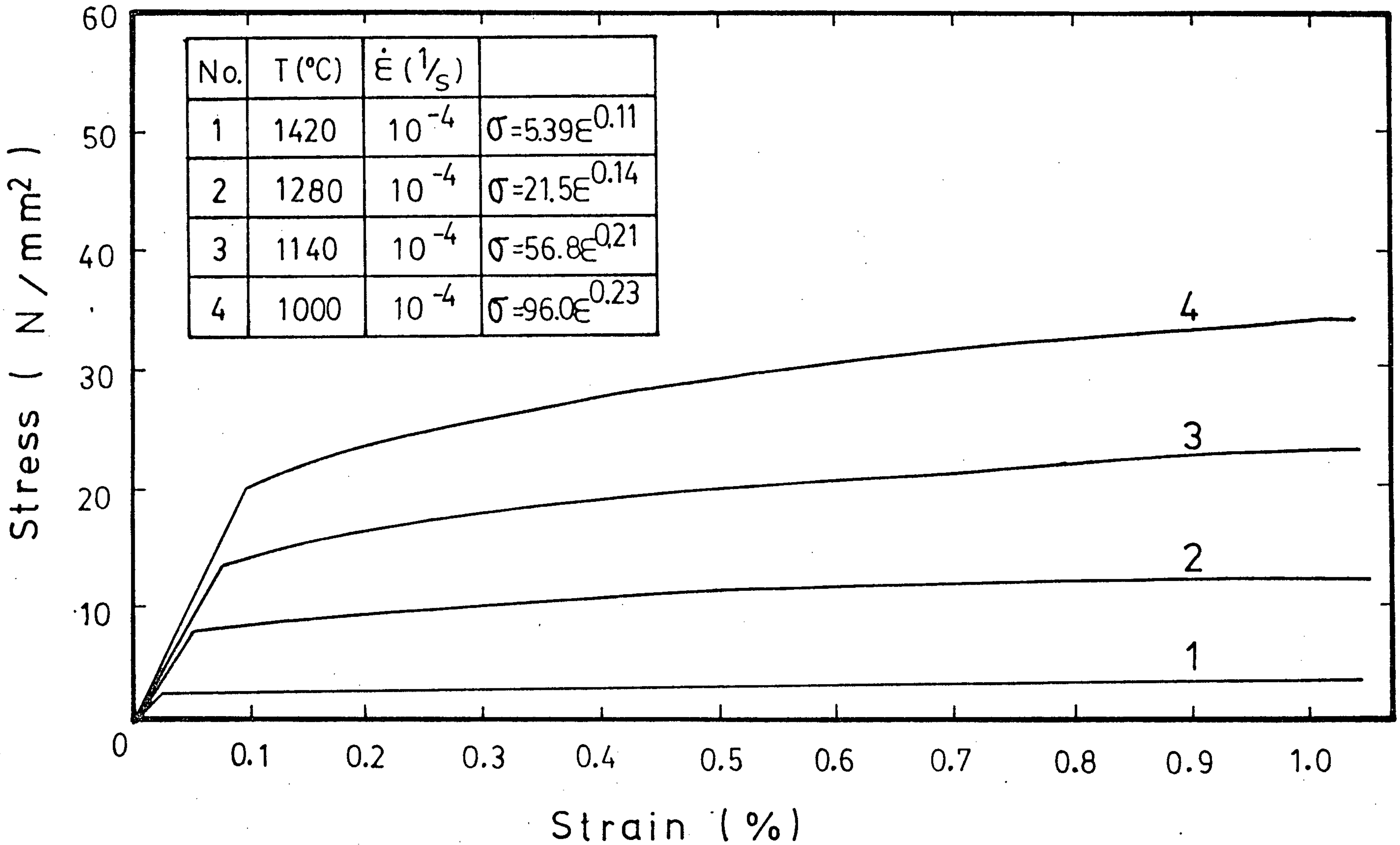

Fig. 4.5 Assumed Stress-Strain Curves for the Slab in Case 1.

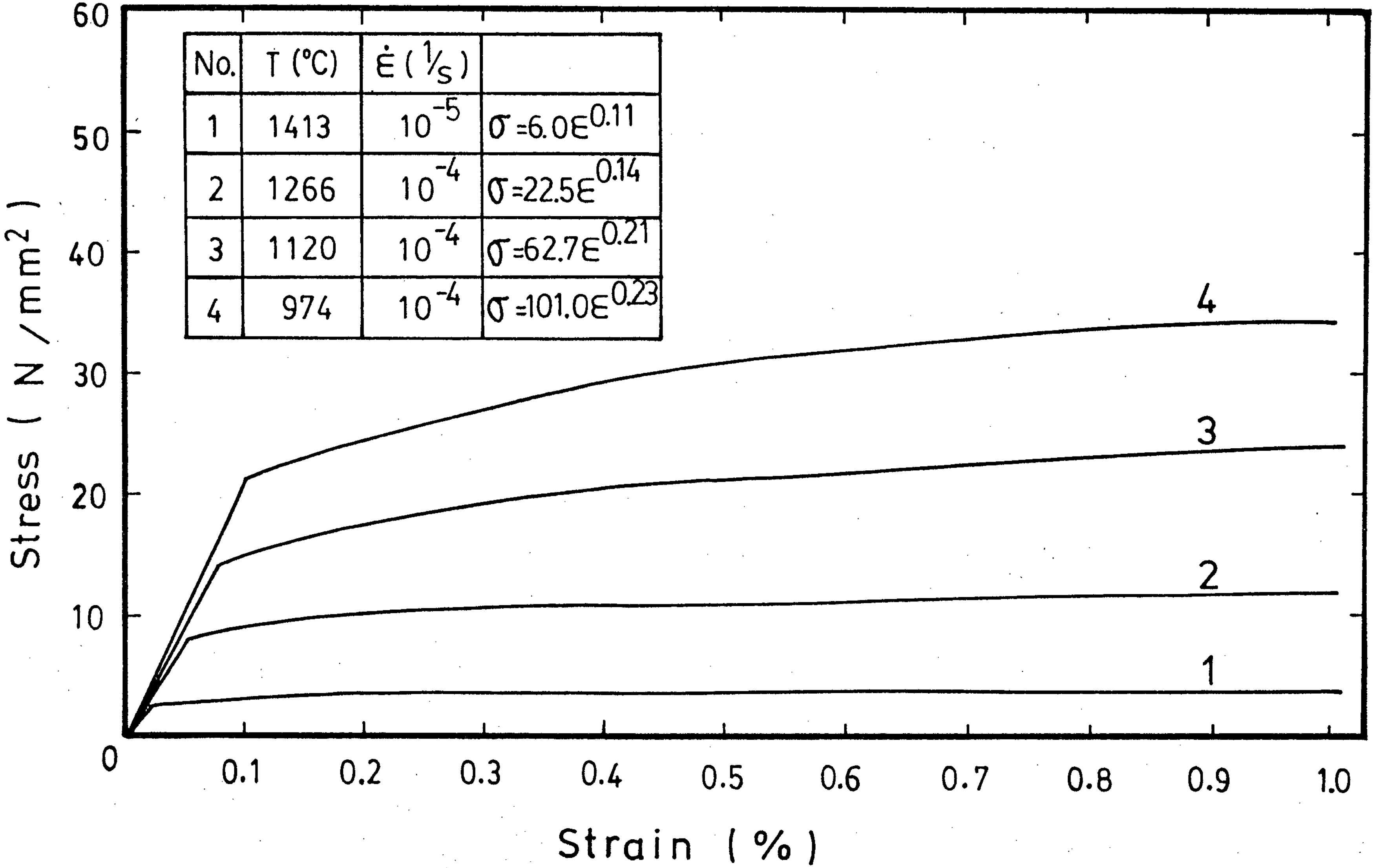

Fig. 4.6 Assumed Stress-Strain Curves for the Slab in Case 2,3,6,7,8,9 and 10.

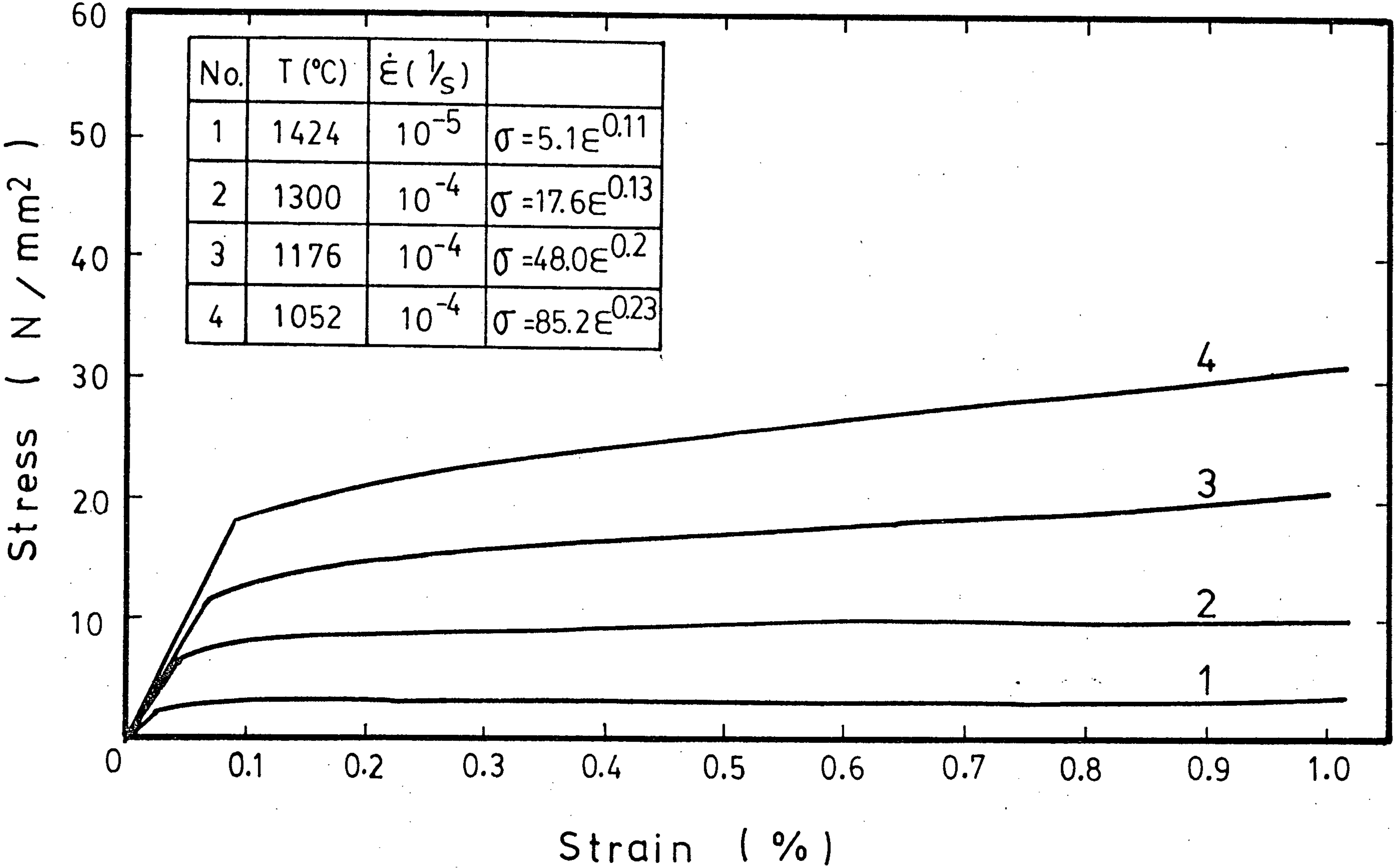

Fig. 4.7 Assumed Stress-Strain Curves for the Slab in Case 4.

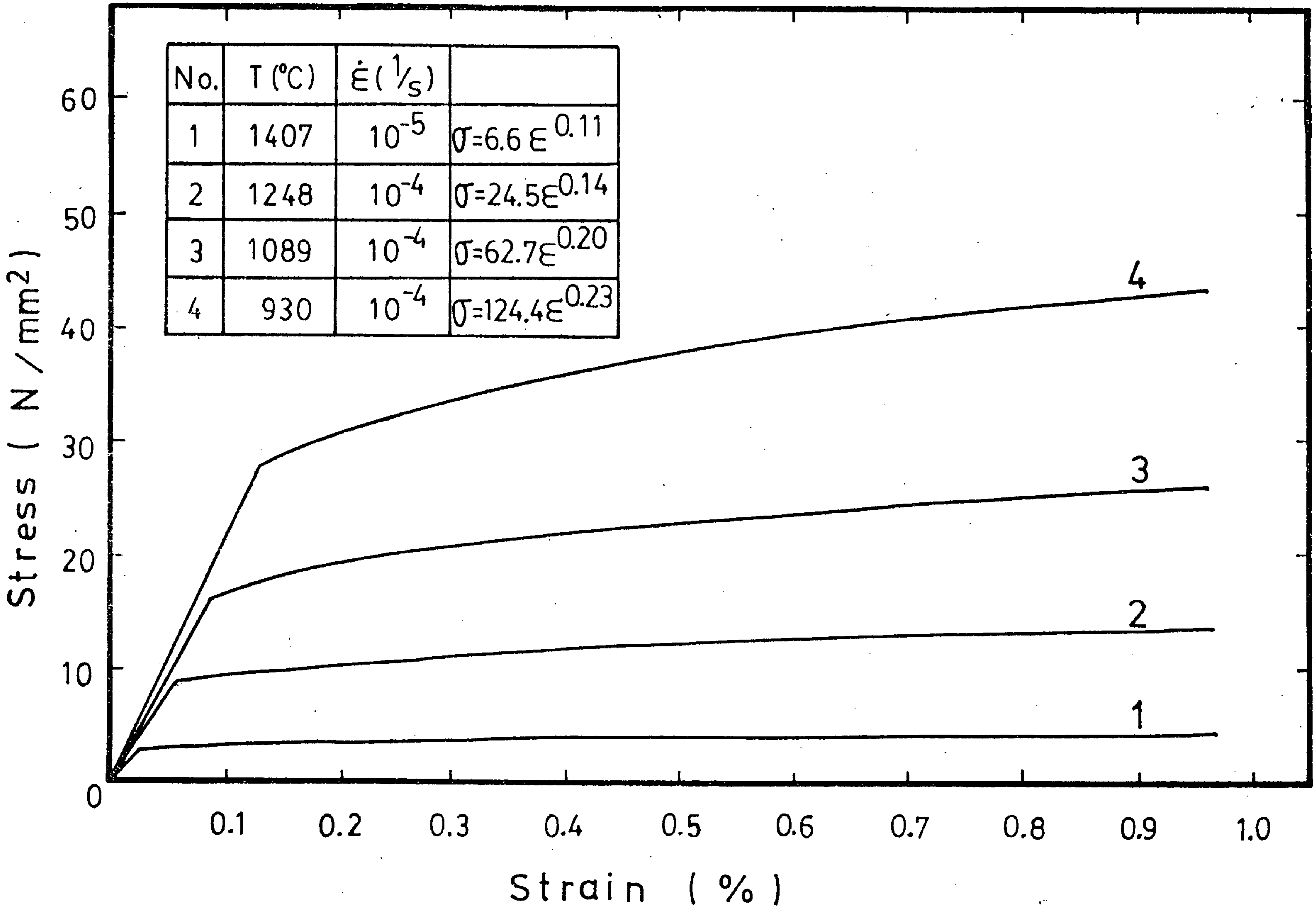

No.	T (°C)	$\dot{\varepsilon}$ (1/s)	
1	1407	10^{-5}	$\sigma = 6.6\,\varepsilon^{0.11}$
2	1248	10^{-4}	$\sigma = 24.5\varepsilon^{0.14}$
3	1089	10^{-4}	$\sigma = 62.7\varepsilon^{0.20}$
4	930	10^{-4}	$\sigma = 124.4\varepsilon^{0.23}$

Fig. 4.8 Assumed Stress-Strain Curves for the Slab in Case 5.

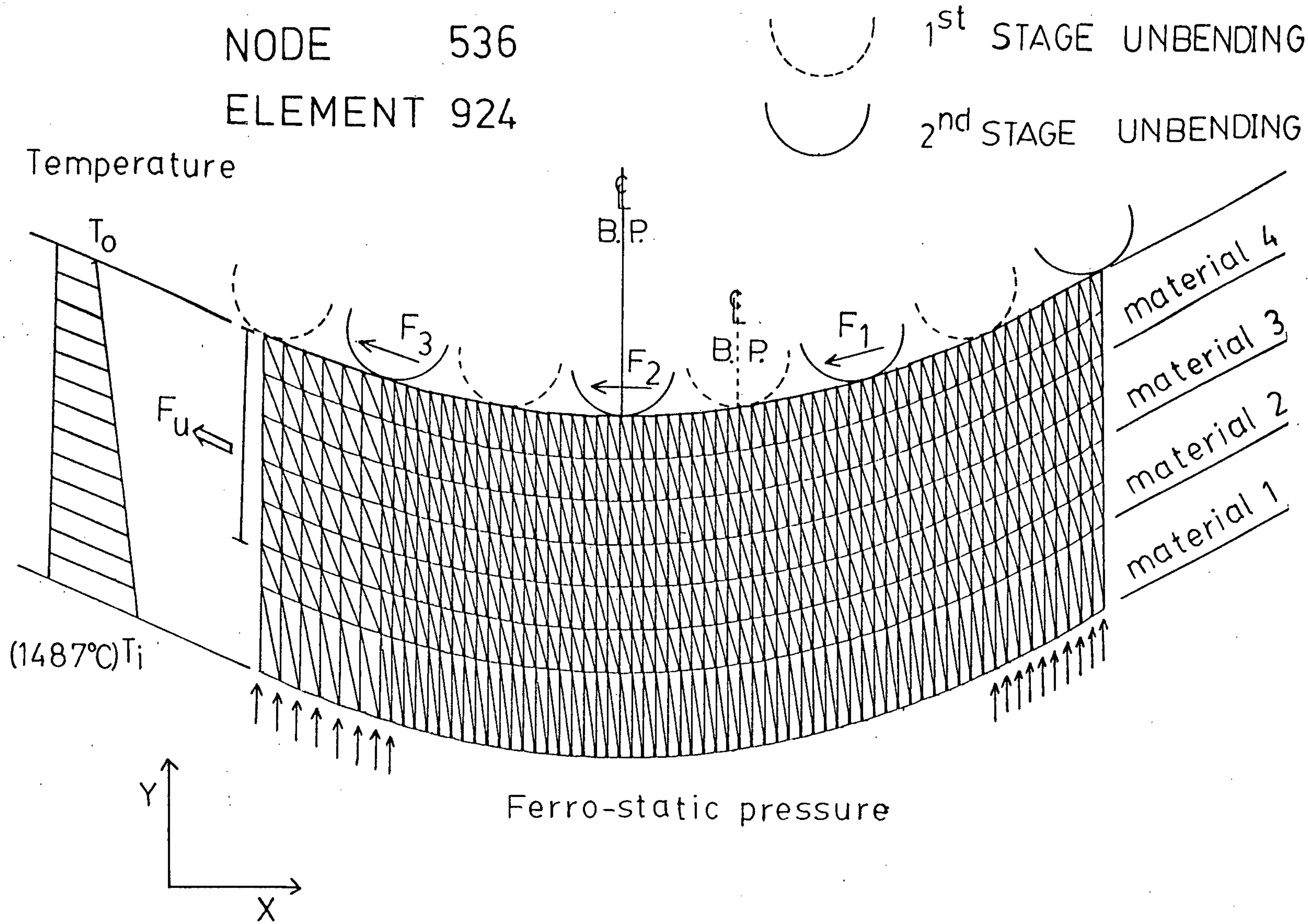

Fig. 4.9 Schematic Diagram of the Two-Dimensional Finite-Element Mesh for the Bending and Bulging Analysis.

Chapter 5

MODEL PREDICTIONS AND DISCUSSION

5.1 Results of calculations

Figs.5.1 to 5.6 show the results of bending and bulging analysis for Case 1,presented in terms of the computer plots of deformation, XX-strain contours, XY-strain contours, effective stress contours and principal strain vectors. As seen from Figs.5.5 and 5.6, the directions of principal strain vectors are the same as those of XX- and YY-strain. Thus, the ε_x component of strain is a principal strain and will be discussed hereafter with reference to internal cracks.

High peaks of tensile strain, ε_x (0.55 - 0.65%) occur at the inner surface of the upper shell beneath the roll support points in Fig.5.5, while at the inner surface of the lower shell the value of the peak strain, ε_x, is rather small (about 0.1%), as shown in Fig.5.6. This implies that internal cracks could be expected to appear preferentially on the upper shell in the straightening zone.

The deformation of the upper and lower shells is not

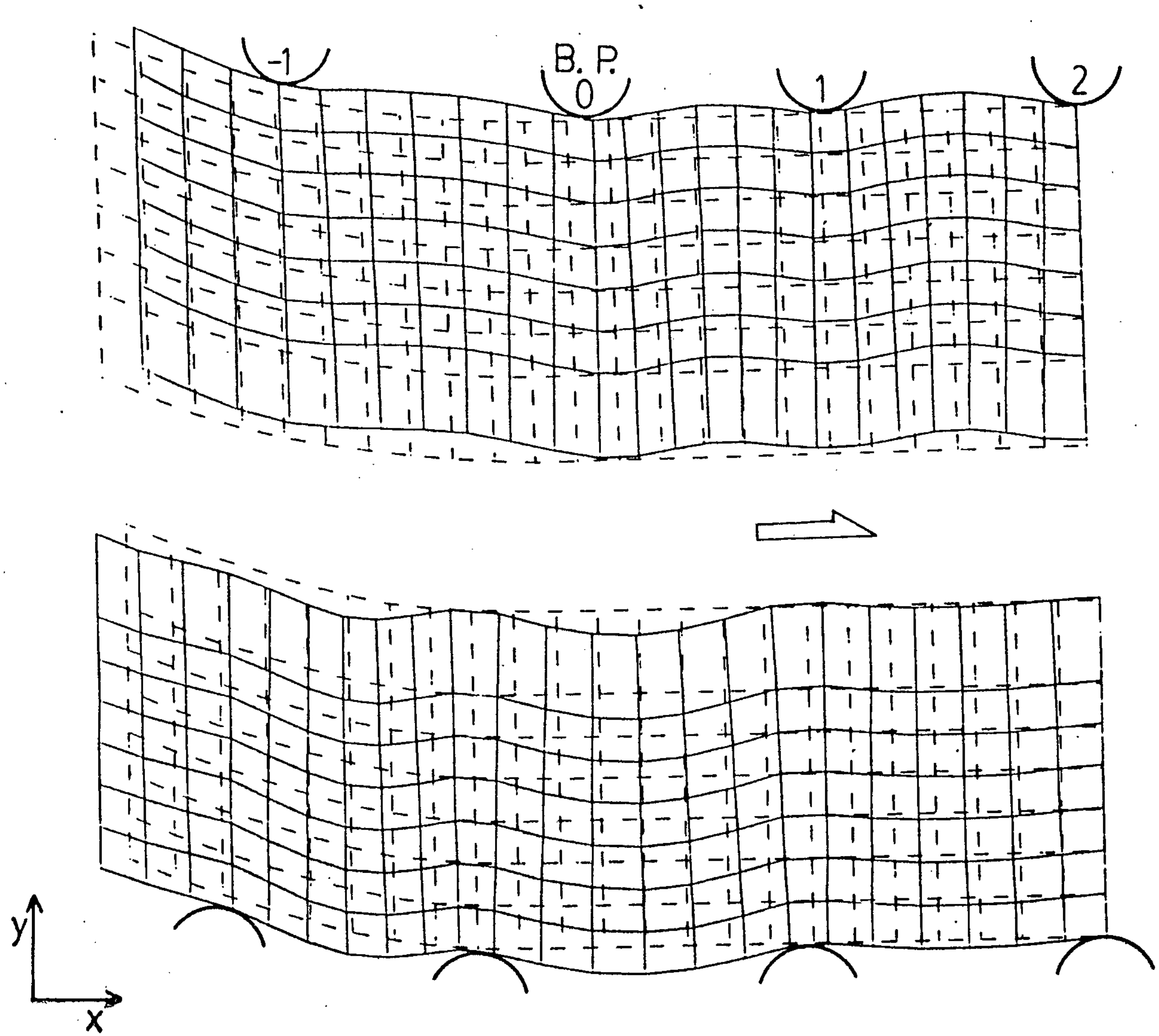

Fig. 5.1 Predicted Distortion Due to Bending and Bulging in Case 1.

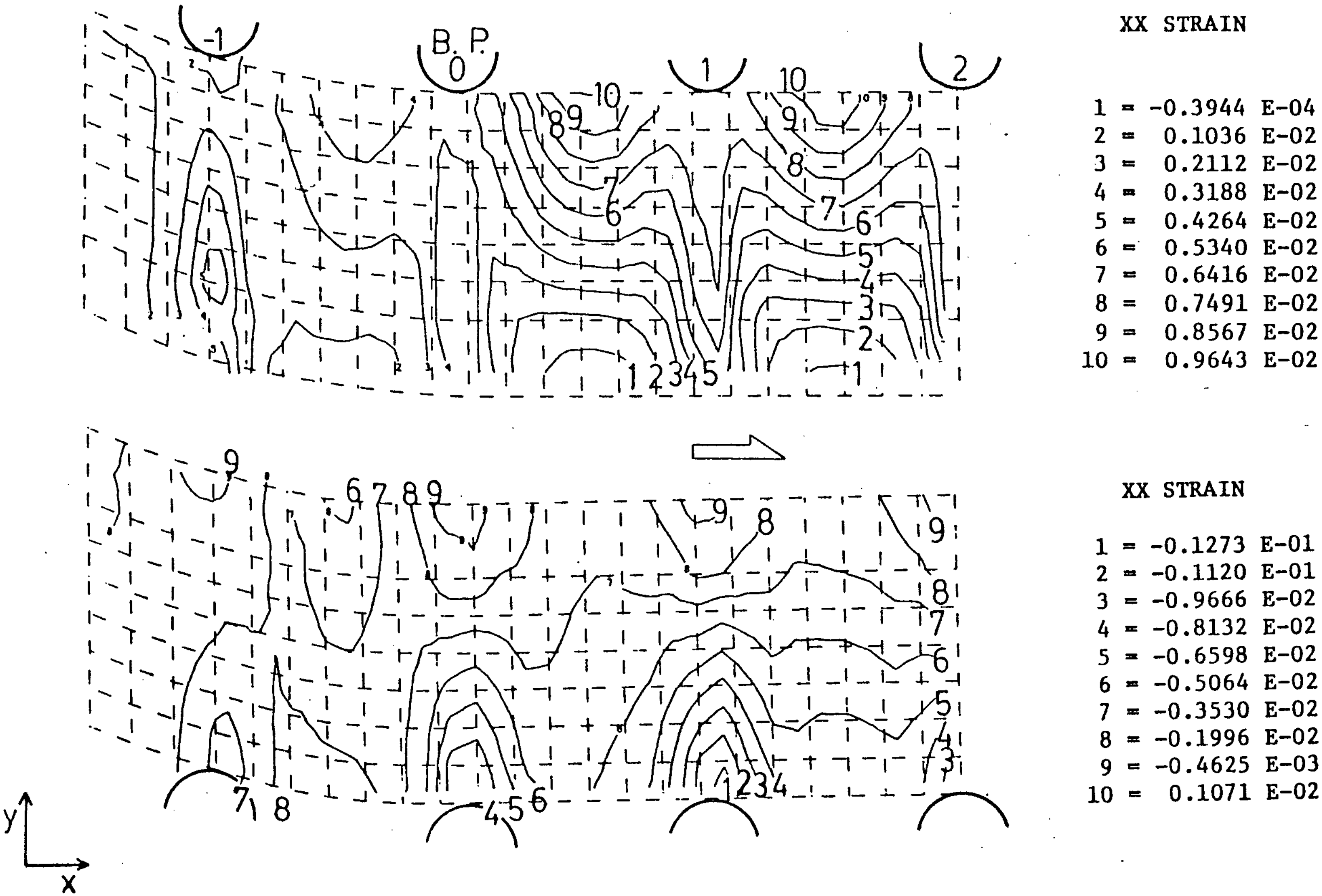

Fig. 5.2 Predicted XX-STRAIN Contours Due to Bending and Bulging in Case 1.

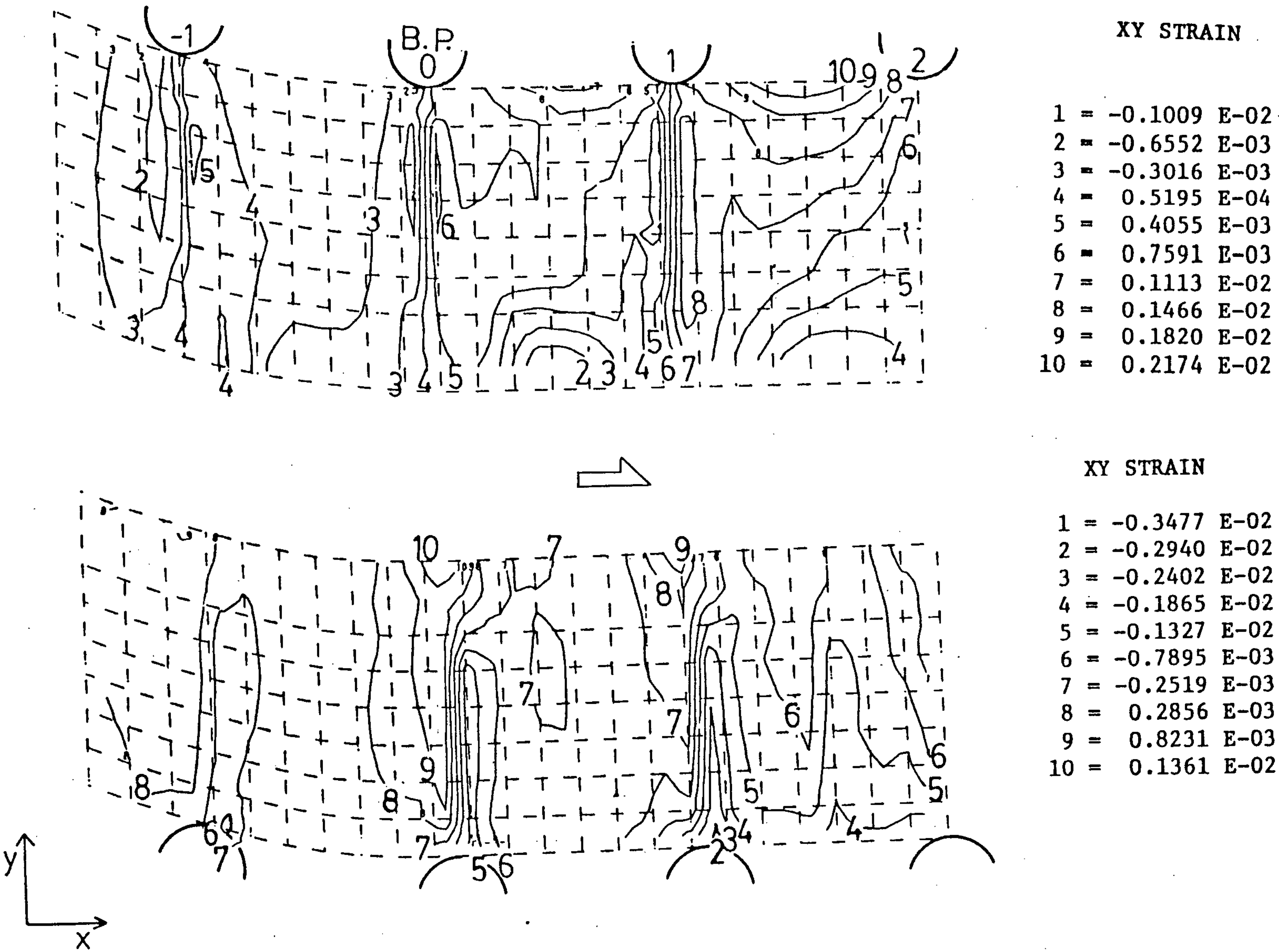

Fig. 5.3 Predicted XY-STRAIN Contours Due to Bending and Bulging in Case 1.

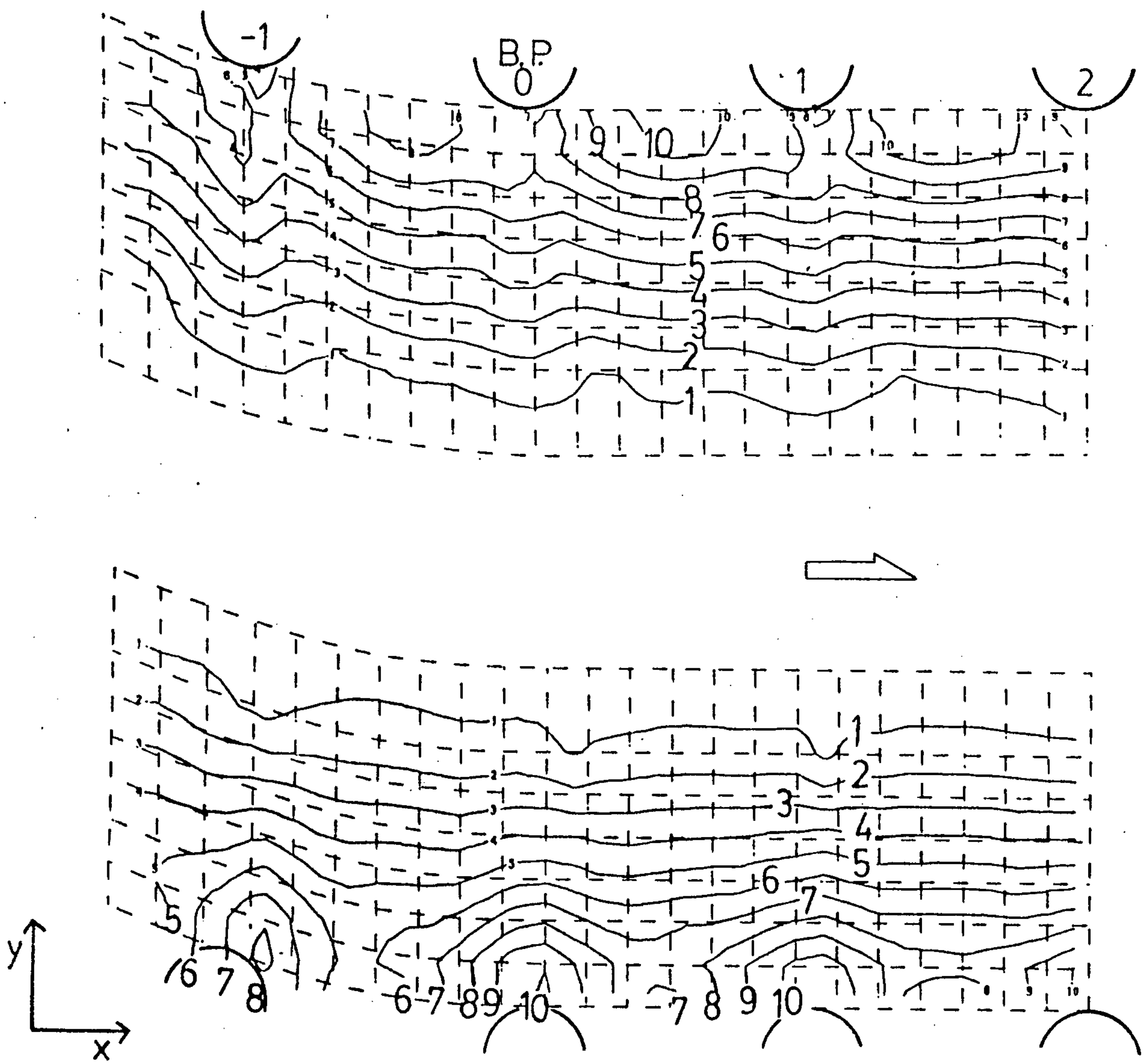

EFFECTIVE STRESS (MPa)

1 = 0.4806 E+01
2 = 0.7817 E+01
3 = 0.1082 E+02
4 = 0.1383 E+02
5 = 0.1684 E+02
6 = 0.1986 E+02
7 = 0.2287 E+02
8 = 0.2588 E+02
9 = 0.2889 E+02
10 = 0.3190 E+02

EFFECTIVE STRESS (MPa)

1 = 0.5478 E+01
2 = 0.8607 E+01
3 = 0.1174 E+02
4 = 0.1486 E+02
5 = 0.1799 E+02
6 = 0.2111 E+02
7 = 0.2425 E+02
8 = 0.2738 E+02
9 = 0.3050 E+02
10 = 0.3364 E+02

Fig. 5.4 Predicted EFFECTIVE STRESS Contours Due to Bending and Bulging in Case 1.

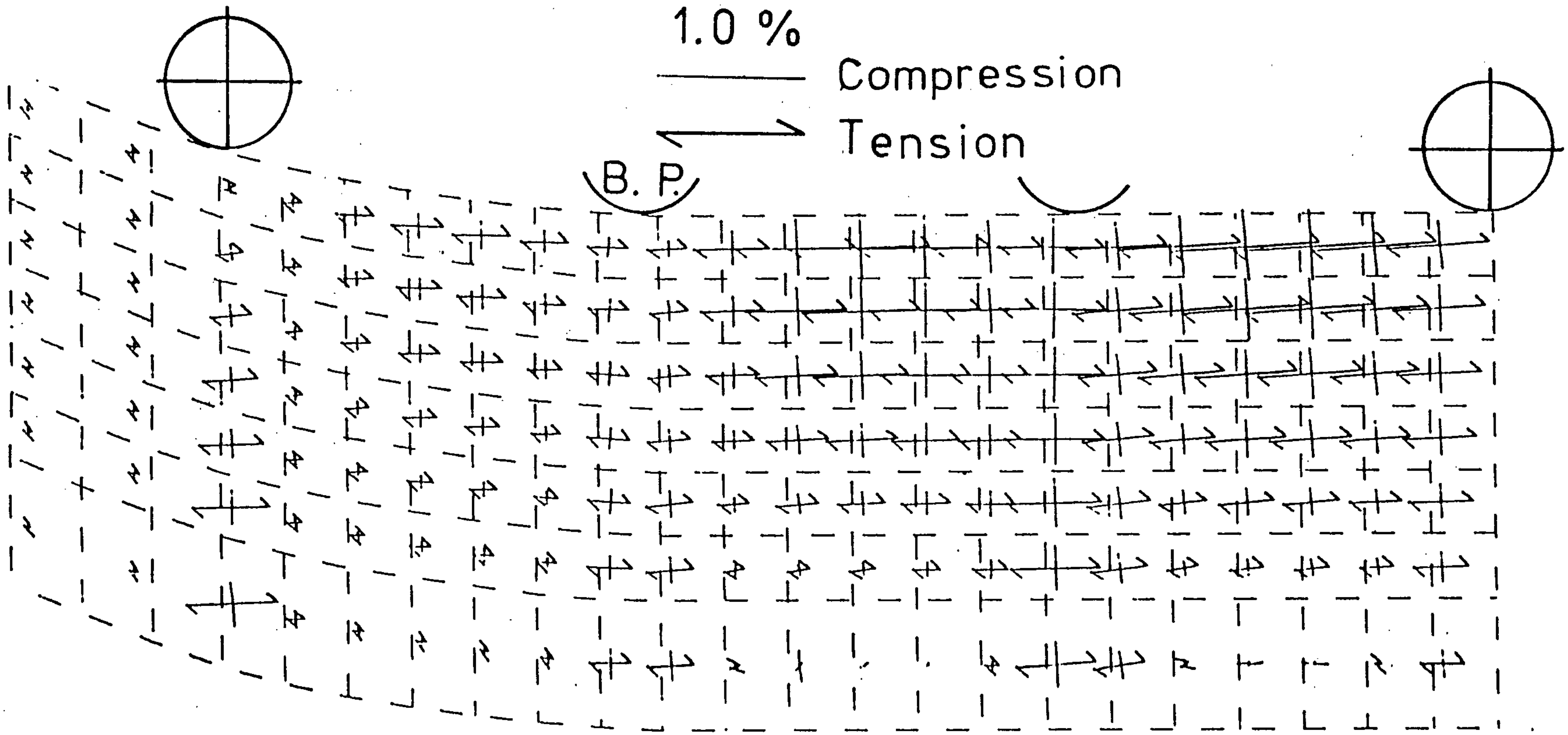

Fig. 5.5 Predicted Principal Strain Vectors Due to Bending and Bulging in Case 1.(Upper Shell)

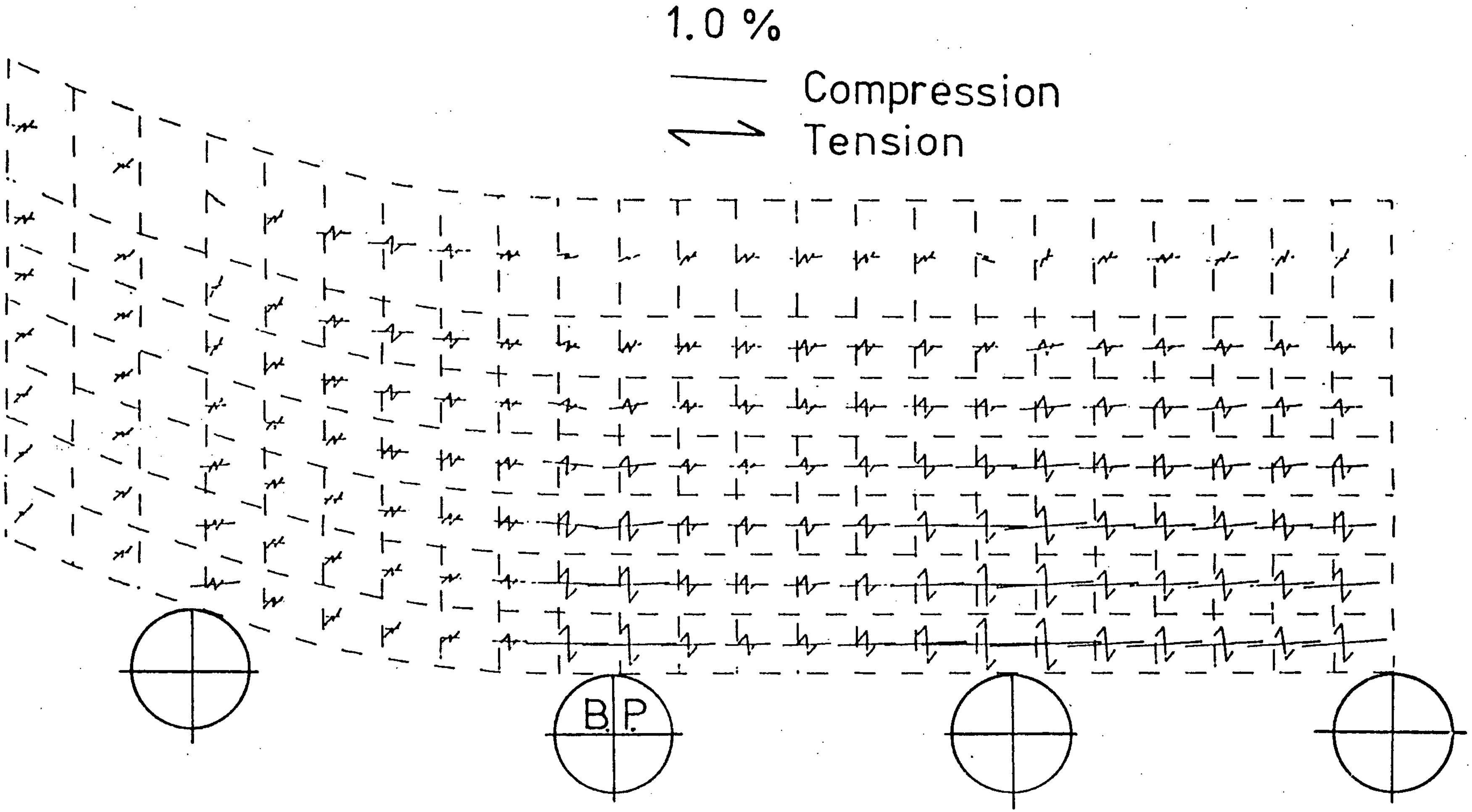

Fig.5.6 Predicted Principal Strain Vectors Due to Bending and Bulging in Case 1.(Lower Shell)

Table IV Strains at solidification front on the center plane normal to the wide face.

	Bulging	Bending		Bending and Bulging					
		inner surface	outer surface						
	ε_x %	ε_x %	ε_x %	ε_x %	ε_y %	ε_z %	ε_{xy} %	$\bar{\sigma}$ MPa	$\bar{\varepsilon}_p$ %
CASE 1. U	0.08	0.17	0.84	0.55/0.65	-0.26/-0.28	-0.27/-0.33	0.043/0.16	3.1/3.4	0.5/0.67
L	0.08	-0.21	-0.82	0.1	-0.0075	-0.085	0.09	3.8	0.56
2. U	0.062	0.1	0.85	0.25/0.3 *	-0.13/-0.18	-0.12/-0.11	0.043/0.06	3.2/3.7	0.23/0.29
3. U	0.045	0	0.84	0.15/0.2	-0.078/-0.12	-0.08/-0.1	0.033/0.016	3.2/3.3	0.14/0.2
L	0.045	-0.02	-0.85	0.1/0.13	-0.037/-0.09	-0.086/-0.04	0.065/0.055	3.5/3.1	0.28/0.16
4. U	0.072	0.15	0.91	0.38/0.4	-0.19/-0.15	-0.13/-0.17	0.0058/0.093	2.8/2.9	0.3/0.32
5. U	0.055	0.03	0.79	0.15/0.23	-0.077/-0.15	-0.076/-0.09	0.011/-0.001	2.4/4.0	0.14/0.34
6. U	0.034	0.09	0.84	0.15/0.20	-0.06/-0.12	-0.08/-0.09	0/0.012	3.5/3.3	0.17/0.18
7. U	0.089	0.1	0.87	0.3/0.4	-0.11/-0.25	-0.12/-0.17	0.055/0.058	3.4/3.6	0.27/0.42
8. U	0.039	0.09	1.1	0.15/0.2	-0.086/-0.098	-0.077/-0.10	0.0075/0.004	2.9/3.6	0.22/0.17
9. U	0.063	0.19	1.05	0.35/0.4	-0.19/-0.15	-0.17/-0.084	0.007/-0.04	3.3/3.6	0.33/0.27
10. U	0.082	0.11	0.73	0.3/0.33	-0.11/-0.16	-0.13/-0.12	0.056/0.0057	3.2/3.5	0.24/0.26

U : upper shell , L : lower shell

* critical strain for internal cracks

symmetrical, as shown in Fig.5.1. Maximum bulging deflection of the upper shell is usually larger than that of the lower shell, for example the maximum bulging of the upper and lower shells is 0.87 mm and 0.39 mm respectively between No.1 and No.2 rolls.

As seen from the ε_x contours, Fig.5.2, the spacing of each contour is uniform through the shell thickness, indicating that the longitudinal strain distribution ε_x is linear through the shell thickness. Thus, the behavior of each shell is similar to that of a simple beam rather than of a two-dimensional continuum. The shear strain ε_{xy} is fairly small, close to one fourth of the ε_x component, see Fig.5.3.

Table IV lists all the components of strain at the solidification front for the other cases. The remaining results of Case 2 to Case 10 are presented in Appendix VI.

5.1.1 Comparison of model prediction with plant data

Fig.5.7 shows the relation between internal cracks and casting speed at Oita NO.4 caster, NSC.[34,35] Here, the rating of internal cracks is defined as crack length divided by crack spacing. Thus the threshold casting speed for bending related internal cracks is seen to be 1.1 - 1.2 m/min for the case of ordinary casting i.e. without compression. Figs.5.8 to 5.10[46] show examples of sulfur prints of a longitudinal section through slabs with internal crack ratings of 0.2,0.5 and 1.0

respectively. The internal cracks generally appear as dark segregation lines between the primary arms of dendrites. As is apparent from these prints, internal cracks tend to appear on the upper shell with an increase in casting speed.

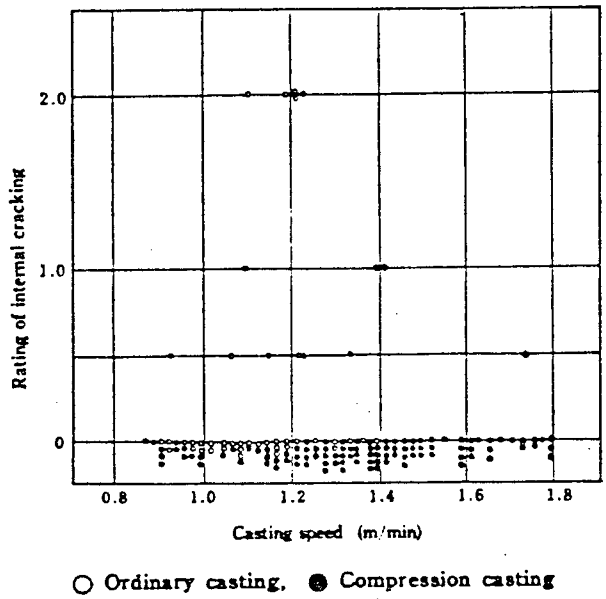

Fig.5.7 Relation between Internal Cracks and Casting Speed at Oita NO.4 caster.
(Al-Si-killed ($40kg/mm^2$) steel grade)[34,35]

Figs.5.11 to 5.15 show the model predictions for casting speeds of 1.6,1.2 and 1.0 m/min. The level of strain ε_x at the inner surface of the upper shell increases with an increase in casting speed, while ε_x at the inner surface of the lower shell remains low. Thus the critical strain for internal cracks,which is reached at a casting speed of 1.2m/min, is 0.25 to 0.30% according to the present analysis. This value of critical strain is resonable in comparison to the experimental values reported in the literature (refer to Section

2.1).[12,15,36-39]

5.1.2 Bulging strain

Figs.5.16 to 5.18 show the results of the bulging analysis of Case 1(lower shell). From Fig.5.17, the peak tensile strain, ε_x, appears periodically along the inner surface of the shell. The magnitude of the shear strain, ε_{xy} is about one half of the ε_x component in the present case and hence is fairly important in the bulging analysis. A similar finding has been reported by Matsumiya.[25]

Table V shows the maximum bulging deflection between No.1 and No.2 rolls for the cases of bulging alone and bulging in combination with bending. The total deflection due to the combination of bending and bulging is usually larger than that due to bulging by itself.

5.1.3 Bending/Unbending strain

Figs.5.19 and 5.20 show the results of calculations of the bending strain, ε_x, for Case 1. The remaining results are presented in Appendix VI. The major characteristics of the results are as follows. The bending strain, ε_x, is observed to increase from one roll before the bending point to Roll No.1 beyond which it reaches a steady-state level. The upper and lower shells deform about their own neutral axes the

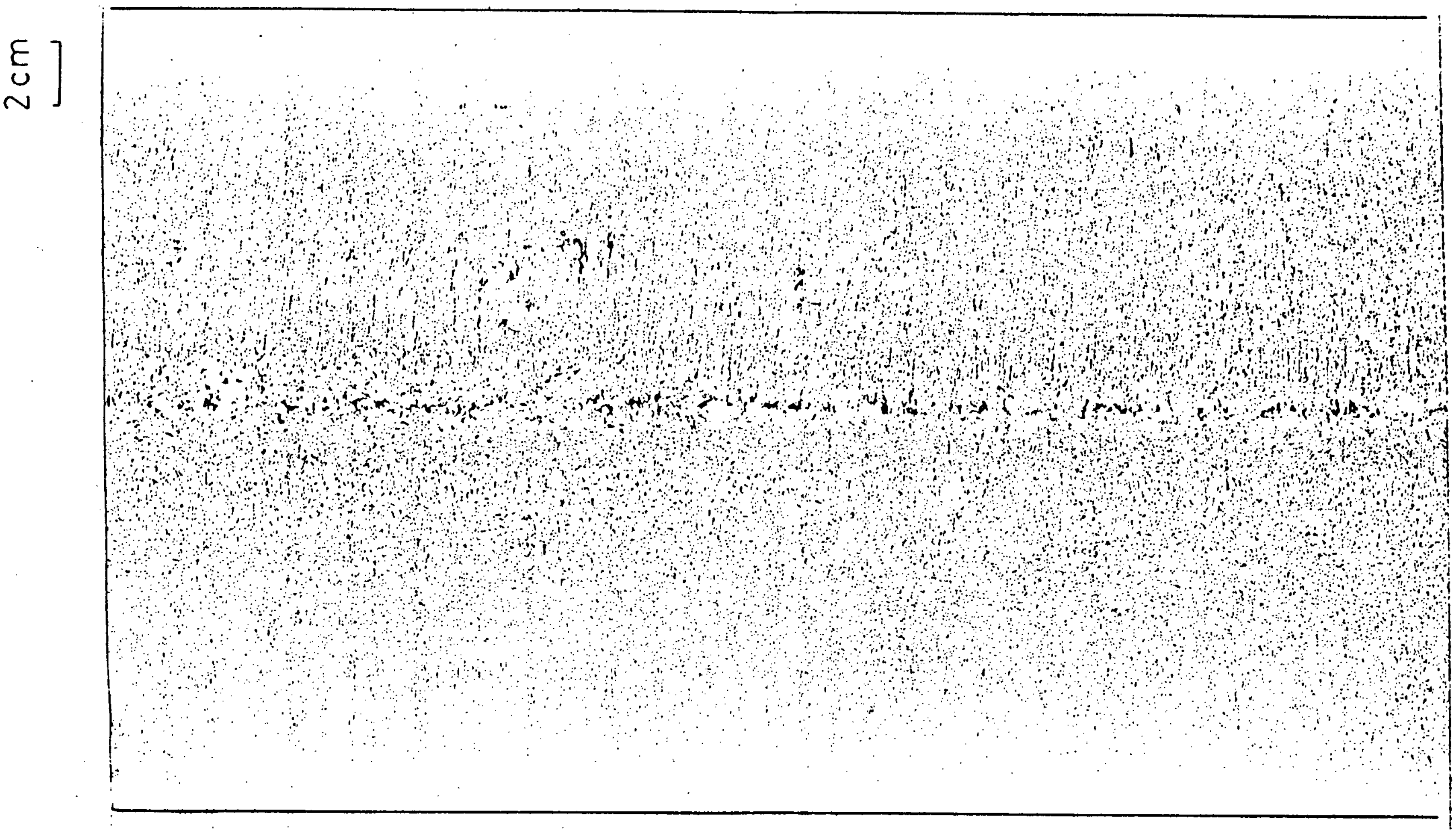

Fig. 5.8 Sulfur Print of a Longitudinal Section ; Rating of Internal Cracks = 0.2.[46]

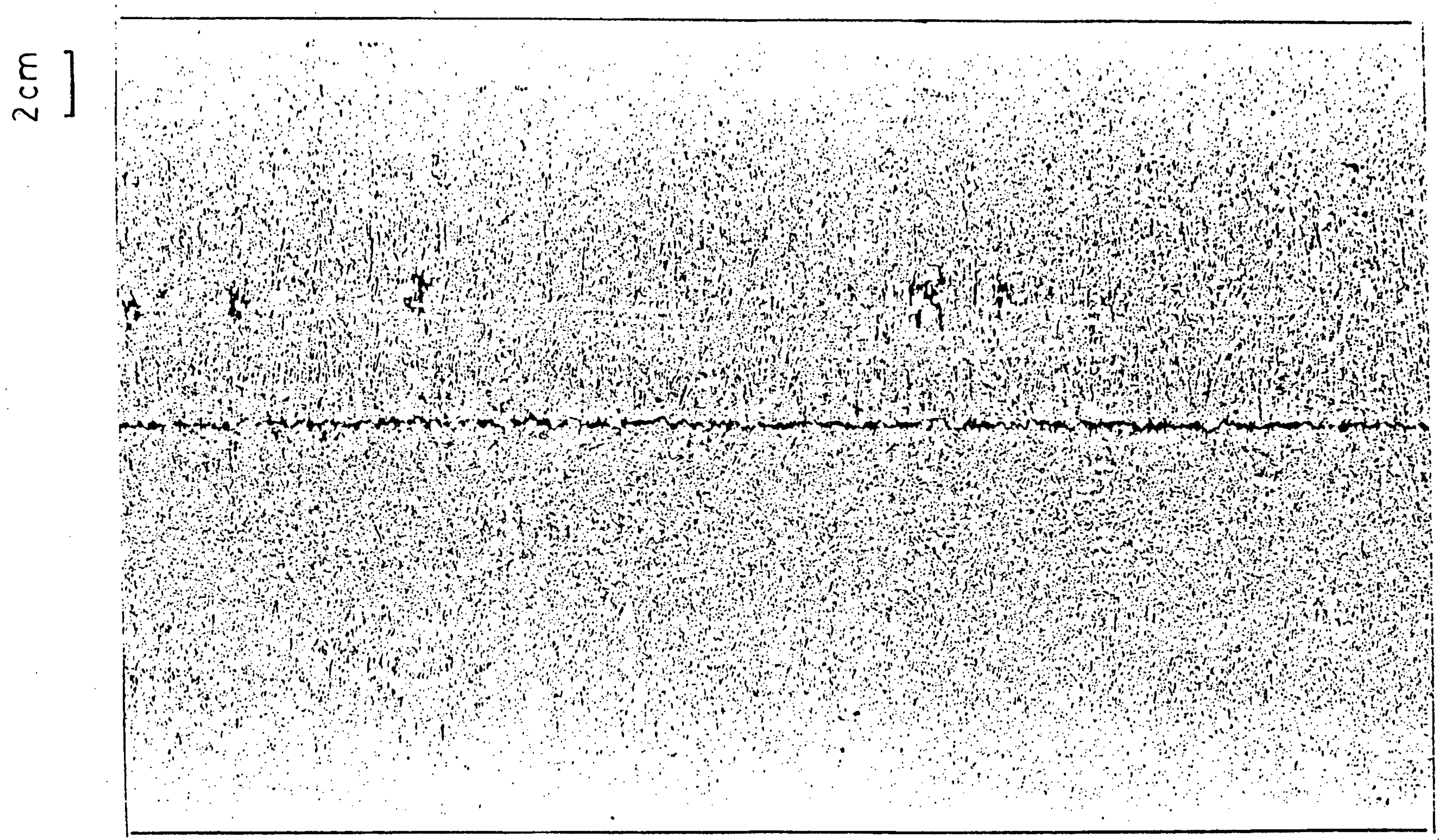

Fig. 5.9 Sulfur Print of a Longitudinal Section ; Rating of Internal Cracks = 0.5.[46]

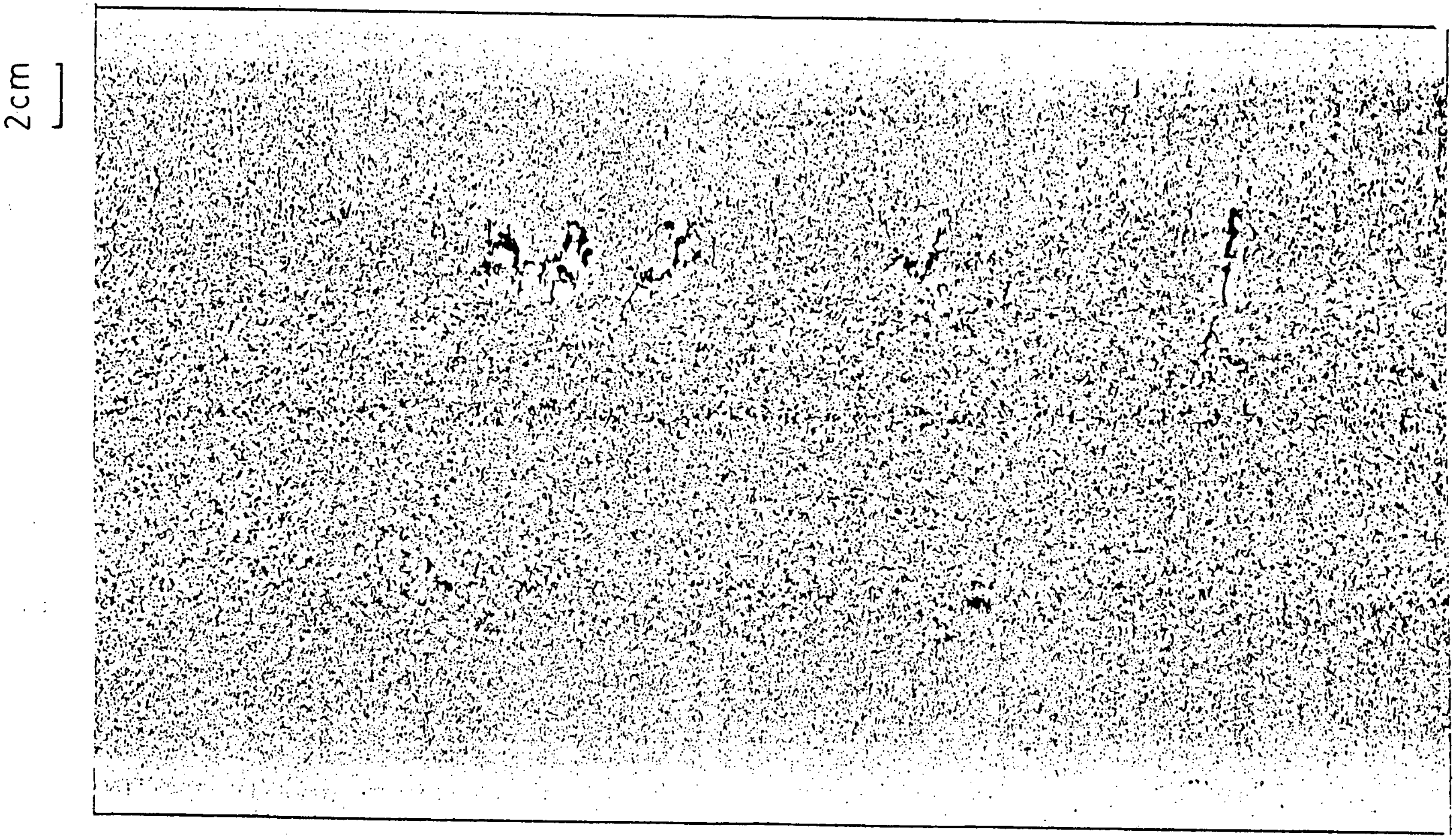

Fig. 5.10 Sulfur Print of a Longitudinal Section ; Rating of Internal Cracks = 1.0.[46]

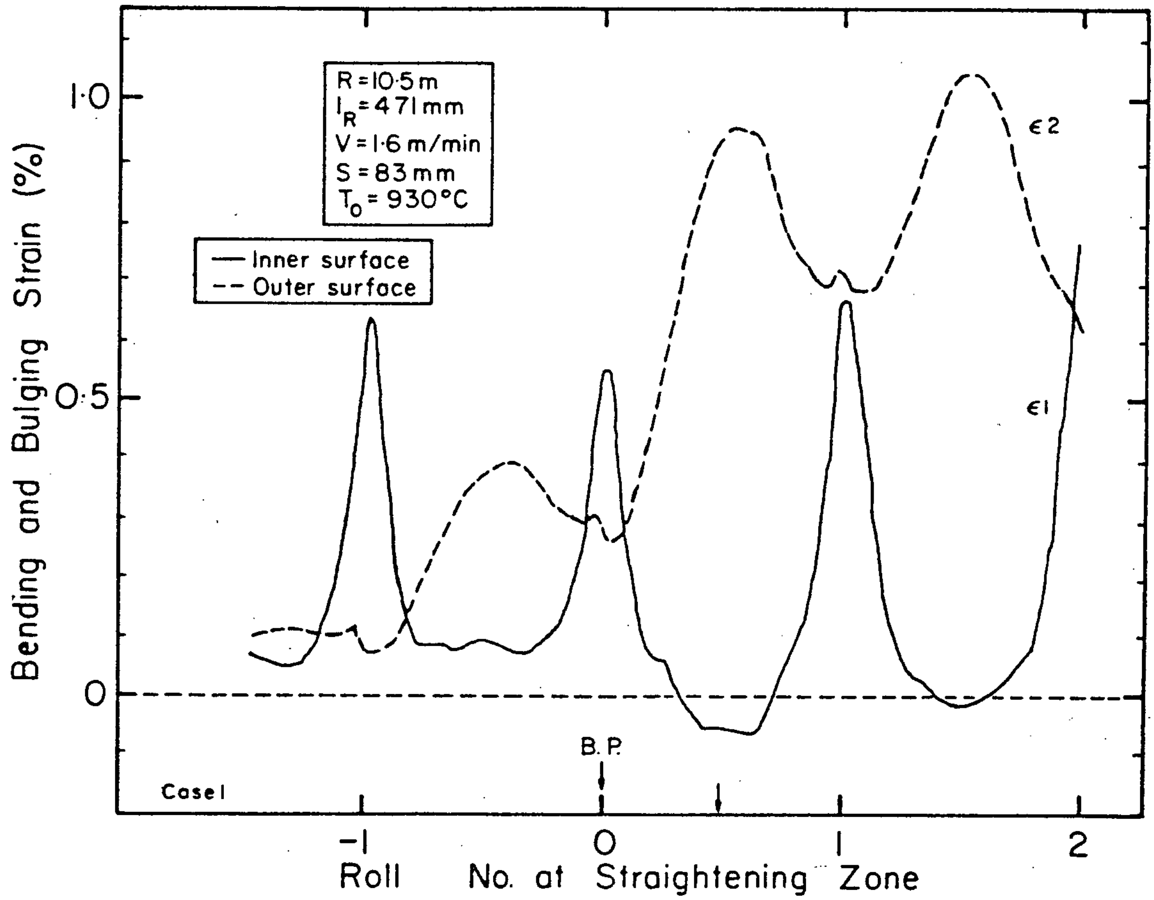

Fig. 5.11 Predicted Bending and Bulging Strain, ε_x in Case 1. (Upper Shell, V=1.6m/min)

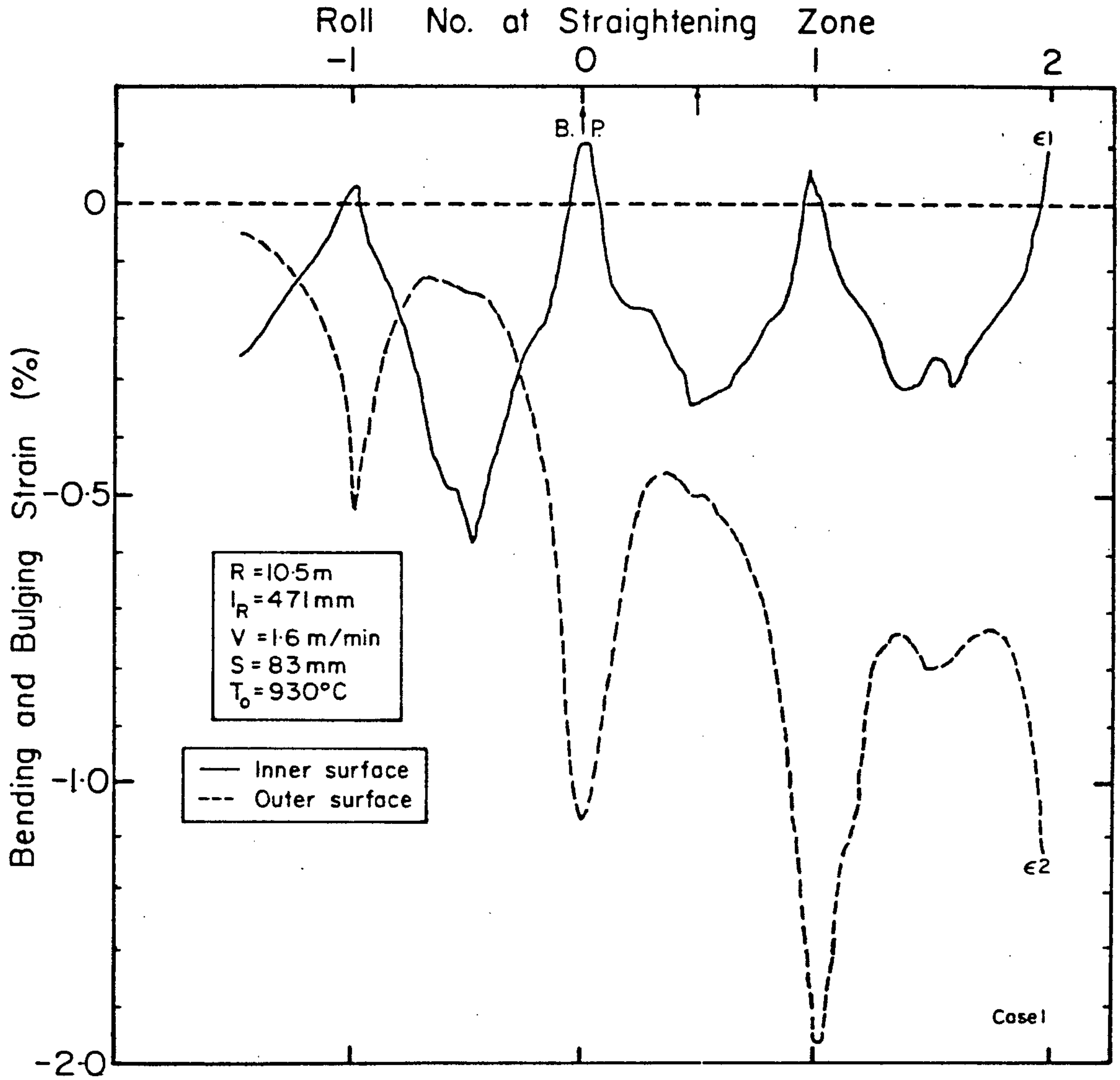

Fig. 5.12 Predicted Bending and Bulging Strain, ε_x in Case 1. (Lower Shell, V=1.6m/min)

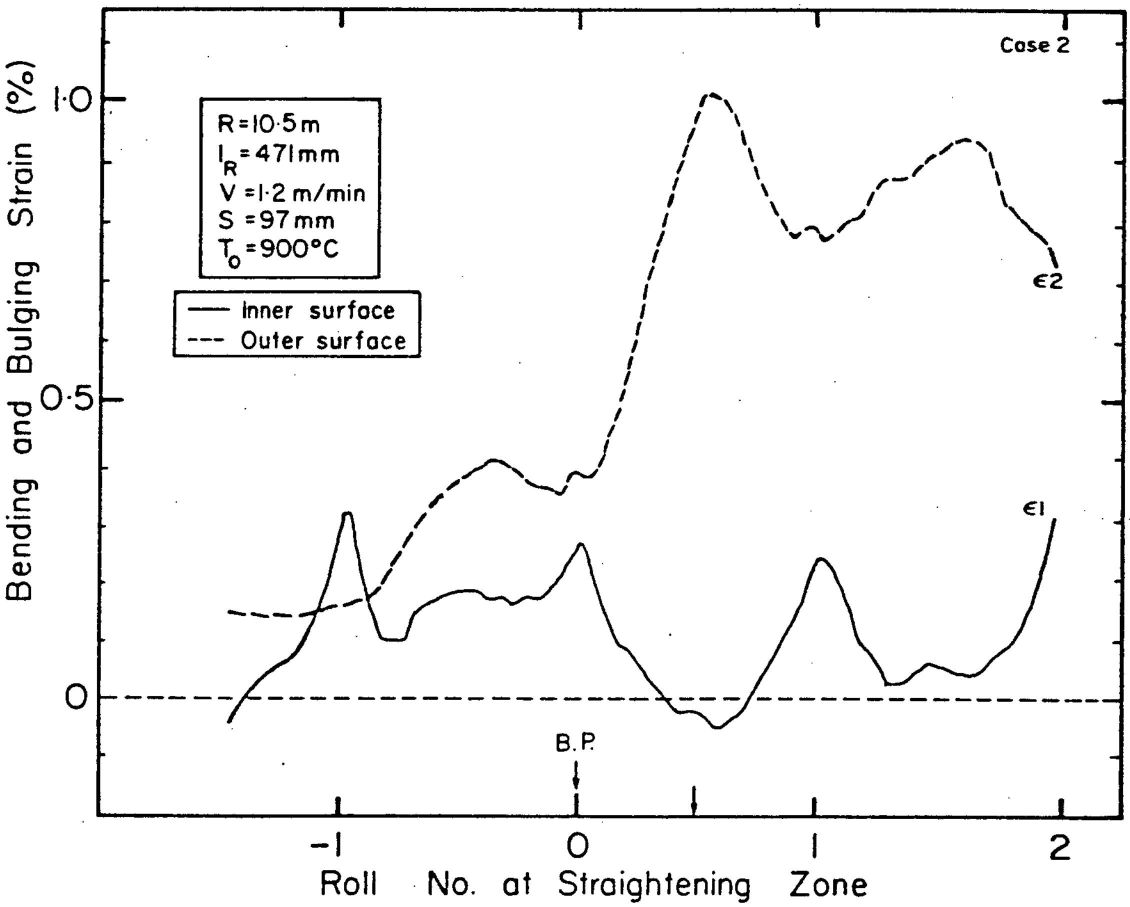

Fig. 5.13 Predicted Bending and Bulging Strain, ε_x in Case 2. (Upper Shell, V=1.2m/min)

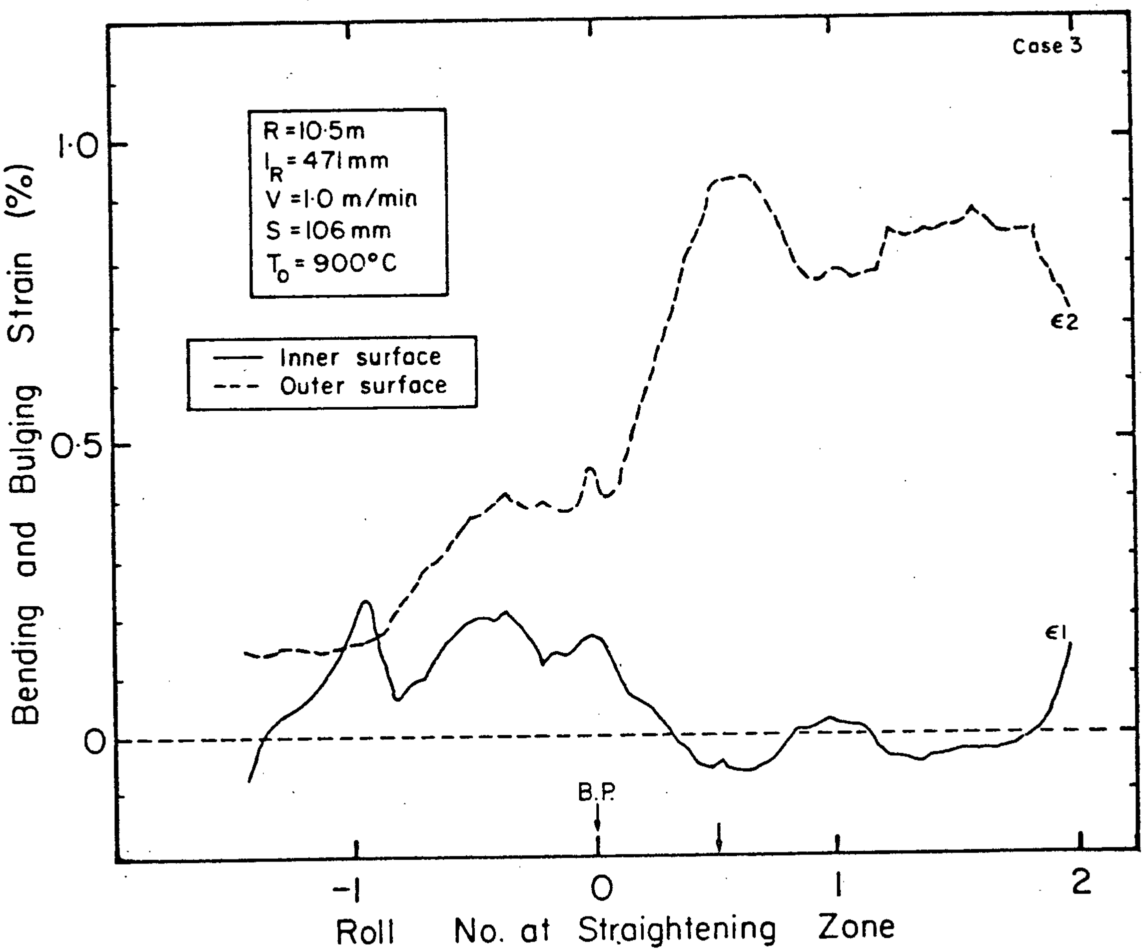

Fig. 5.14 Predicted Bending and Bulging Strain, ε_x in Case 3. (Upper Shell, V=1.0m/min)

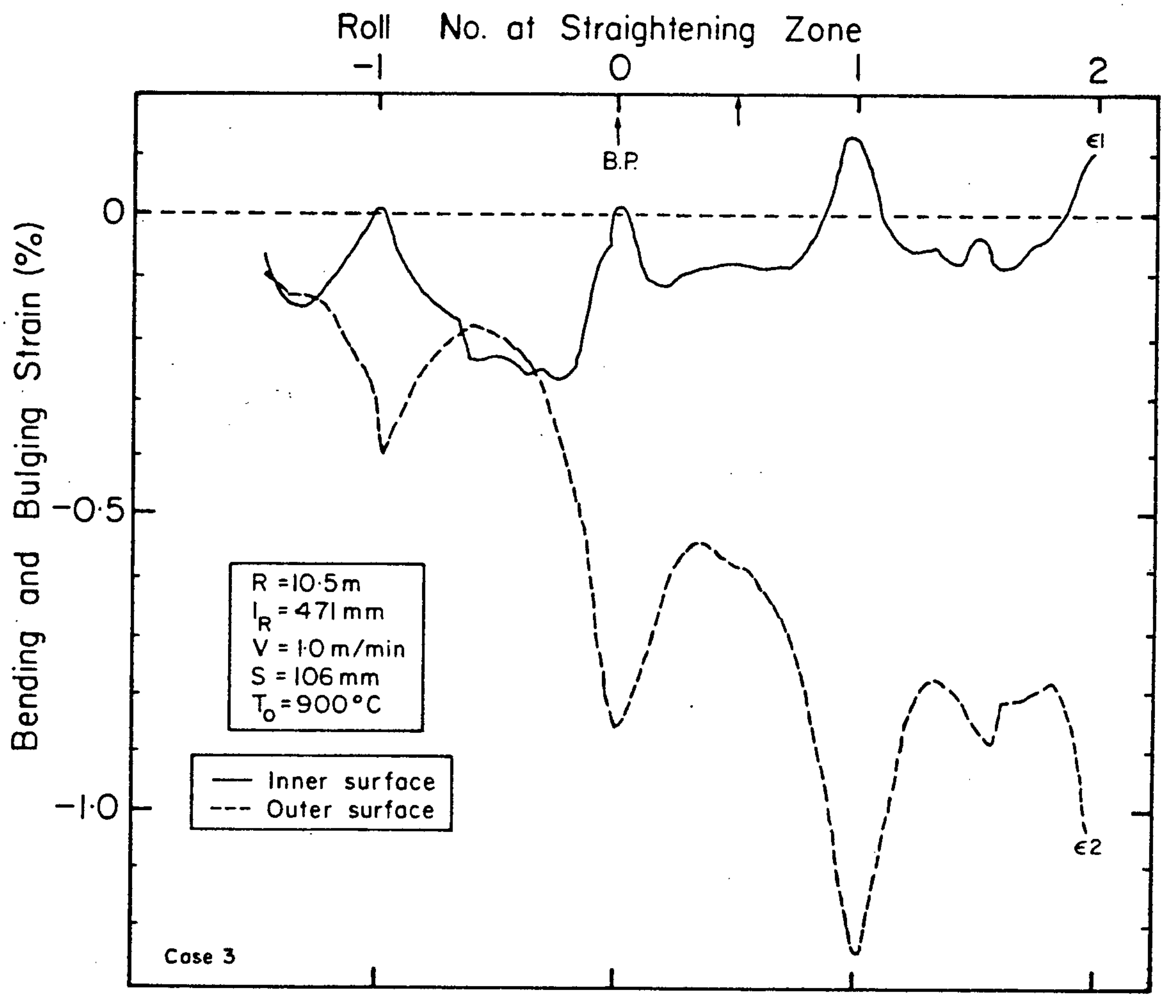

Fig. 5.15 Predicted Bending and Bulging Strain, ε_x in Case 3. (Lower Shell, V=1.0m/min)

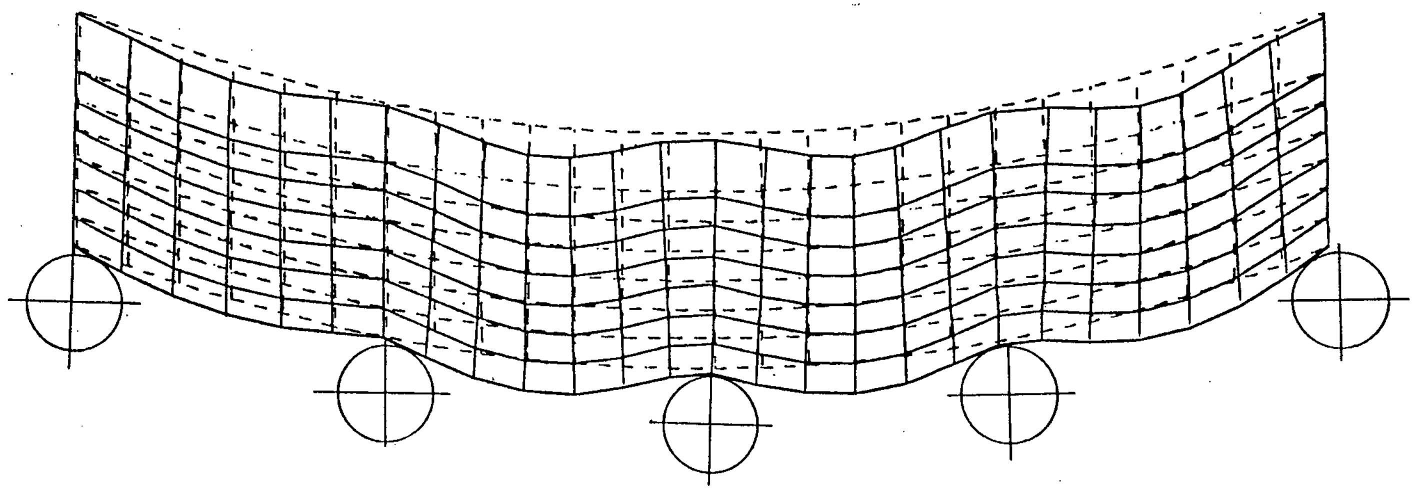

Fig. 5.16 Predicted Distortion Due to Bulging in Case 1. (Lower Shell)

XX-STRAIN

1	=	-0.4257E-03
2	=	-0.2556E-03
3	=	-0.8544E-04
4	=	0.8471E-04
5	=	0.2549E-03
6	=	0.4250E-03
7	=	0.5952E-03
8	=	0.7653E-03
9	=	0.9355E-03
10	=	0.1106E-02

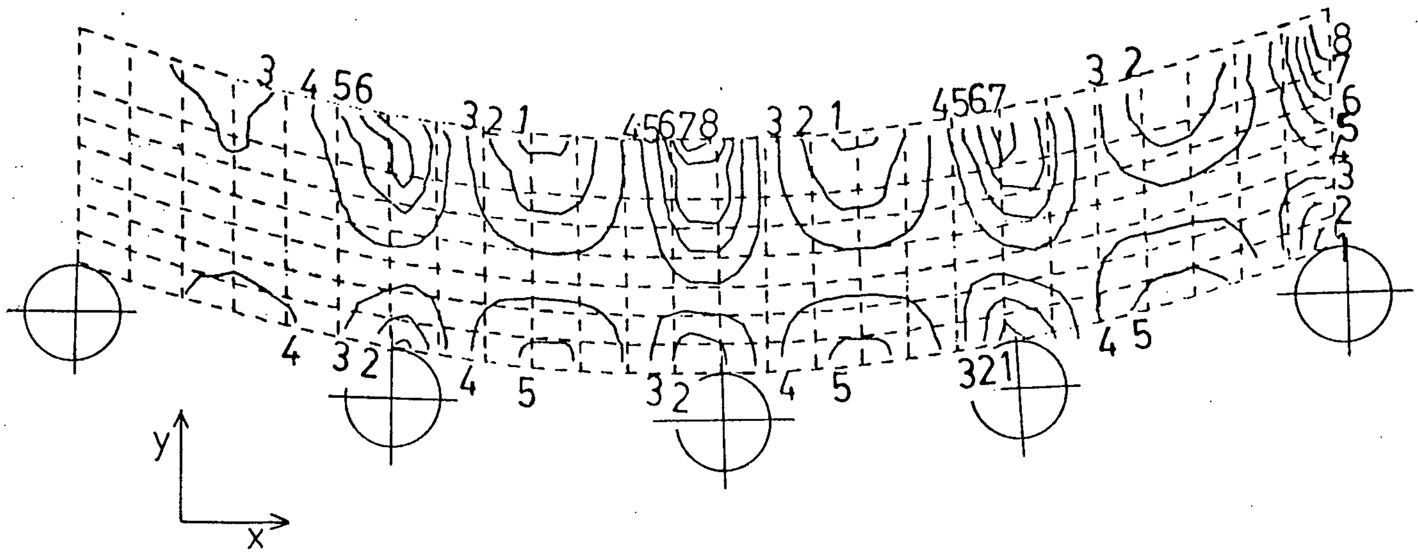

Fig. 5.17 Predicted XX-STRAIN Due to Bulging in Case 1. (Lower Shell)

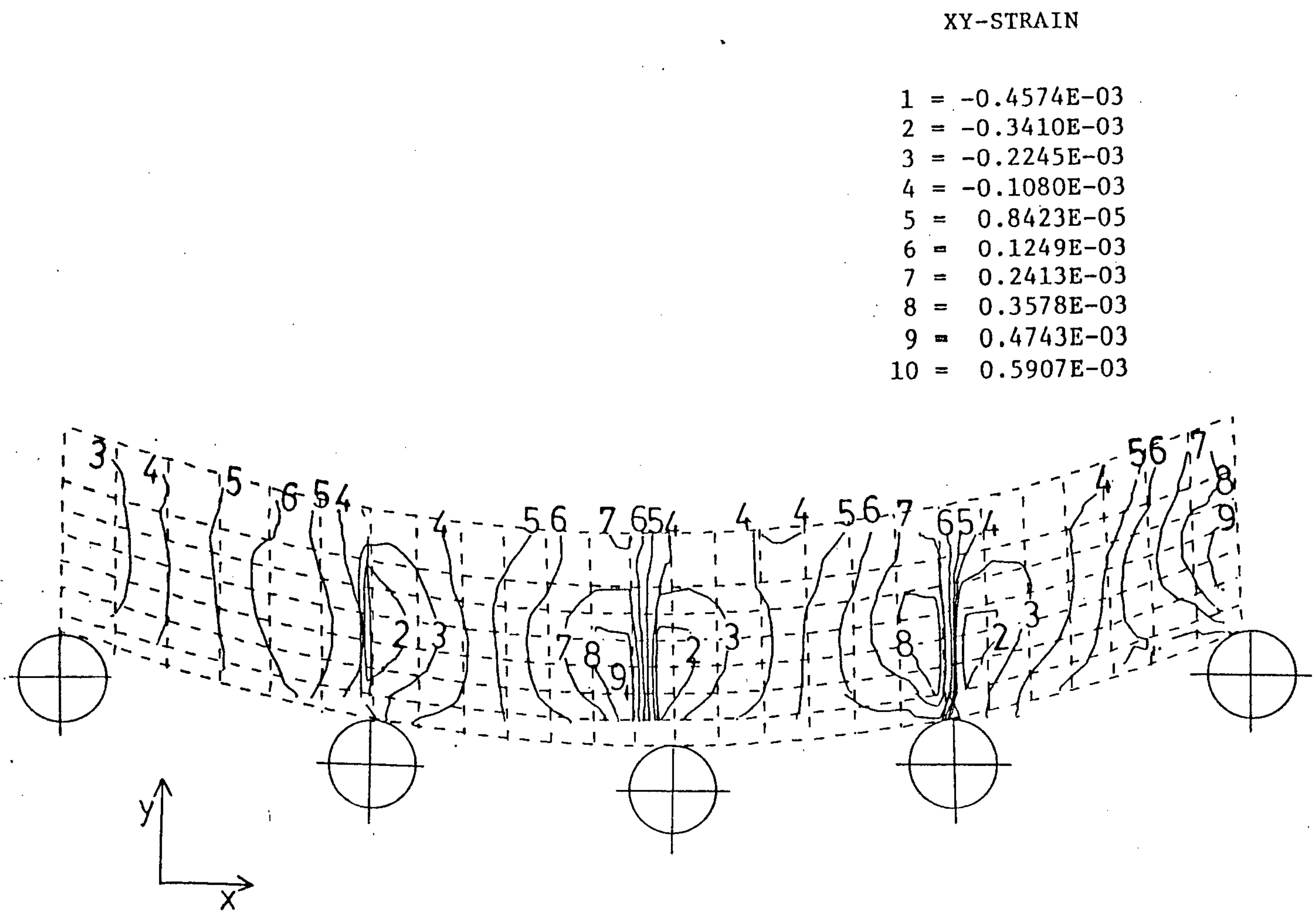

Fig. 5.18 Predicted XY-STRAIN Due to Bulging in Case 1. (Lower Shell)

Table V Maximum bulging deflection between No.1 and No.2 rolls.

		Bulging δ_B (mm)	Bending and Bulging δ_T (mm)
CASE 1.	U	0.22	0.87
	L	0.22	0.39
2.	U	0.13	0.26
3.	U	0.11	0.17
	L	0.11	0.12
4.	U	0.15	0.40
5.	U	0.13	0.22
6.	U	0.08	0.16
7.	U	0.21	0.51
8.	U	0.10	0.12
9.	U	0.14	0.35
10.	U	0.17	0.39

U : upper shell , L : lower shell

locations of which are roughly symmetrical with respect to the center plane of the slab thickness, 7 and 14 mm respectively from the inner surface of each shell as shown in Figs.5.19 and 5.20. Therefore the bending strain distributions of the upper and lower shells also are symmetrical with respect to the center plane of slab thickness.

Small peak strains are observed between Roll No.-1 and the tangent(0) roll at the inner surface; however this peak can be attributed to the simplifying approximations of the upstream boundary condition and the simulation of a dynamic process by a two-stage bending model. To check the effect of the bending simulation a three-stage bending model was run and the peak strain at this location was found to decrease and to move further downstream. Despite these simplifications, the strain and stress distributions at the bending point and downstream of it should be reasonably accurate owing to the good agreement that was obtained between the model predictions and the plant data on the occurrence of internal cracks described earlier.

Fig.5.21 shows the predicted curvature, ρ , of the strand, where ρ was calculated from the results of bending strain as follows;

$$\rho = (\varepsilon_2 - \varepsilon_1)/\Delta y \qquad (16)$$

in which ε_2 =strain at outer surface

ε_1 =strain at inner surface

Δy =distance between outer and inner surfaces

As to the question of whether the strand is straightened along the roll profile or not, the results show that bending occurs along the curvature determined by the roll profile as shown in Fig.5.21. A similar finding has been reported by Onishi[31] for the one-dimensional dynamic analysis of bending of continuously cast slabs.

Fig.5.22 shows the relationship between bending strain in the upper shell and roll pitch for different surface temperatures at the straightening point. Geometrical strain, which was calculated by assuming a neutral axis at the center plane of the slab thickness, also is shown on the same figure as a broken line for comparison(y is the distance from the center plane). From the results, it is evident that the bending strain is independent of roll pitch and smaller than the above geometrical strain by about 0.3%. However, a small dependence can be seen on the surface temperature;the bending strain increases by 0.05% with a temperature increase of 90°C because the stiffness of the strand is diminished so that the deformation is localized around the bending point. Thus, the elongation due to bending is enhanced at the straightening zone at higher temperatures.

Figs.5.23 and 5.24 show the relationship between bending strain and shell thickness for the 10.5m and 8.0m machine radii. The bending strain distributions in the upper and lower shells are seen to be symmetrical and the bending strain at the inner surface changes linearly with an increase in shell thickness. According to these results, the bending strain at the inner surface of the upper shell can have a negative value if the shell thickness is larger than 106 mm.

Fig.5.25 shows the influence of machine radius(curvature) on bending strain in the upper shell. The bending strain at the outer surface increases linearly with a change of curvature. However, the strain at the inner surface is not much influenced by the change of machine radius. The reason is that the neutral axis of bending is located very close to the inner surface and therefore the strain at the inner surface is almost independent of curvature.

5.2 Corner strain and crack formation

Although this analysis has focused on stresses and strains at the longitudinal mid-plane of a slab it is possible to estimate strain at the corner as well,based on insight gained from the three-dimensional,elasto-plastic calculations. If bulging is neglected the strain distribution in the edge shell is a result of bending which can be calculated by considering a neutral axis at the center of the slab thickness. Table VI presents the predicted bending strains at the corner close to the solidification front as well as bulging and bending strain at the inner surface of the shell in the mid-

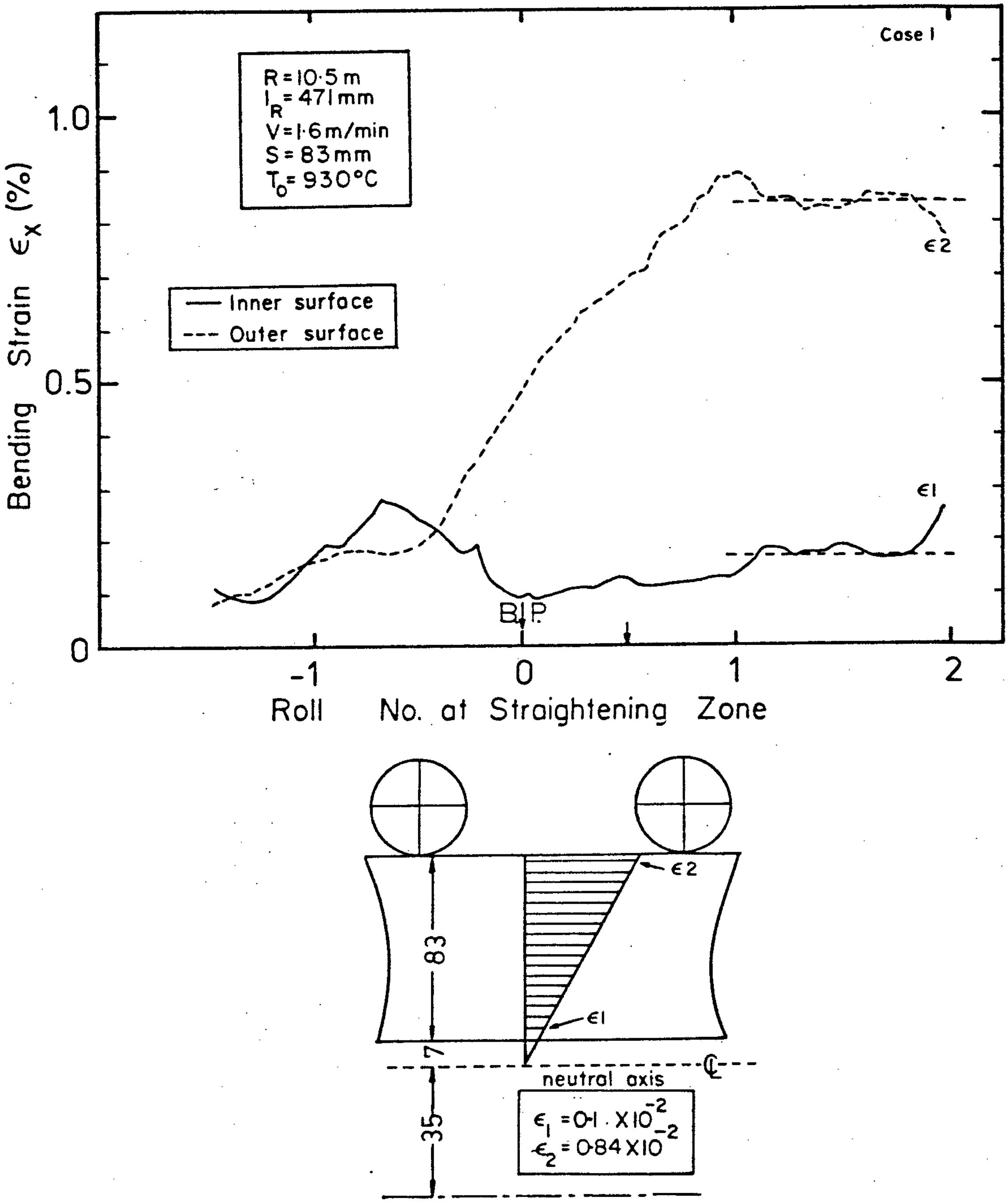

Fig. 5.19 Predicted Bending Strain, ε_x in Case 1. (Upper Shell, V=1.6m/min)

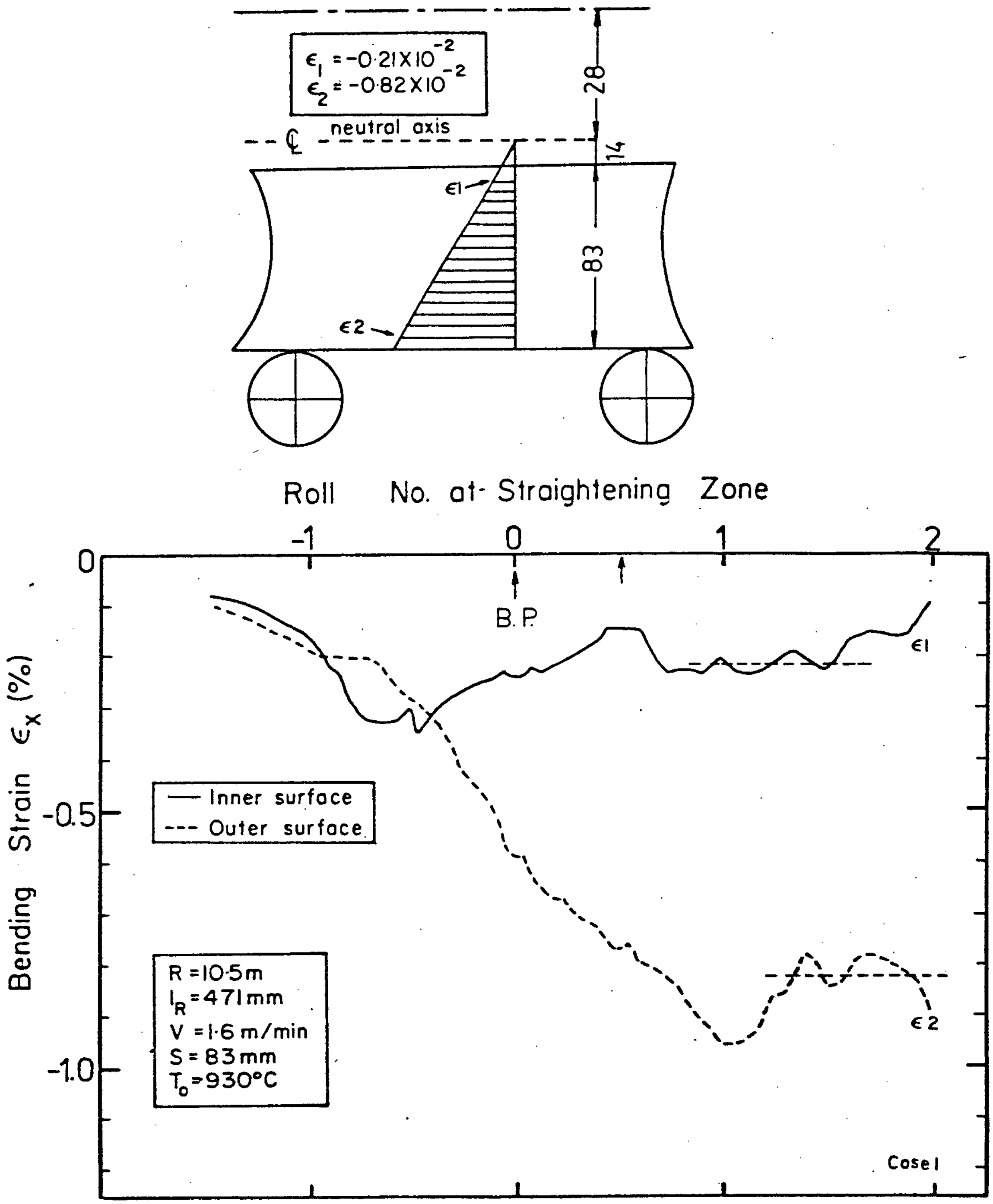

Fig. 5.20 Predicted Bending Strain, ε_x in Case 1. (Lower Shell, V=1.6m/min)

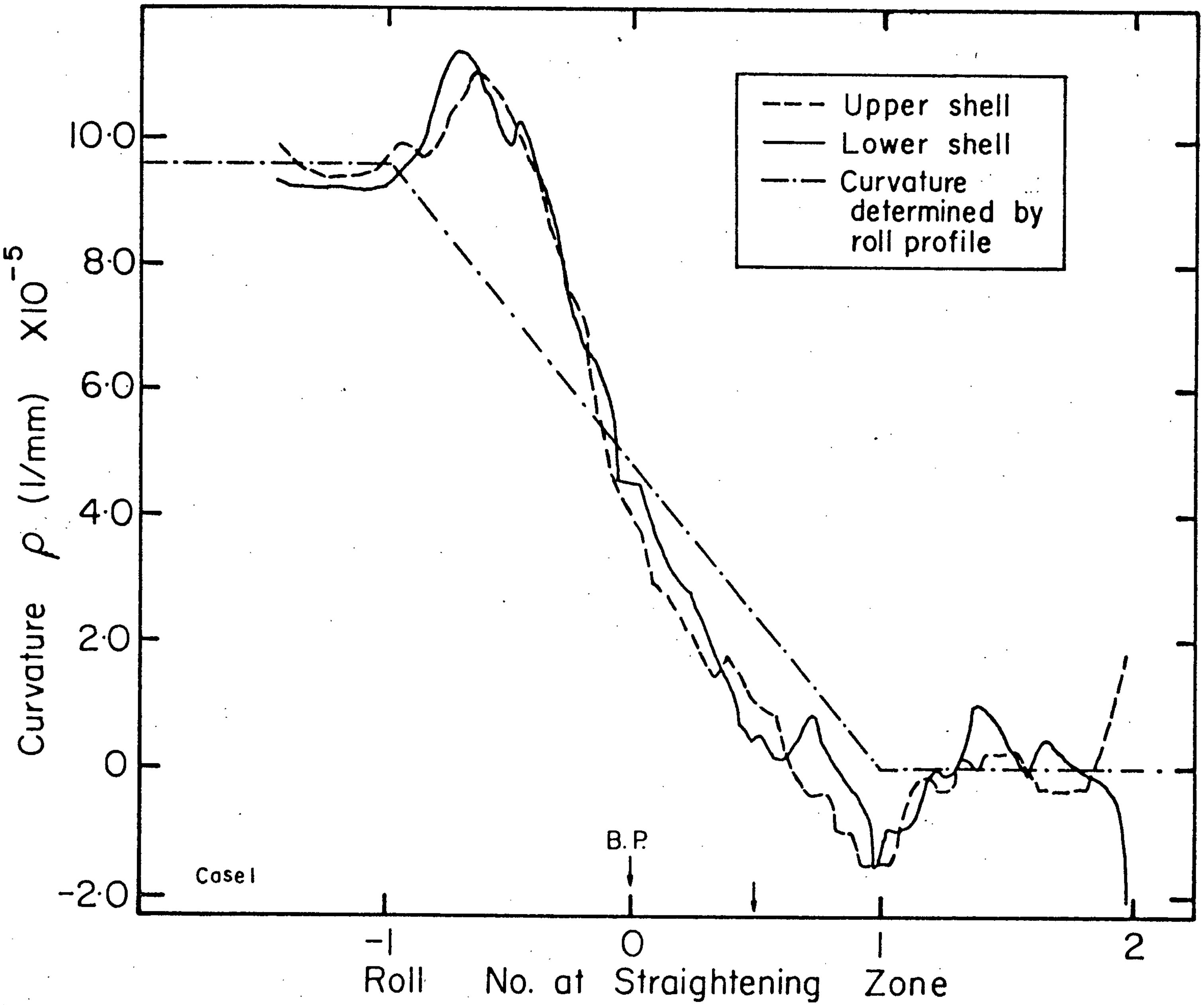

Fig. 5.21 Predicted Curvature of the Shell Due to Bending in Case 1.

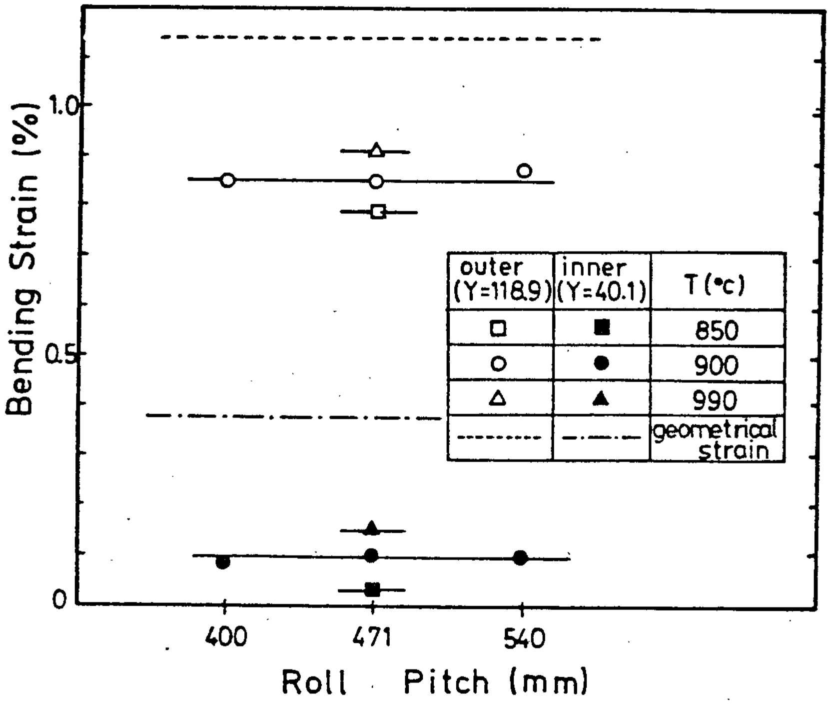

Fig. 5.22 Relation between Bending Strain, ε_x and Roll Pitch Predicted by the Finite-Element Bending Analysis.

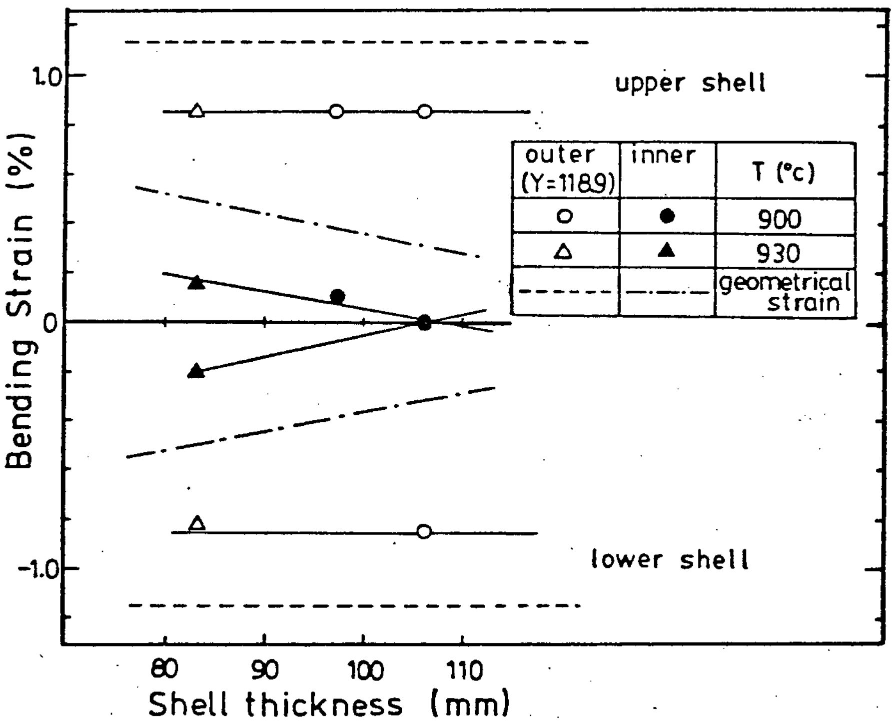

Fig. 5.23 Relation between Bending Strain, ε_x and Shell Thickness Predicted by the Finite-Element Bending Analysis. (Machine Radius = 10.5m)

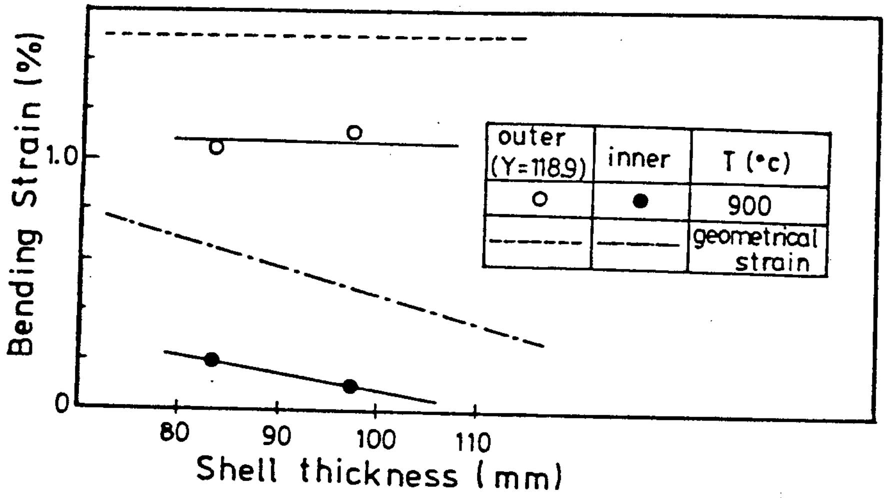

Fig. 5.24 Relation between Bending Strain, ε_x and Shell Thickness Predicted by the Finite-Element Bending Analysis. (Machine Radius = 8.0m)

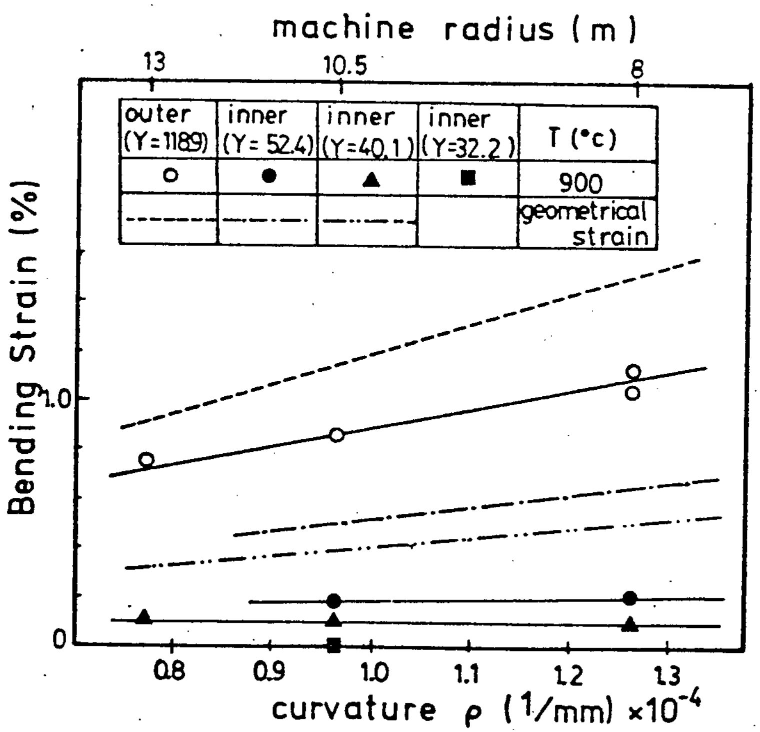

Fig. 5.25 Relation between Bending Strain, ε_x and Machine Radius (Curvature) Predicted by the Finite-Element Bending Analysis.

plane. From the results of Case 2,4,5,6 and 7, low surface temperatures and small roll pitches are preferable to prevent internal cracks in the mid-plane, since these conditions suppress the bulging strain. In the case of an 8m machine radius(Case 8,9), the threshold casting speed to ensure that internal cracks do not appear at the corner is 0.9m/min(based on the critical strain). For a 13m machine radius (Case 10), the internal cracks occur in the mid-plane due to bulging,and the threshold casting speed is nearly 1.4m/min (based on the critical strain). Thus, in one point bending bow-type casters, the small machine radius of 8.0m is obviously unfavorable compared with the values of 10.5m and 13m owing to the low casting speed at which cracks form.

5.3 Creep effects on the critical strain

The critical strain for internal cracks reported in the literature exhibits some scatter(0.2-3.0% at a strain rate of 1×10^{-4} s^{-1}) as mentioned previously in Section 2.1. In the present study, the estimated value of the critical strain is 0.25-0.3% at a strain rate of 3×10^{-4} s^{-1} based on the appearance of cracks in slabs. However, this critical value may be an underestimate since creep has not fully been accounted for in this analysis. Creep effects have been taken into account partially by considering an approximate strain rate for the stress-strain curves. If the model were able to consider creep the bulging strain would be increased and as a result the

Table VI Bending and Bulging strain at solidification front.

	center ε_x %	corner $\varepsilon_x (= \frac{y}{R})$ %	internal cracks
CASE 1. U	0.55/0.65	0.4	center , corner
L	0.1	-0.4	no crack
2. U	0.25/0.3*	0.27	(*critical strain)
3. U	0.15/0.2	0.18	no crack
L	0.1/0.13	-0.18	no crack
4. U	0.38/0.4	0.27	center
5. U	0.15/0.23	0.27	no crack
6. U	0.15/0.20	0.27	no crack
7. U	0.3/0.4	0.27	center
8. U	0.15/0.2	0.35	corner
9. U	0.35/0.4	0.53	center , corner
10. U	0.3/0.33	0.21	center

U : upper shell , L : lower shell

total strain of bending and bulging should be increased.

Fig.5.26 shows the total strain, ε_T, as a function of bulging strain, ε_B, and bending strain, ε_u. From the results, the correlation among these variables is as follows;

$$\varepsilon_T = (2 - 5)\varepsilon_B + \varepsilon_u \tag{17}$$

As is apparent from Eq.(17), bulging strain affects the total strain significantly and hence creep effects on bulging should be considered to determine the critical strain more precisely. If, for instance, bulging strain is increased from 0.06% to 0.12% at the bending strain of 0.1% which is a condition of Case 2, the critical strain will be increased easily from 0.25% to 0.6%, see Fig.5.26.

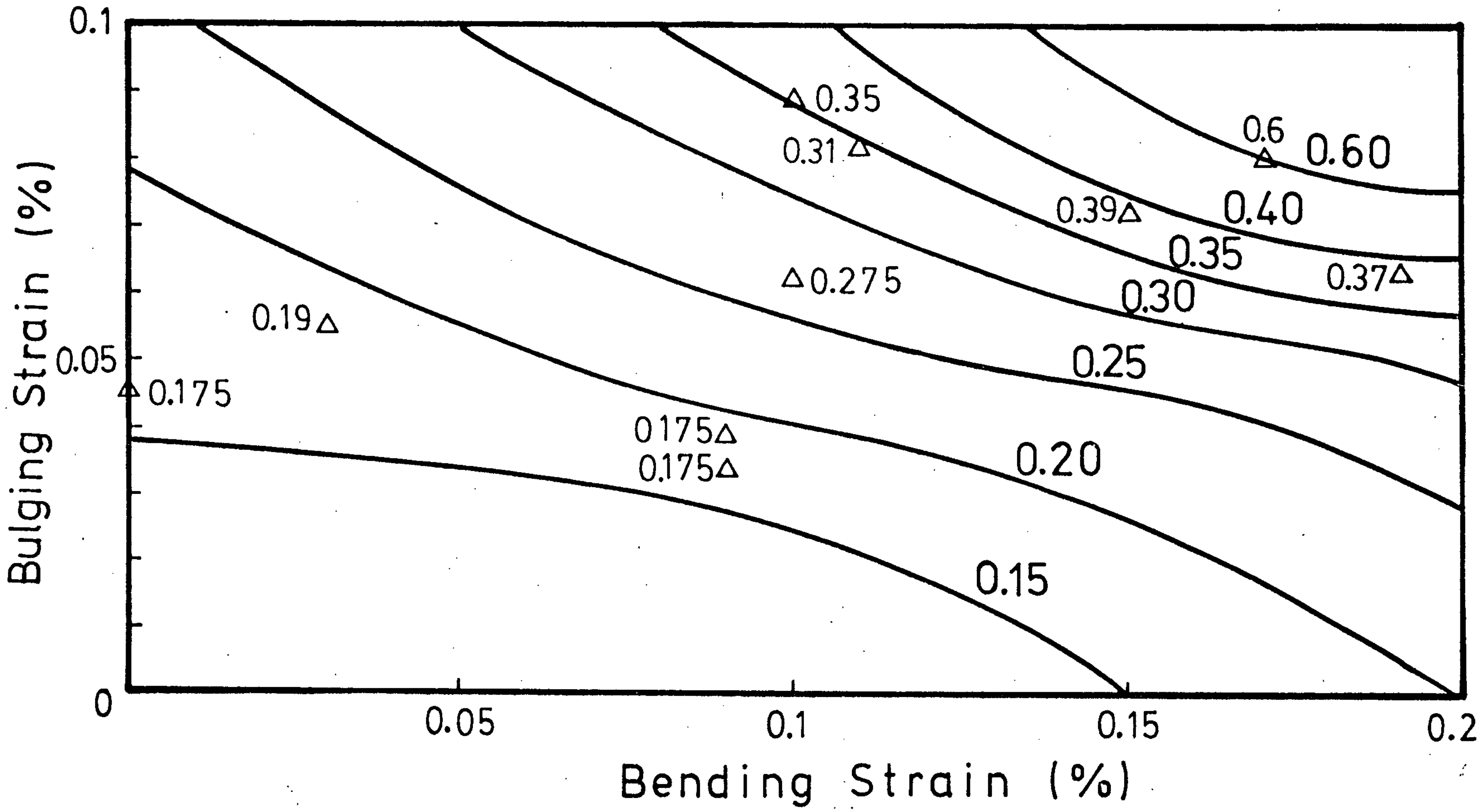

Fig. 5.26 Predicted Total Bending and Bulging Strain, ε_T, at an Inner Surface as a Function of Bulging Strain, ε_B, and Bending Strain, ε_u.

Chapter 6

CONCLUSIONS AND SUGGESTIONS FOR FUTURE WORK

6.1 Conclusions

A two-dimensional elasto-plastic model has been developed, based on the plane-stress finite-element method to calculate the bending and bulging deformation of partially solidified continuously cast steel slabs during straightening. The findings of the study are as follows;

(1) The model predictions of internal cracks showed good agreement with the plant data of Oita works, NSC. The internal cracks are predicted to occur mainly in the upper shell beneath the roll support points in the straightening zone based on a critical cracking strain of 0.25 to 0.3% at a strain rate of 1×10^{-4} s^{-1}.

(2) The upper and lower shells deform independently about their respective neutral axes.

(3) The roll friction force plays the most important role in the bending analysis and a value of 0.45 was adopted for the coefficient of roll friction. Owing to the restraint exerted on the strand by the roll friction force the neutral axes of the two shells shift inward, past the solidification front into the molten steel, and as a result the upper and lower shells deform like a single beam. The neutral axes of the upper and lower shells are located very close to their respective solidification fronts.

(4) The strain distribution of ε_x is linear through the shell thickness and hence bending strain, ε_u , follows the ordinary bending beam theory.

$$\varepsilon_u = \frac{y}{R}$$

where y is the distance from the neutral axis and R is the bending radius.

(5) Bending occurs along the curvature determined by the roll profile.

(6) The bending strain depends slightly on the surface temperature of the strand increasing by 0.05% with a temperature increase of 90°C.

(7) The bulging deflection is enhanced significantly as a result of interaction with bending. The resultant bulging deflections are greater in the upper than in the lower shell .

(8) The shear strain, ε_{xy} , is comparable to the ε_x component in the case of the bulging analysis, whereas ε_{xy} is fairly small, close to one fourth of ε_x component, in the case of the combined bending and bulging analysis.

(9) The total strain, ε_T , can be expressed in terms of each component of bulging strain, ε_B , and bending strain, ε_u , as follows.

$$\varepsilon_T = (2 - 5)\ \varepsilon_B + \varepsilon_u$$

The bulging strain affects the total strain significantly and hence to prevent internal cracks it is important to suppress the bulging by ensuring low surface temperatures and have a small roll pitch in the straightening zone.

(10) The predicted critical strain for internal cracks is 0.25 - 0.30% at $1\times10^{-4}\ s^{-1}$ for low-carbon steels. However, it will be necessary to take into account

creep effects to obtain a more precise value of the critical strain.

(11) In one-point bending,bow-type casters, a small machine radius of 8m is obviously unfavorable compared with the values of 10.5m and 13m because at normal casting speeds the tensile strain at the solidification front exceeds the critical value for crack formation.

6.2 Suggestions for future work

An important direction for further research is the experimental measurement of several parameters adopted in the present model such as the coefficient of roll friction and the critical strain for internal cracks. The results of such an investigation would help conclusively establish the validity of the proposed model.

Then, an obvious extension of the work would be to develop a model for multi bending casters, which has been of great interest in the industry, based on the model for one point bending casters.

REFERENCES

1. A.Grill,J.K.Brimacombe and F.Weinberg: "Mathematical Analysis of Stresses in Continuous Casting of Steel" Ironmaking & Steelmaking ,No.1 ,1976, pp38-47

2. A.Grill and K.Sorimachi: "The thermal loads in the finite element analysis of elasto-plastic stresses" Numerical Methods in Engineering , Vol.14, 1979, pp499-505

3. W.T.Lankford : "Some Considerations of Strength and Ductility in the Continuous Casting Process" , Metl. Trans. , Vol.3 , 1972, pp1331-1357

4. T.Nakamura and M.Ueki : "The high temperature torsional deformation of a 0.06%C mild steel" , Trans. ISIJ, Vol.15, 1975, pp185-193

5. P.J.Wray : "Plastic deformation of austenitic iron at intermediate strain rates" ,Metal. Trans.A , 6A 1975,pp1189-1202
"Plastic Deformation of Delta-Ferritic Iron at Intermediate Strain Rates" ,Metal. Trans.A, 7A 1976, pp1621-1627

6. T.Sakai and K.Takeishi:"The effect of strain rate and temperature on the hot workability of 0.16%C-Fe" , The 18th Japan Congress on Materials Research, March 1975, pp63-68
" The effect of temperature, strain rate,and carbon content on hot deformation of carbon steels" , Tetsu-to-Hagane(J.Iron Steel Inst. Jpn), Vol.11, 1981, pp2000-2009

7. H.Mizukami,Y.Miyashita and K.Murakami : " Mechanical Properties of Continuously Cast Steels at Elevated Temperatures", Tetsu-to-Hagane ,Vol.63, 1977,S562

8. P.A.Jarvinen :" Representation of high-temperature plastic behavior of austenitic and ferritic stainless steels by empirical equations", Scand.J.Metal.,Vol.6 ,1977, pp79-82

9. J.J.Jonas,R.A.Petkovic and M.J.Luton: "Flow curves and softening kinetics in high strength low alloy steels" , TMS-AIME Fall Meet., 1977, pp68-81

10. T.Emi and K.Kinoshita :" Crack formation and tensile properties of strand-cast steels up to their melting points", Shefield Int. Conf. Solidification and Casting,2 1977, pp268-274

11. M.J.Stewart:"Hot Deformation of C-Mn Steels from 1100 to 2200°F with constant true strain rates from 0.5 to 140 S^{-1} ", TMS-AIME Fall Meet., 1977, pp47-65

12. A.Palmaers:"Mechanical Properties of steels at high temperatures as control tools for continuous casting" , Metallurg. Rep. CRM, No.53 1978, pp23-31
" Calculation of the mechanical and thermal stresses in continuously cast strands", Stahl u. Eisen, 99-Nr.19 , 1979 ,pp1039-1050

13. I.Y.Chernikhova: Russian Metallurgy,4 1978,pp108

14. J.Imamura : Tetsu-to-Hagane, 66 1981,S892

15. O.M.Puhringer: " Strand Mechanics for continuous casting plants" , Stahl u. Eisen, 96-Nr.6, 1976, pp279-284

16. A.Niedermayr,F.G.Rammerstorfer,D.F.Fischer and C.Jaquemar: " The thermal and thermo-visco-elasto-plastic processes during continuous casting of steel ", Arch. Eisenhuttenwes, 51-Nr.2, 1980, pp67-72

17. K.Kinoshita,T.Emi and M.Kasai: " Thermal Elasto-Plastic Stress Analysis of Solidifying Shell in Continuous Casting Mold", Tetsu-to-Hagane, Vol.65,1979, pp2022-2031

18. G.G.Konradi: Zasodskays Pabor, 27-10, 1961, pp1296

19. Y.Yamada: " EPIC-IV" , Baifu-kan ,1981

20. K.Sorimachi and T.Emi : Tetsu-to-Hagane, Vol.63, 1977,pp1297

21. K.Miyazawa and K.Schwerdtfeger: " Computation of bulging of continuously cast slabs with simple bending theory", Ironmaking and Steelmaking, No.2 1979, pp68-74

22. A.Grill and K.Schwerdtfeger: " Finite-element analysis of bulging produced by creep in continuously cast steel slabs", Ironmaking and Steelmaking, No.3 1979, pp131-135

23. K.Fukawa,K.Nakajima and H.Matsumoto: " Rheological Analysis of Bulging of Continuously Cast Slabs with Elementary Bending Theory" , Tetsu-to-Hagane, Vol.68, 1982, pp794-798

24. H.Fujii,T.Ohashi,M.Oda,R.Arima and T.Hiromoto: " Analysis of Bulging in Continuously Cast Slabs by the Creep Model", Tetsu-to-Hagane, Vol.67,1981, pp1172-1179

25. T.Matsumiya and Y.Nakamura: Tetsu-to-Hagane ,Vol.68, 1982,A145

26. Morita : Kobe-seiko-giho, 29-3 ,1979, pp55-59

27. K.Wunnenberg: Stahl u. Eisen, 98 , 1978, pp254-259

28. O.C.Zienkiewicz: " The Finite Element Method in Engineering Science", New York, McGraw-Hill, 1974

29. Y.Yamada : " Recent advances in matrix methods of structural analysis and design", 1969

30. R.Hill : " The theory of combined plastic and elastic deformation with particular reference to a thick tube under internal pressure", Proceedings of the Royal Society, A.Vol.191, 1947, pp278-303

31. K.Onishi,K.Nagai and M.Wakabayashi: " A numerical analysis of strains in slabs and forces on rollers in the straightening zone of continuous casting machine", Tetsu-to-Hagane, Vol.67, 1981,pp1162-1171

32. J.A.Schey: " Metal deformation processes(Friction and Lubrication)", MARCEL DEKKER, New York, 1970

33. Suzuki: Trans. Japan Institute of Metals, 32, 1968, pp1301

34. T.Inoue and H.Tanaka: " Progress in large-section slab continuous casting techniques at Nippon Steel Corporation", Nippon Steel Technical Report, No.13, June 1979 ,pp1-23

35. N.Yamauchi,H.Misumi,Y.Uchida and T.Yamamoto: " Internal Cracks in Continuously Cast Slabs", Nippon Steel Technical Report, No.13, June 1979, pp62-72

36. S.S.Daniel :" Roll Containment Model for Strand-Cast Slab and Blooms", 2nd Process Technology Conf.,Chicago, 1981, pp102-113

37. K.Narita,T.Mori and J.Miyazaki: " Effect of Deformation on the Formation of Internal Cracks in Continuously Cast Blooms", Tetsu-to-Hagane, Vol.67, 1981, pp1307-1316

38. H.Suzuki: " Characteristics of Embrittlement in Steels above 600°C", Tetsu-to-Hagane, Vol.65, 1979,S2038

39. T.Matsumiya: Tetsu-to-Hagane, Vol.69, 1983, S169

40. T.Obinata : " General View of the Continuous Casting Equipment", Tetsu-to-Hagane, Vol.60, 1974, pp741-754

41. F.Weinberg: " The Ductility of Continuously Cast Steel Near the Melting Point - Hot Tearing", Metal.Trans.B, Vol.10B ,June 1979, pp219-227

42. H.Suzuki,S.Nishimura and S.Yamaguchi: " Characteristics of hot ductility in steels subjected to the melting and solidification", Trans.ISIJ, Vol.22, 1982, pp48-56

43. G.Komma : " Design and Operational Aspects in Continuous Casting of Wide Slabs", Iron and Steel Eng., June 1973, pp68-73

44. A.Vaterlaus :" Finite element analysis for slab straightening with liquid core", Tetsu-to-Hagane, Vol.69, 1982,S170

45. S.Nagata and K.Yasuda: Tetsu-to-Hagane, Vol.68, 1982, S991

46. H.Misumi : Private Communication

APPENDIX I

MECHANICAL PROPERTIES ADOPTED IN THE BULGING CALCULATION FOR THE COMPARISON WITH THE EXPERIMENTAL RESULTS OF Morita

	Material 1	Material 2	Material 3	Material 4
T (°C)	1101	1205	1309	1413
E MPa	17738	15827	13916	10123
σ_Y MPa	14.8	10.1	6.3	2.4
ν	0.36	0.37	0.38	0.39
	$\sigma = 75.4\,\varepsilon^{0.23}$	$\sigma = 47.0\,\varepsilon^{0.21}$	$\sigma = 21.5\,\varepsilon^{0.16}$	$\sigma = 6.0\,\varepsilon^{0.11}$

APPENDIX II

DERIVATION OF THE FINITE-ELEMENT EQUATIONS FOR THE ELASTO-PLASTIC PROBLEMS

Displacements $\{\delta\}$ within each element are given by

$$\{\delta\} = [N]\ \{\delta\}^e \tag{A.1}$$

where $[N]$ is a matrix of shape functions and $\{\delta\}^e$ is a vector of nodal displacements. The strain $\{\varepsilon\}$ and stress $\{\sigma\}$ in the element are given by

$$\begin{aligned} \{\varepsilon\} &= [B]\ \{\delta\}^e \\ \{\sigma\} &= [D]\ \{\varepsilon\} \end{aligned} \tag{A.2}$$

By applying the principle of virtual work to these elements and summing the individual equilibrium equations for all elements, Eq.(A.3) is obtained. The nodal forces, displacements and the distributed loads $\{P\}$ can now be related through

$$\{ F \} = [K] \{ \delta \} + \{ Fp \} \quad \text{(A.3)}$$

where $[K] = \Sigma \int [B]^T [D] [B] \, d\,(vol)$

and $\{ Fp \} = - \Sigma \int [N]^T \{ P \} \, d\,(vol)$

Σ - summation over all elements.

Equation (A.3) can be solved for the displacements.

$$\{ \delta \} = [K]^{-1} (\{ F \} - \{ Fp \}) \quad \text{(A.4)}$$

Finally, using Eq.(A.2) , one can calculate the strain and stress distribution over the entire region.

Under conditions of plastic deformation the stress analysis is more complicated since the [D] and [K] matrices become strain(or stress) dependent. Therefore Eq.(A.3) is solved by an incremental method.[29] The load is applied incrementally and the [K] matrix is adjusted after every increment. The load increments are adjusted, such that with each increment 30 elements yield. After all elements yield, the remaining load is divided into several equal increments.

Nomenclature; [ ] matrices

{ } vectors

** details of the derivations are discussed by Zienkiewicz[28] and Yamada[29].

APPENDIX III

MATERIAL MATRIX[D](plane stress) USED IN THE FINITE ELEMENT

Below the yield point, the elastic matrix $[D^e]$ for the plane stress condition is given by

$$[D^e] = \frac{E}{1-\nu^2}\begin{bmatrix} 1 & \nu & 0 \\ & 1 & 0 \\ \text{sym} & & \frac{1-\nu}{2} \end{bmatrix} \tag{B.1}$$

where E is the Young's Modulus and ν is Poisson's ratio.

Under conditions of plastic deformation, the plastic matrix $[D^p]$ which was developed by Yamada[19] for a Mises material is as follows.

$$[D^p] = \frac{E}{1-\nu^2}\begin{bmatrix} 1 & \nu & 0 \\ & 1 & 0 \\ \text{sym} & & \frac{1-\nu}{2} \end{bmatrix} - \begin{bmatrix} \frac{S_1^2}{S} & \frac{S_1S_2}{S} & \frac{S_1S_6}{S} \\ & \frac{S_2^2}{S} & \frac{S_2S_6}{S} \\ \text{sym} & & \frac{S_6^2}{S} \end{bmatrix} \tag{B.2}$$

where
$$S = \frac{4}{9}\bar{\sigma}^2 H' + S_1\sigma'_x + S_2\sigma'_y + 2S_6\tau'_{xy}$$

and
$$S_1 = \frac{E}{1-\nu^2}(\sigma'_x + \nu\sigma'_y),\ S_2 = \frac{E}{1-\nu^2}(\nu\sigma'_x + \sigma'_y),\ S_6 = \frac{E}{1+\nu}\tau'_{xy}$$

$$H' = \frac{d\bar{\sigma}}{d\bar{\varepsilon}^P}$$

$\bar{\sigma}$ and $\bar{\varepsilon}^P$ are the effective stress and strain and H' is the slope of the $\bar{\sigma}$, $\bar{\varepsilon}^P$ curve. σ_x', σ_y' and τ_{xy}' are deviatoric stresses.

Unloading check has been performed by calculating $d\bar{\varepsilon}^P$ as follows.

$$d\bar{\varepsilon}^P = \frac{S_1 d\varepsilon_x + S_2 d\varepsilon_y + S_6 d\gamma_{xy}}{\frac{3}{2}\frac{S}{\bar{\sigma}}} \quad \text{(B.3)}$$

if $d\bar{\varepsilon}^P < 0$ .... unloading

Once unloading occurs, the material matrix of the element is changed from $[D^p]$ to $[D^e]$.

APPENDIX IV

THICK-WALLED CYLINDER UNDER INTERNAL PRESSURE(plane strain)

To check the accuracy of "EPIC-IV", a calculation was performed for the case of a thick-walled cylinder under internal pressure for which an analytical solution of the stress field is available. The geometry of the cylinder $a \le r \le b$ is shown in Fig.IV.1. The elasto-plastic boundary is located at $r=c$. The displacements in the θ direction on the radial boundaries were constrained due to the axial symmetry. The dimensions of the cylinder were selected as $b=2a$, in order to compare the numerical results with the analytical solution of Hill[30]. Mechanical properties of the material were as follows:

Poisson's ratio	$\nu=0.3$
Shear modulus	$G=4\times10^6$ psi
Young's modulus	$E=10.4\times10^6$ psi
Yield stress	$\sigma_Y=100\sqrt{\frac{3}{2}}=86.6$ psi
	$H'=\frac{d\bar{\sigma}}{d\bar{\varepsilon}^p}=0.01$

The stress σ_z depends on the strain history and must be obtained from the Prandtl-Reuss equations. Fig.IV.2 shows the comparison of the calculated σ_z in dimensionless form with those of Hill. Excellent agreement is observed.

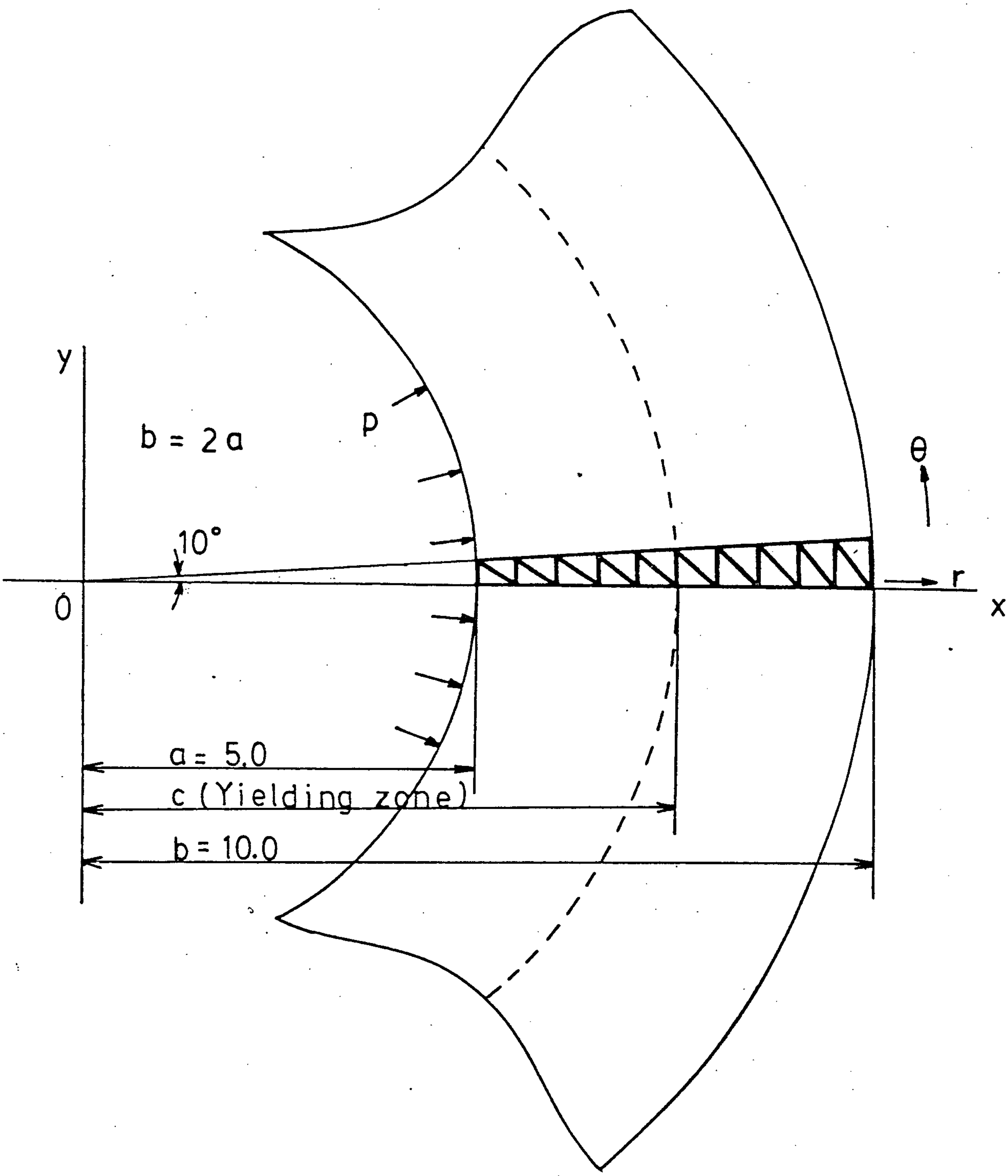

Fig. IV.1 Geometry of a Thick Walled Cylinder.

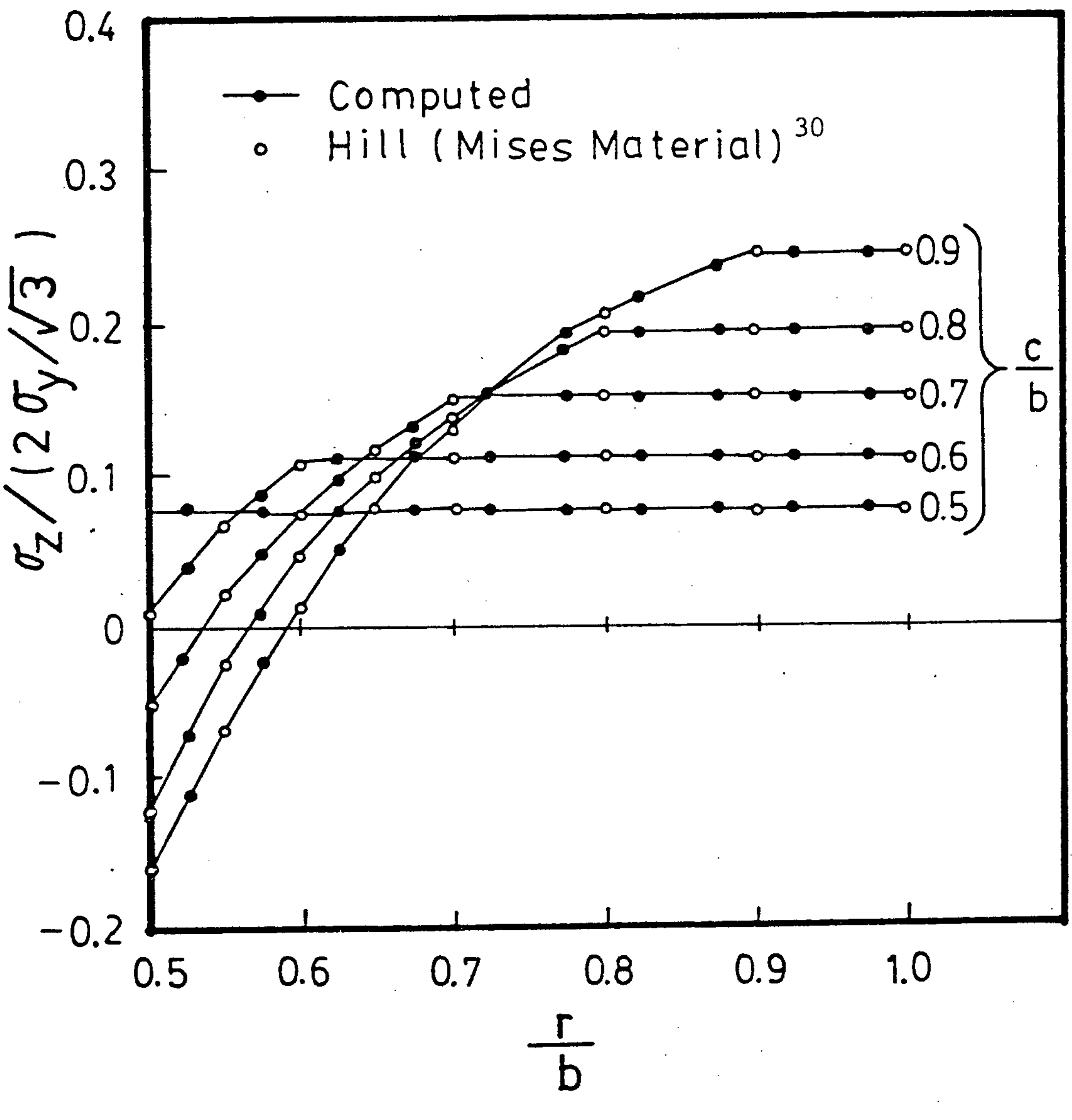

Fig. IV.2 Comparison of the Calculated Stresses σ_z (solid points and lines) with Those Obtained by Hill[30].

APPENDIX V

ESTIMATION OF ROLL FRICTION FORCE IN CASE 1(UPPER SHELL)

Roll No.	Roll Pitch mm ℓ_R	Roll Friction Force N F_i	Cumulative Roll Friction Force N ΣF_i	Stress MPa σ_i	Average Strain % ε_i	Elongation mm $\Delta\ell_i$
11	435	133.2	0	0	0	0
10	435	136.2	133.2	6.4	0.008	0.03
9	435	137.2	269.4	12.9	0.02	0.08
8	435	140.1	406.6	19.6	0.03	0.13
7	435	141.1	546.7	26.3	0.035	0.15
6	435	143.1	689.8	33.2	0.06	0.26
5	435	143.1	832.9	40.1	0.095	0.41
4	435	148.9	981.8*	47.3	0.15	0.65
3	471	157.7	1139.5	54.9	0.32	1.51
2	471	157.7	1297.2	62.5	0.48	2.28
(B.P.) 1	471	157.7	1454.9	70.1	0.71	3.36
					Total	8.86

* Fu = 981.8 N is adopted as the force boundary condition on upstream edge. (Fig.3.13)

APPENDIX VI

RESULTS OF CALCULATION OF BENDING AND BULGING

(CASE 2 TO CASE 10)

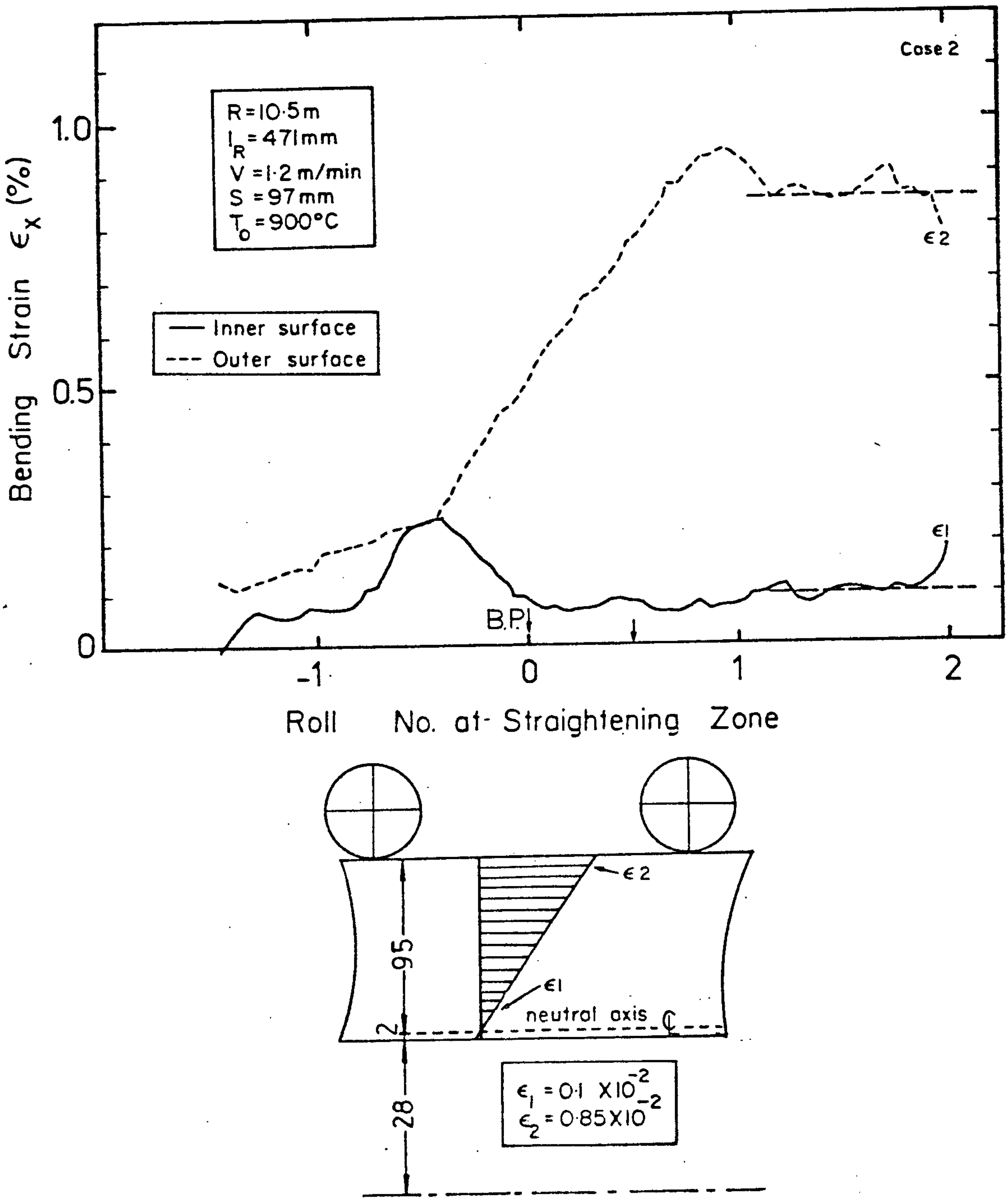

Fig. VI.1 Predicted Bending Strain, ϵ_x in Case 2. (Upper Shell)

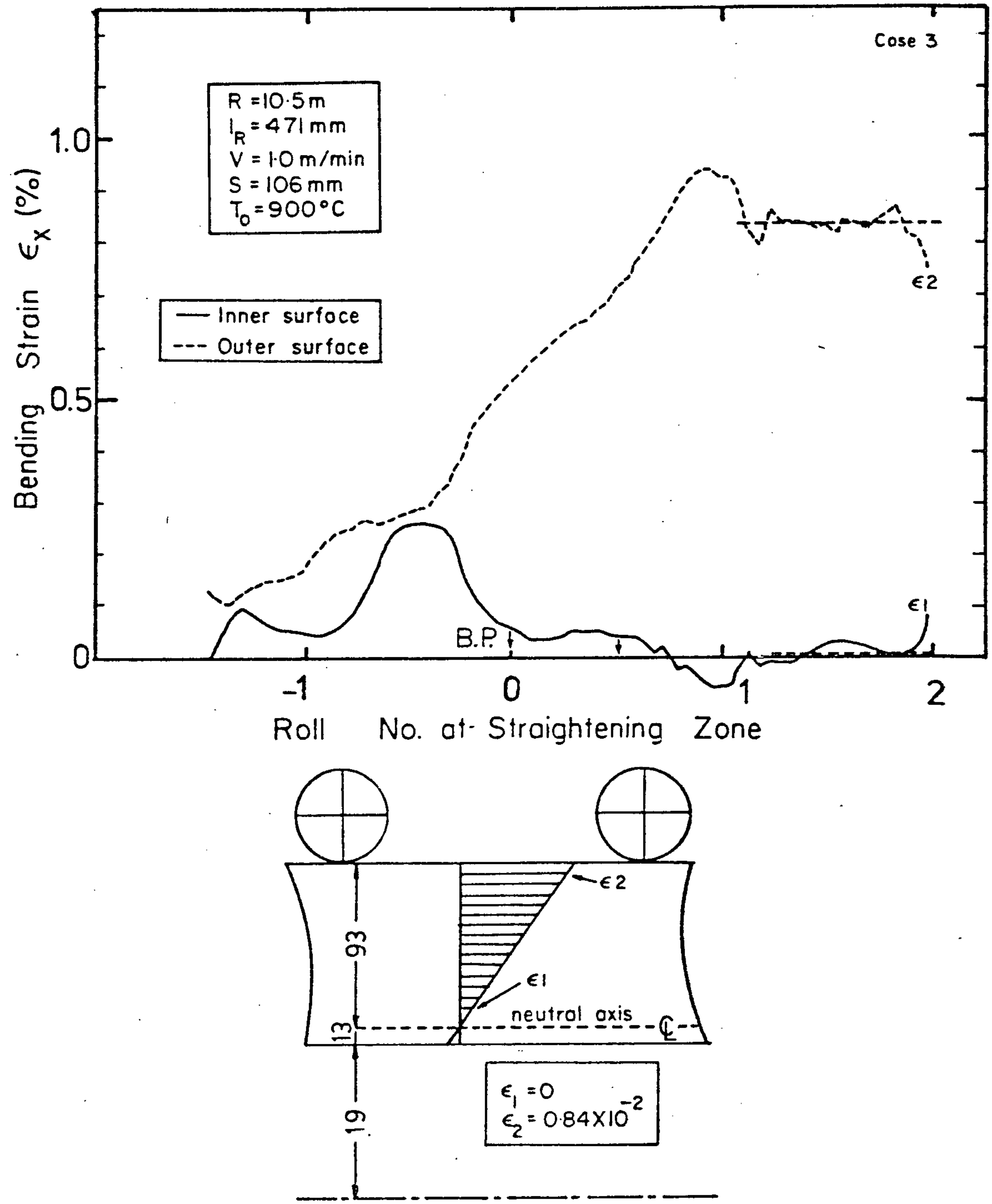

Fig. VI.2 Predicted Bending Strain, ϵ_x in Case 3. (Upper Shell)

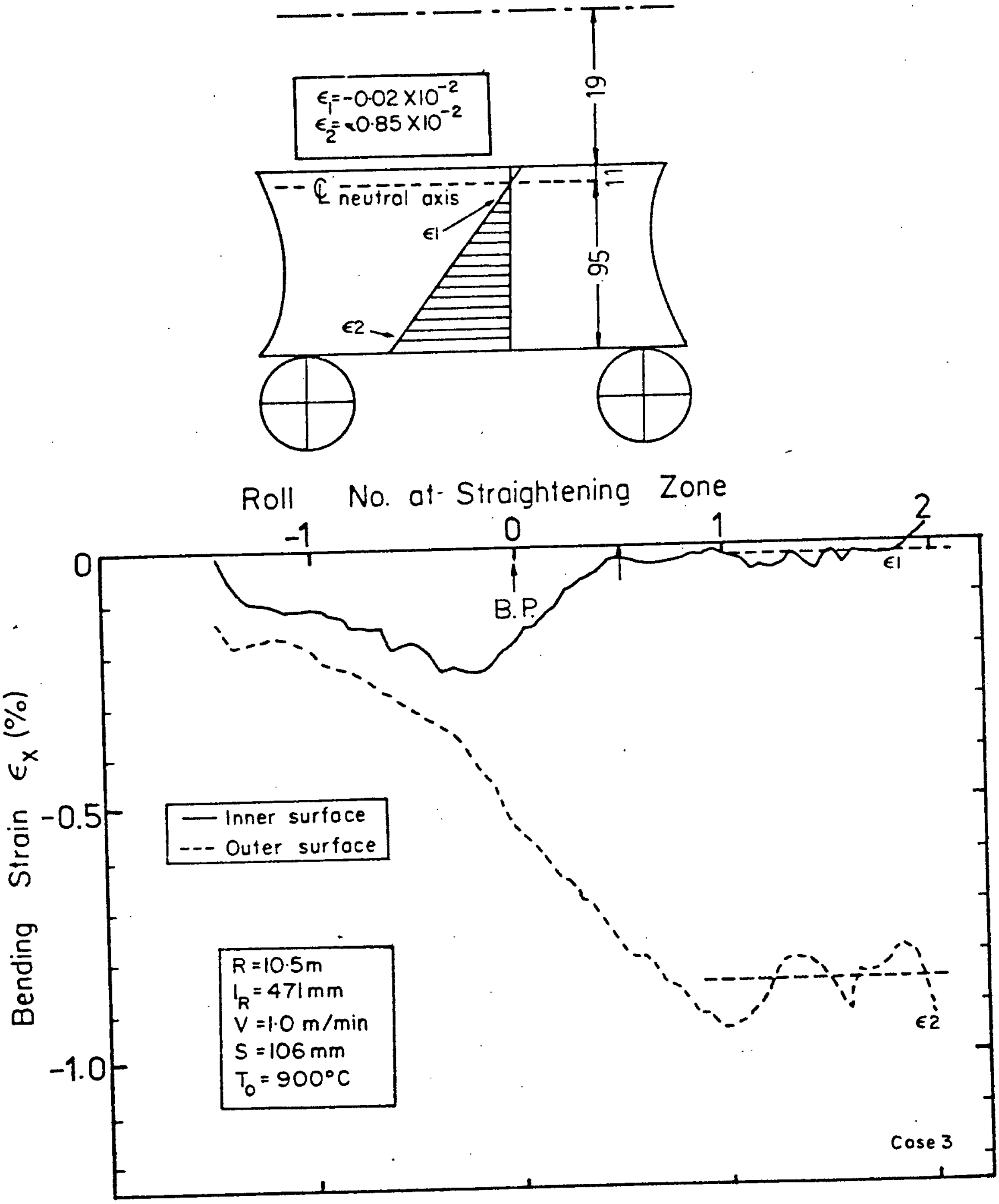

Fig. VI.3 Predicted Bending Strain, ε_x in Case 3. (Lower Shell)

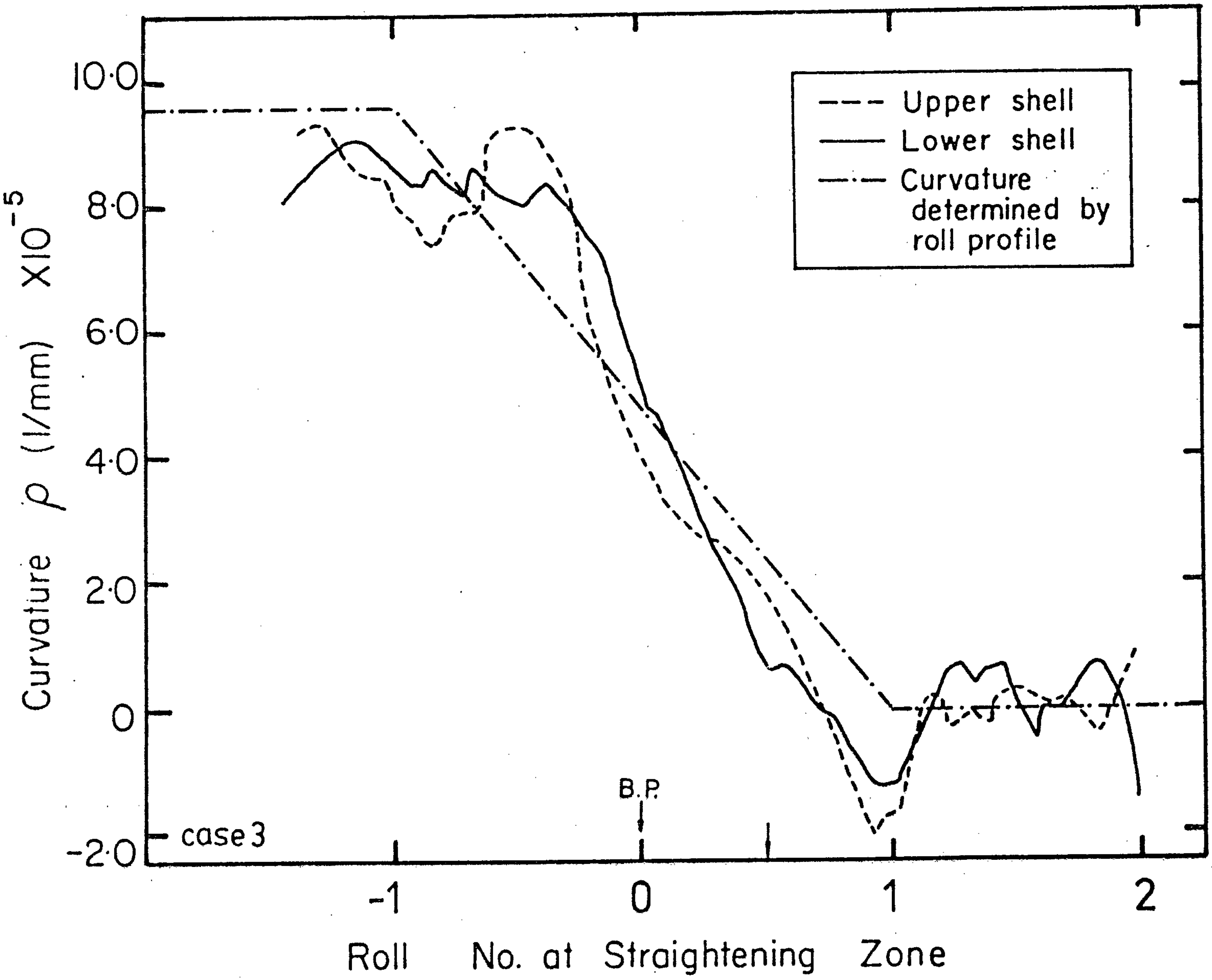

Fig. VI.4 Predicted Curvature of the Shell Due to Bending in Case 3.

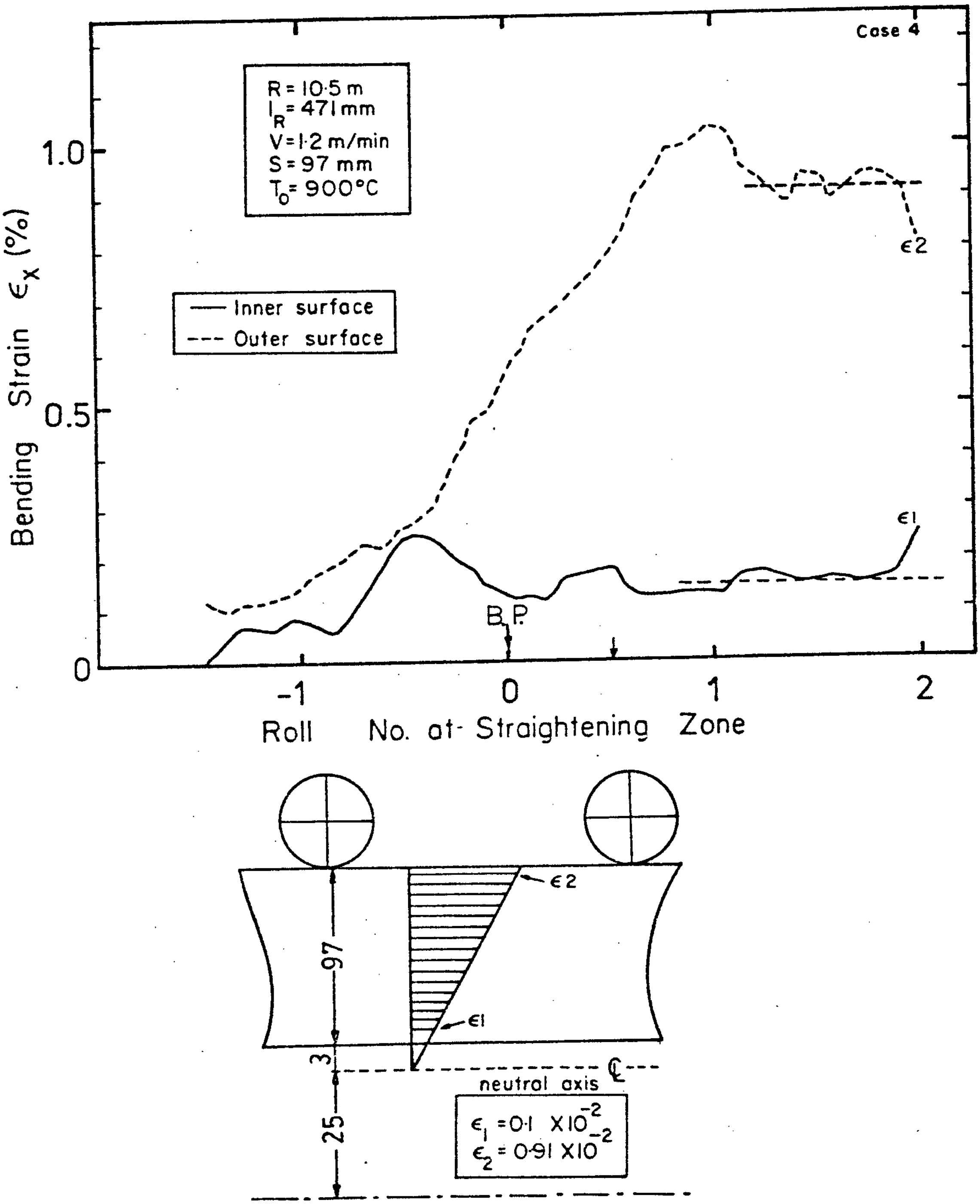

Fig. VI.5 Predicted Bending Strain, ε_x in Case 4. (Upper Shell)

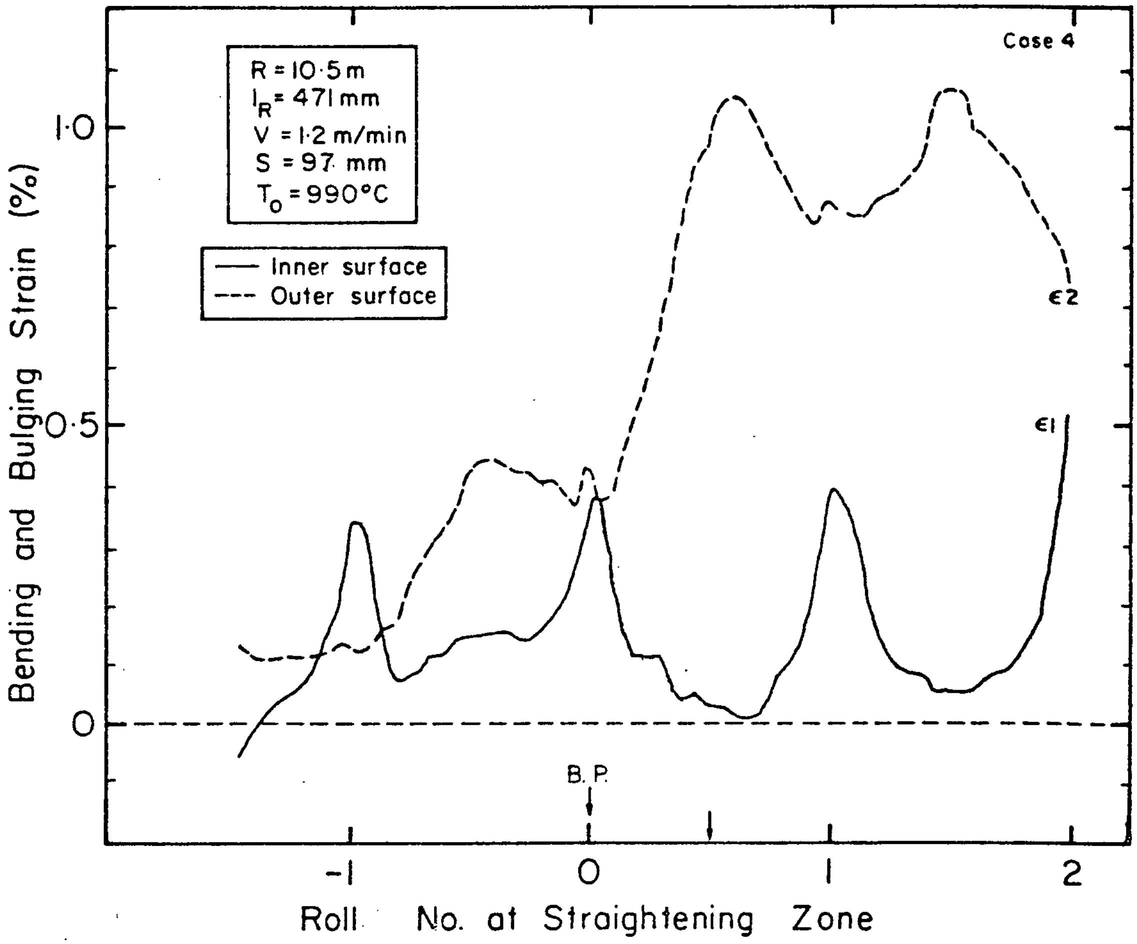

Fig. VI.6 Predicted Bending and Bulging Strain, ε_x in Case 4. (Upper Shell)

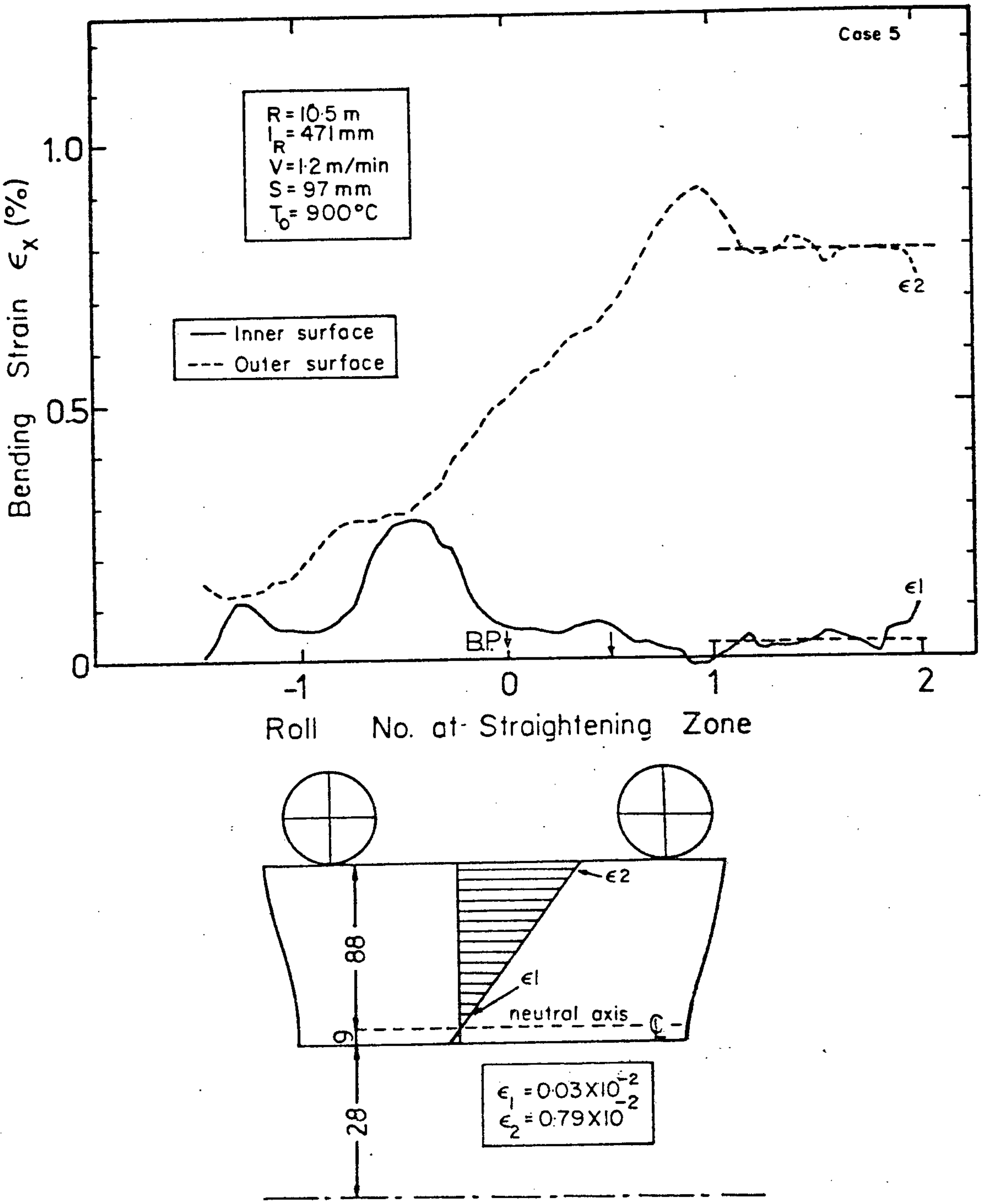

Fig. VI.7 Predicted Bending Strain, ϵ_x in Case 5. (Upper Shell)

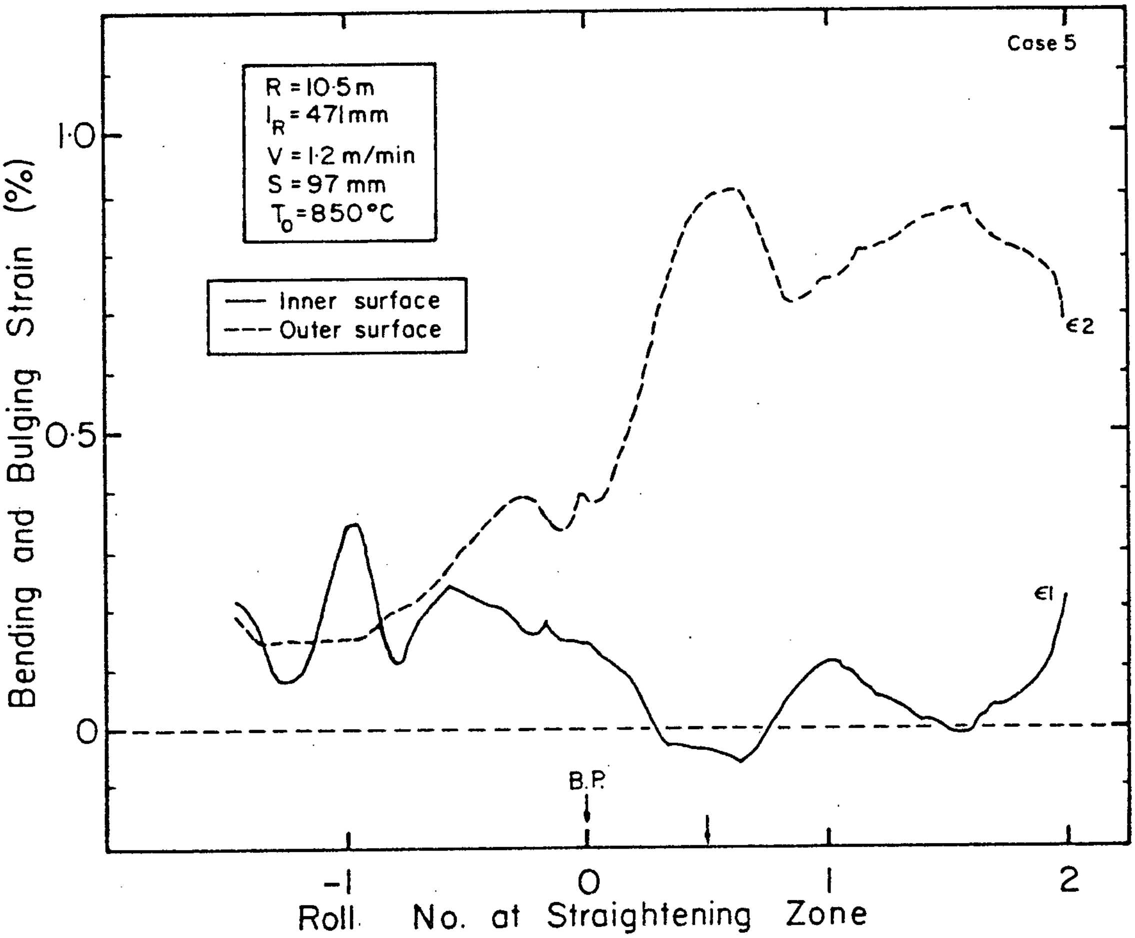

Fig. VI.8 Predicted Bending and Bulging Strain, ε_x in Case 5. (Upper Shell)

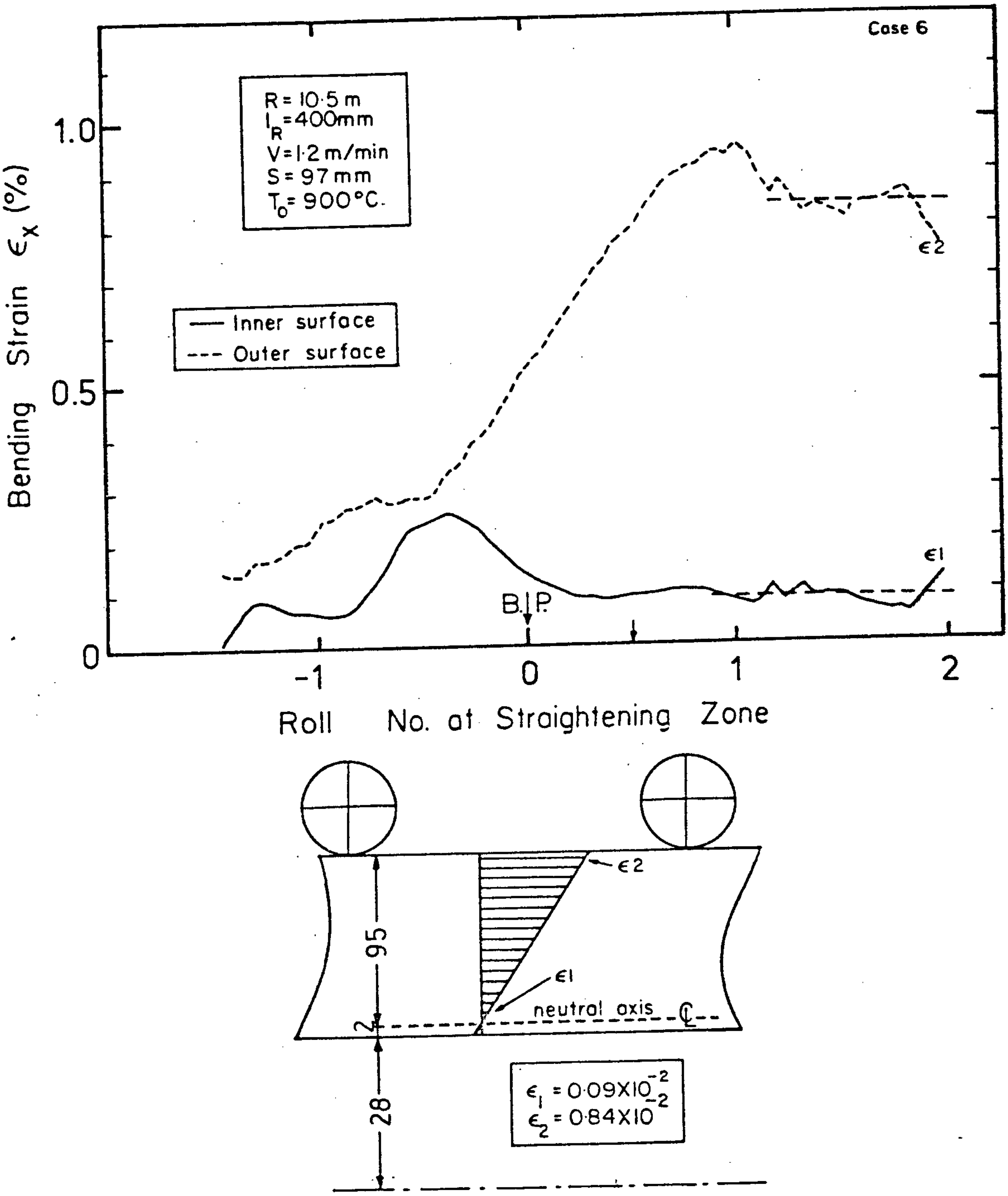

Fig. VI.9 Predicted Bending Strain, ε_x in Case 6. (Upper Shell)

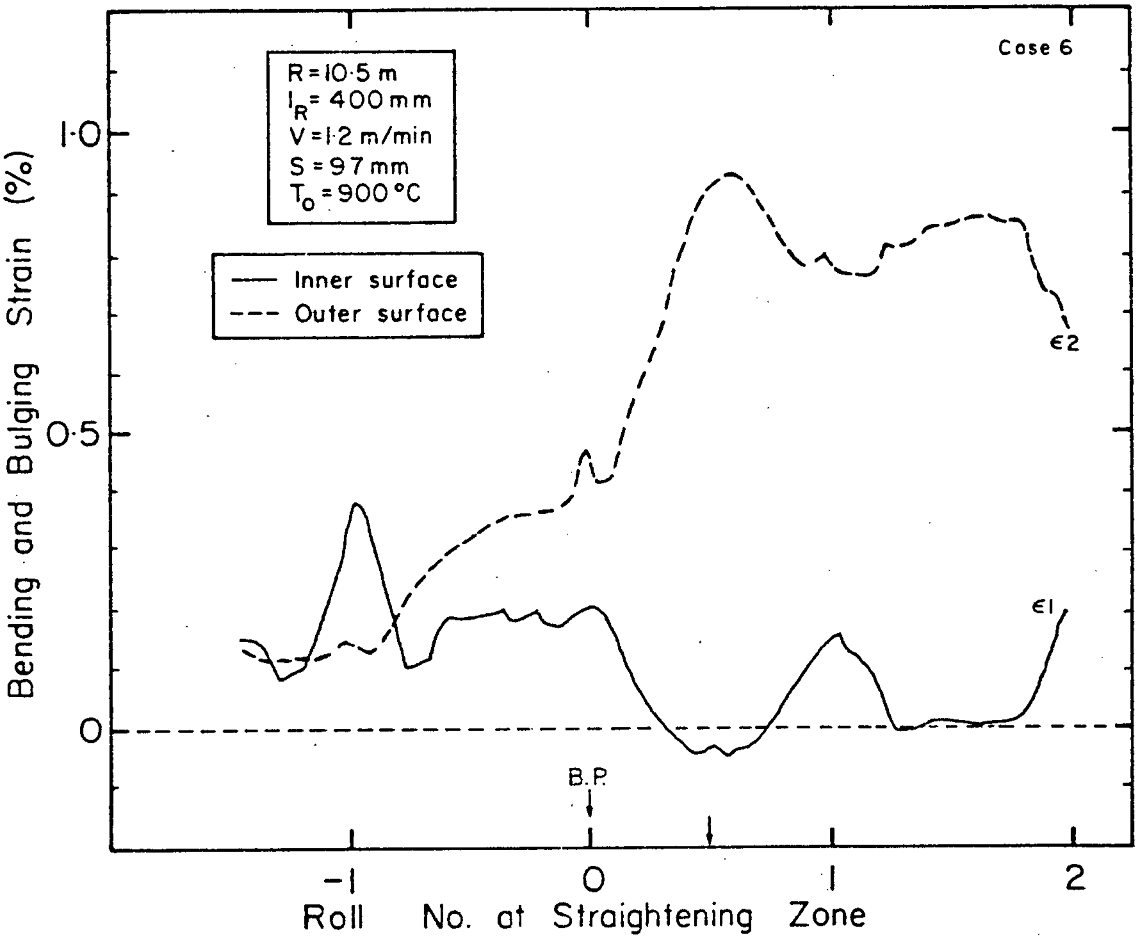

Fig. VI.10 Predicted Bending and Bulging Strain, ε_x in Case 6. (Upper Shell)

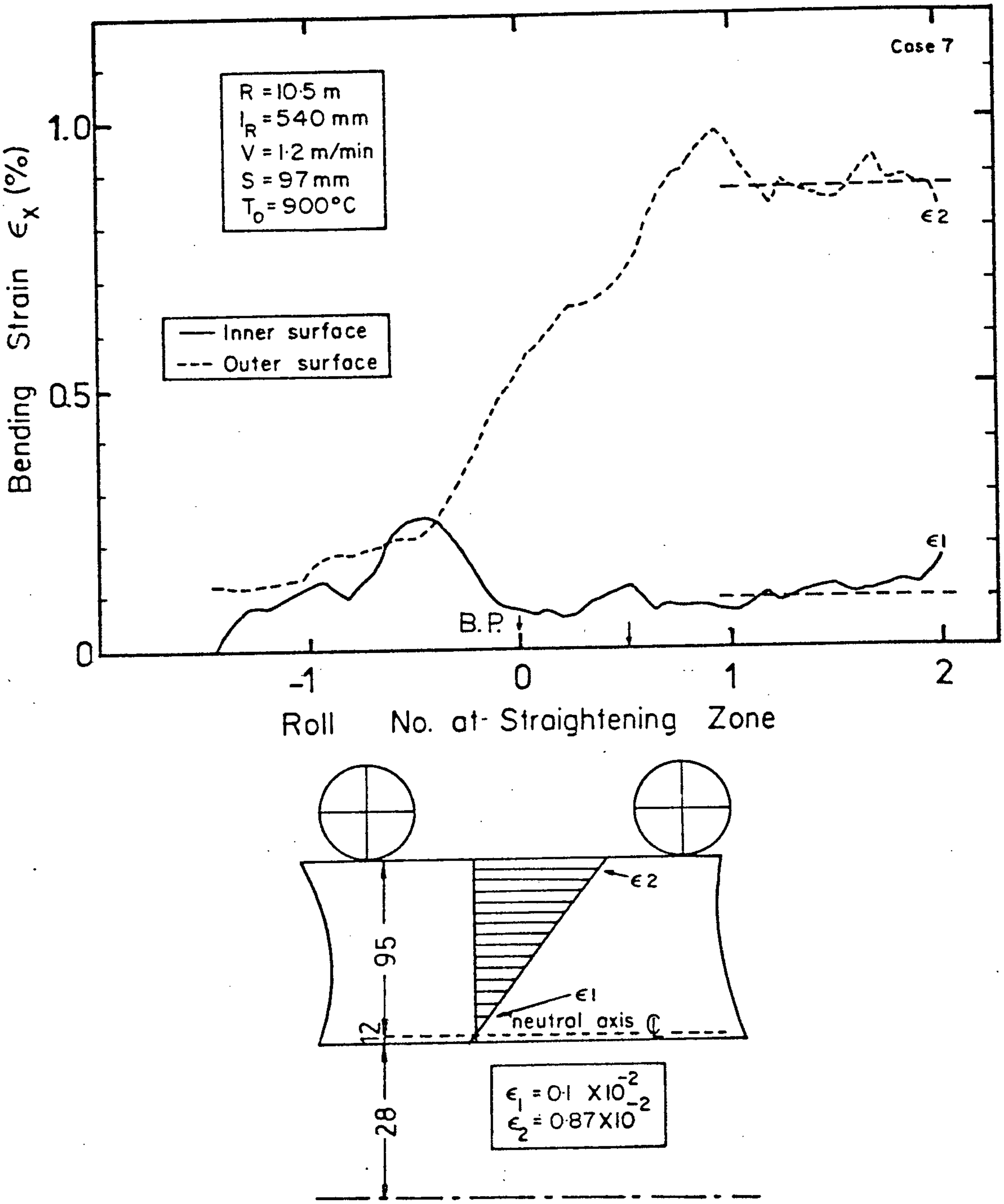

Fig. VI.11 Predicted Bending Strain, ε_x in Case 7. (Upper Shell)

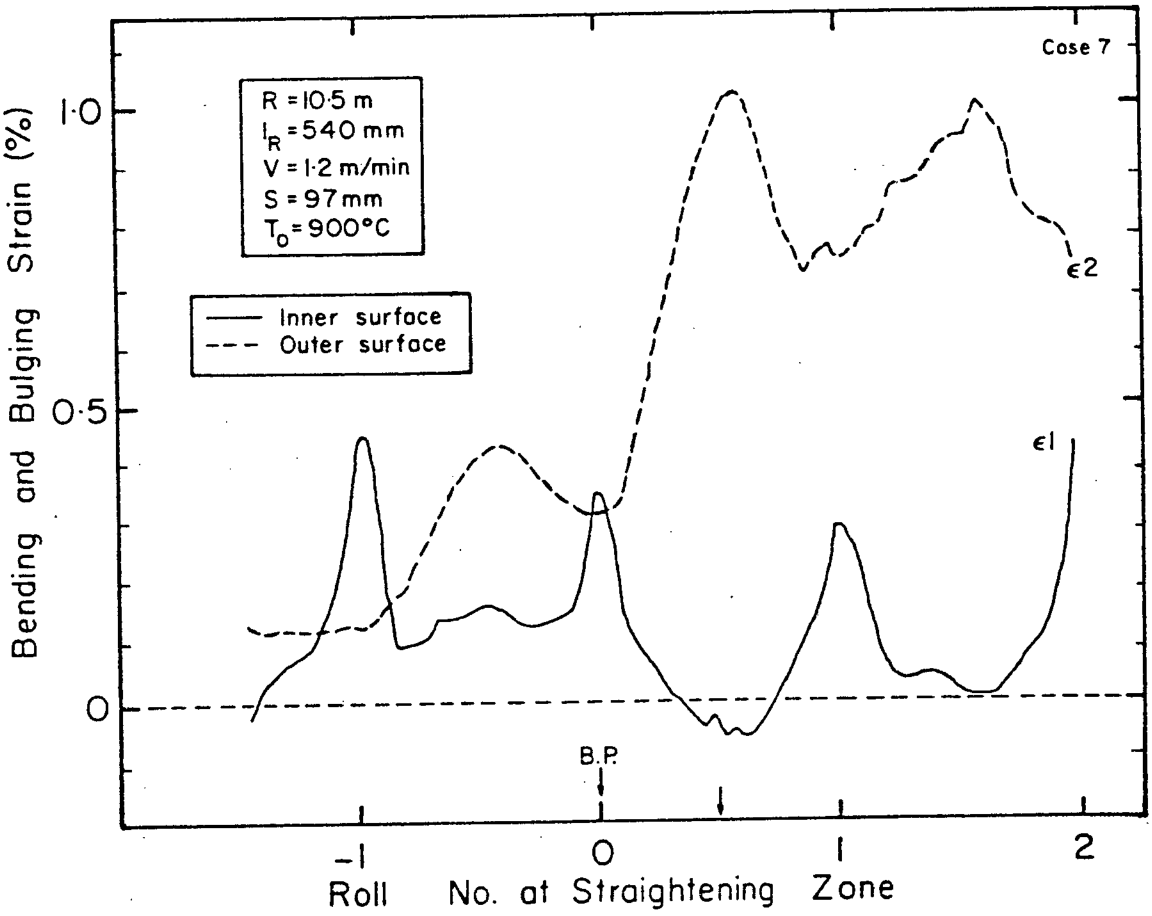

Fig. VI.12 Predicted Bending and Bulging Strain, ε_x in Case 7. (Upper Shell)

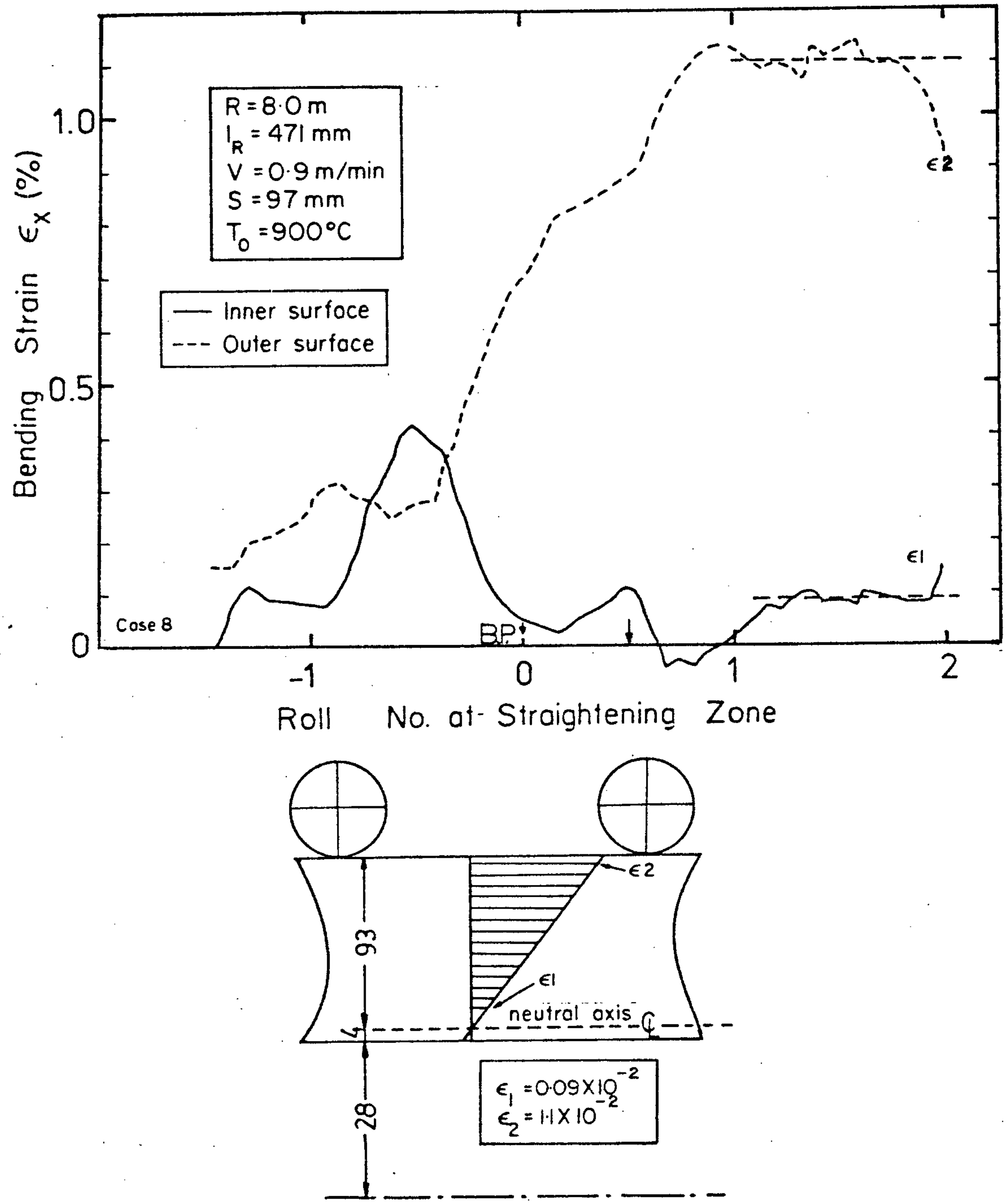

Fig. VI.13 Predicted Bending Strain, ε_x in Case 8. (Upper Shell)

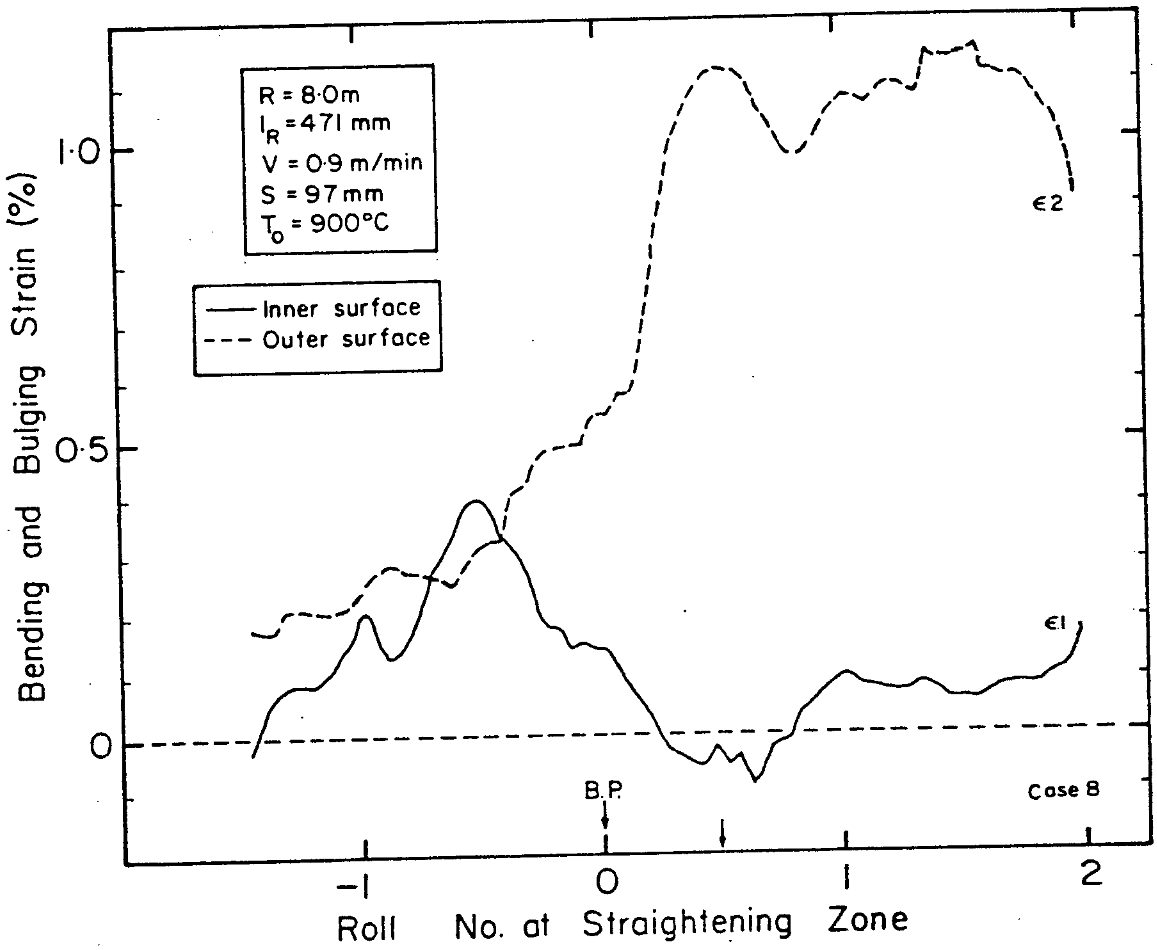

Fig. VI.14 Predicted Bending and Bulging Strain, ε_x in Case 8. (Upper Shell)

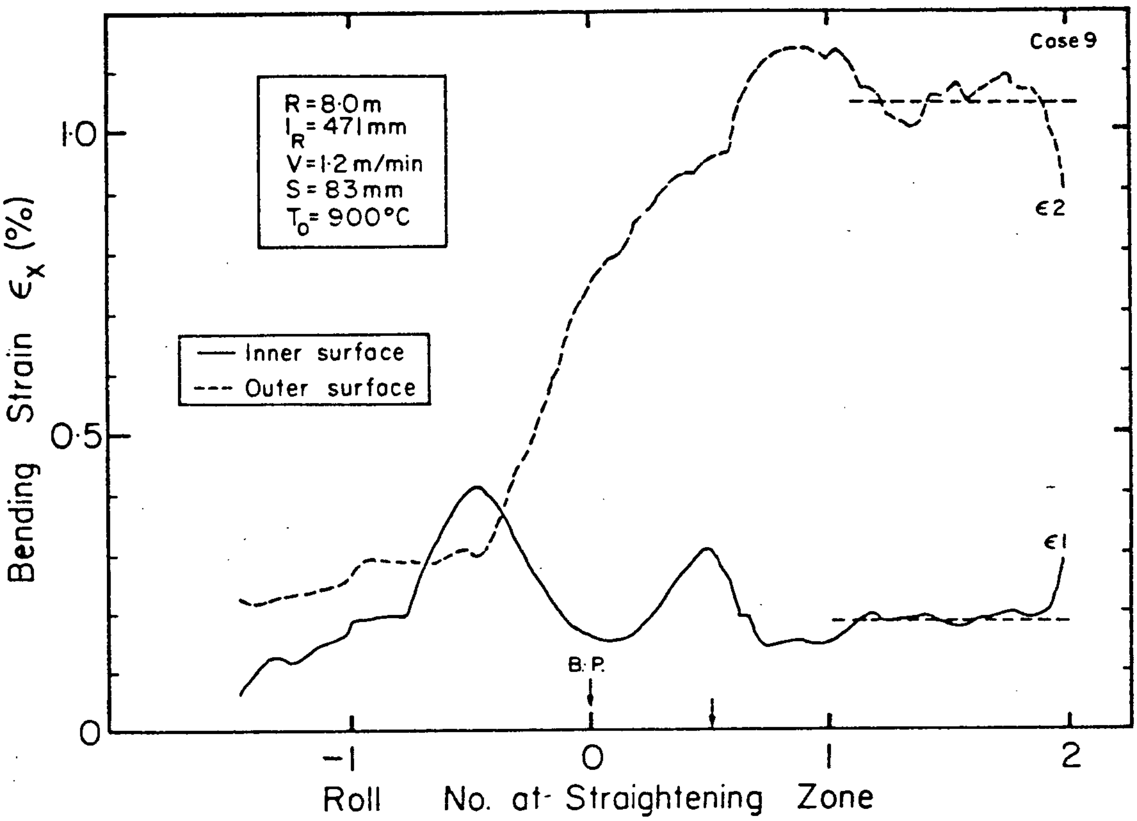

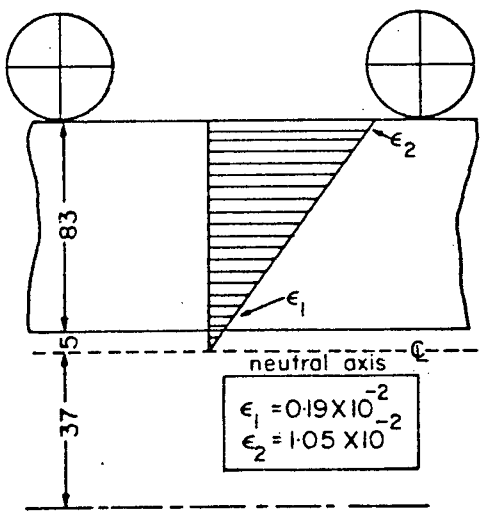

Fig. VI.15 Predicted Bending Strain, ε_x in Case 9. (Upper Shell)

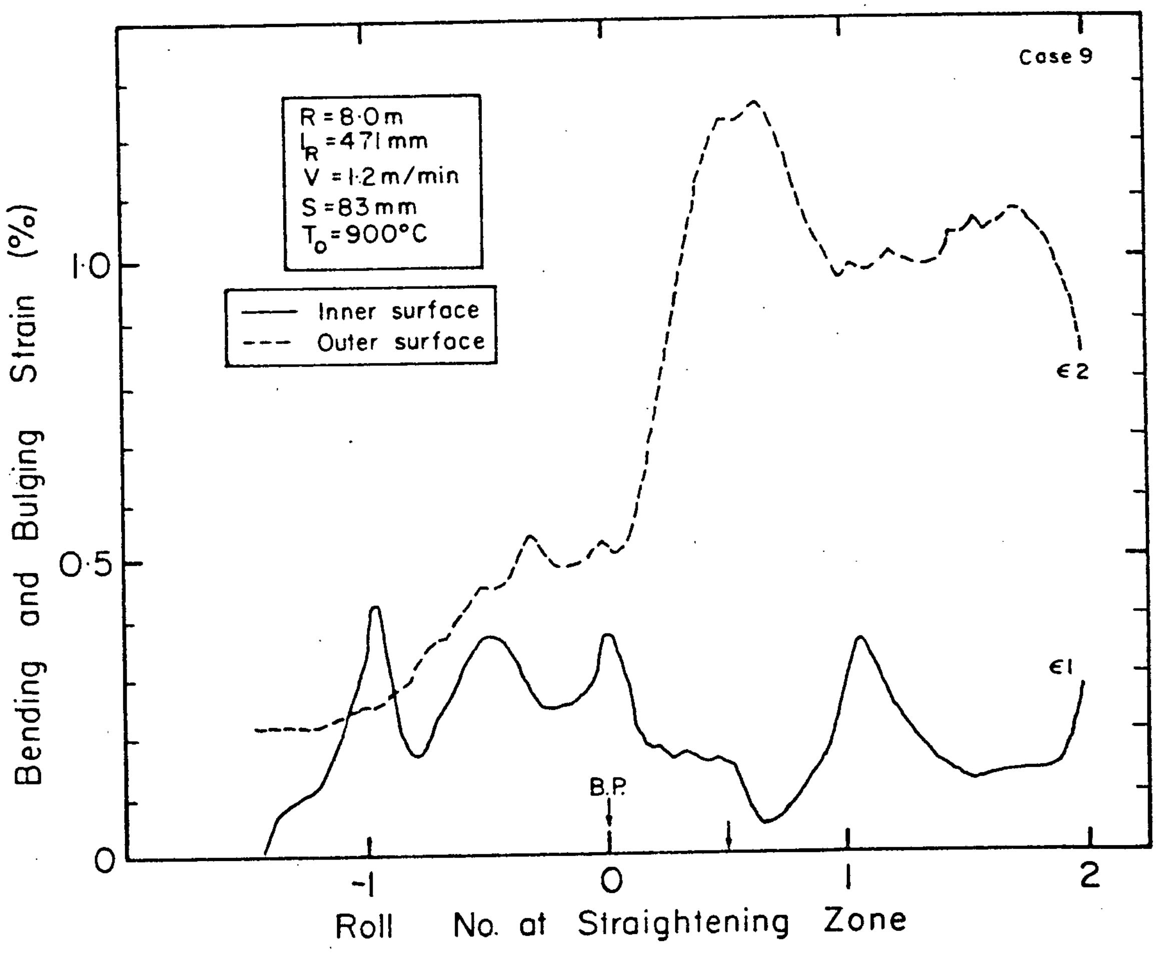

Fig. VI.16 Predicted Bending and Bulging Strain, ε_x in Case 9. (Upper Shell)

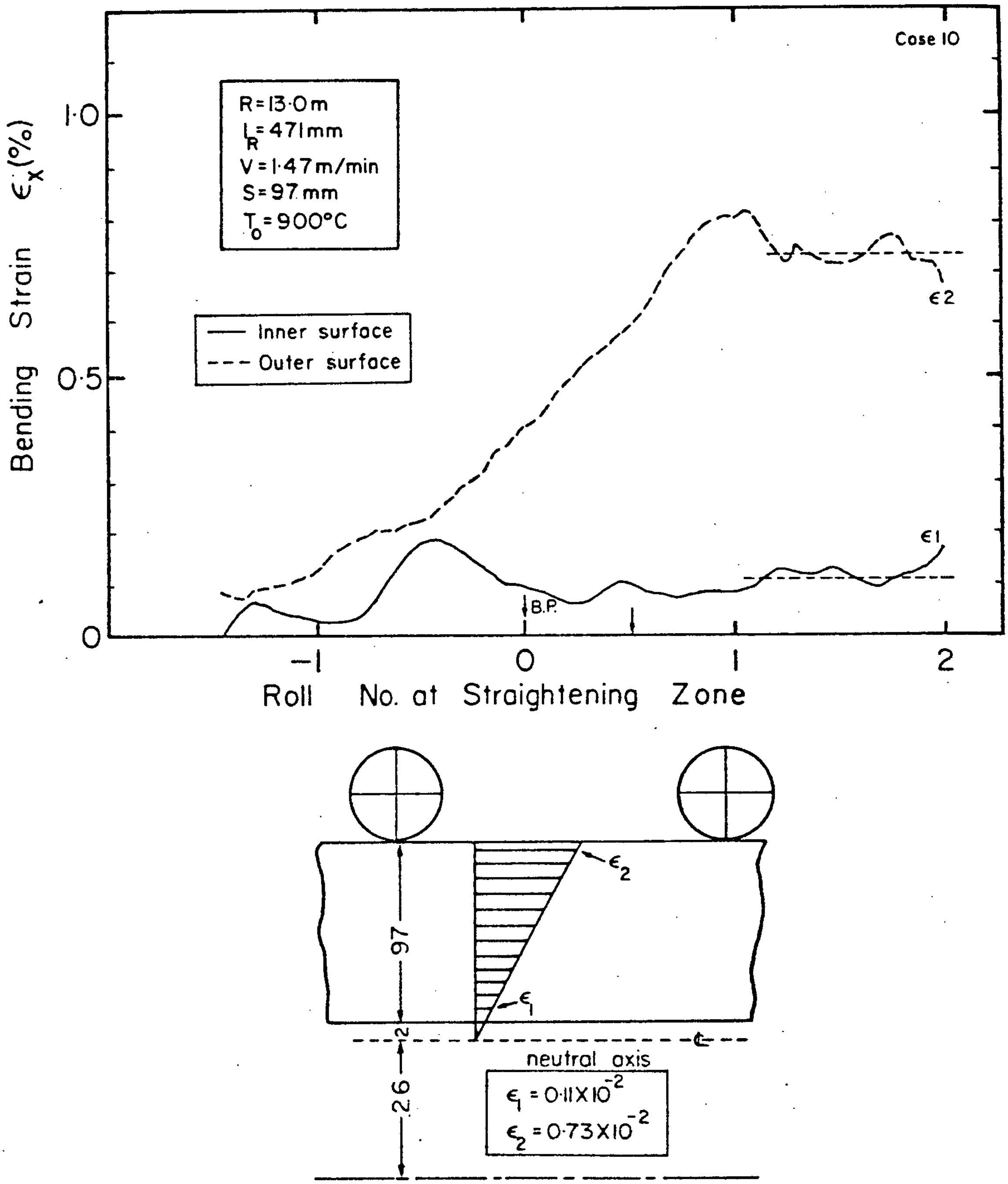

Fig. VI.17 Predicted Bending Strain, ε_x in Case 10. (Upper Shell)

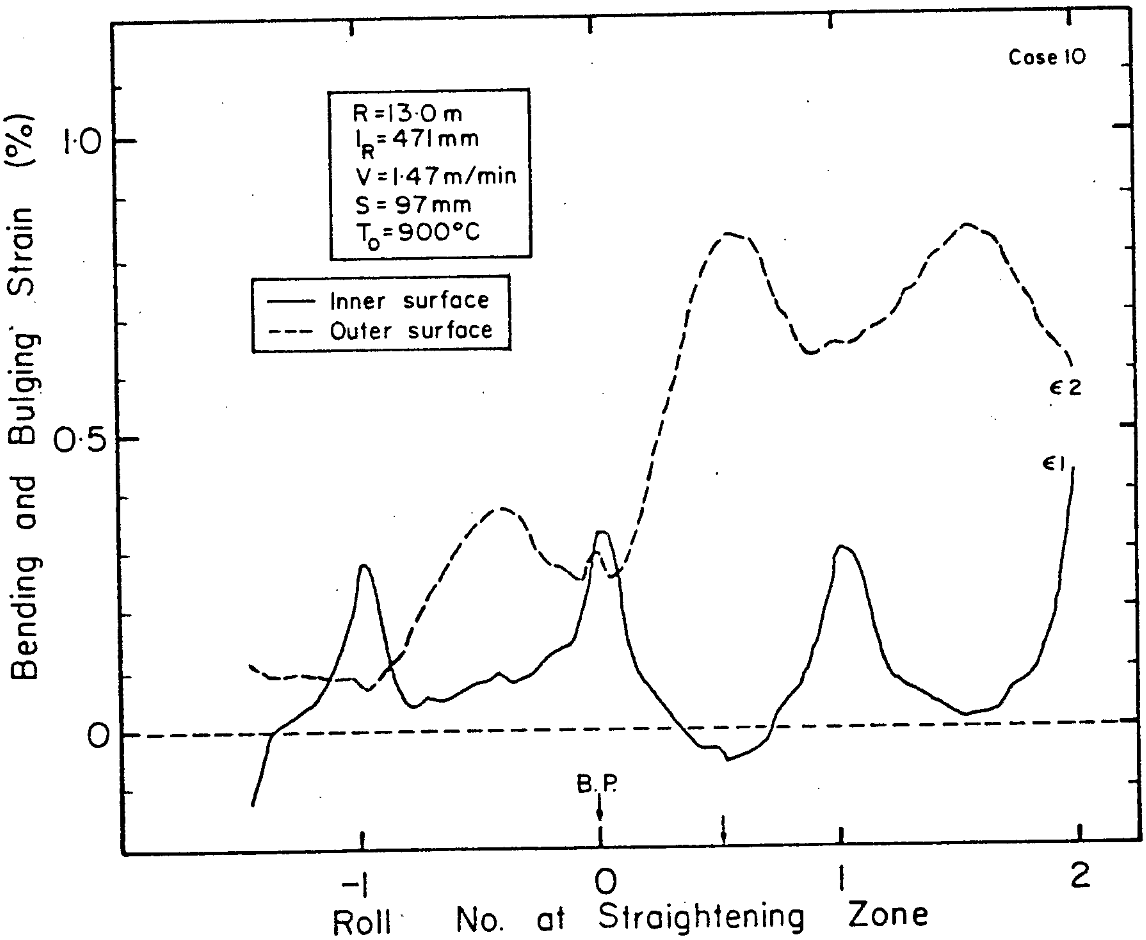

Fig. VI.18 Predicted Bending and Bulging Strain, ε_x in Case 10. (Upper Shell)